A Survey of Results in Modern Precision Cosmology

Thesis by

Anthony R. Pullen

In Partial Fulfillment of the Requirements

for the Degree of

Doctor of Philosophy

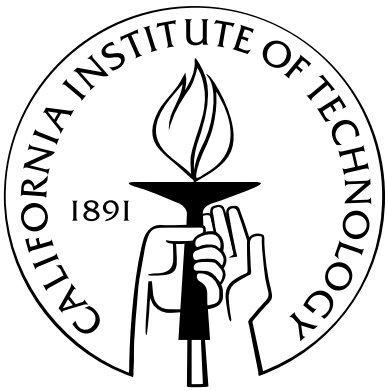

California Institute of Technology

Pasadena, California

2011

(Defended April 26, 2011)

Acknowledgements

The completion of this doctoral thesis marks a monumental moment in my life, and I know I would not have arrived here without all those who have encouraged me along the way. First of all, I thank Marc Kamionkowski, my advisor, who took a chance meeting with me when I was just a summer undergraduate intern and had no experience in theoretical cosmology. Throughout my Caltech tenure, Marc has helped me navigate the murky waters of being a researcher, and his knack for explaining complex physics in a pedagogical way is a talent I hope to emulate.

I also would like to thank those with whom I have collaborated at Caltech. I thank Ranga-Ram Chary for making the first couple of years of graduate research bearable by always being available to explain, and re-explain, the concepts I needed to compose my first research paper as a graduate student. I also thank Chris Hirata, who taught me to see beyond my immediate tasks and question my own results, qualities that distinguish the true researcher. In addition, I would like to thank TAPIR for fostering a premier research community. I also thank my fellow graduate students for stimulating conversation and friendship, including my officemates Dan Grin, Nate Bode, Sam Lee, Yacine Ali-Hammoud, Mike Kesden, and Hilke Schlichting, as well as Adrienne Erickcek, Tristan Smith, Jonathan Pritchard, Ben Collins, and Vera Gluscevic. And special thanks to Shirley Hampton, Joann Boyd, and Chris Mach for keeping TAPIR afloat.

I would not have even began this journey at Caltech if many people had not encouraged me during my academic career. I thank Mrs. Goldstein, my preschool teacher, who believed in me when my parents were told I would have trouble speaking and learning. Thanks to all of my teachers, music instructors, and coaches, for constantly encouraging me to be great and to be kind. I also would like to thank Southern University, my undergraduate institution, for giving me so many opportunities to excel. I thank Steven McGuire, the Chair of Physics, and Beverly Wade, the Dean of the Honors College at Southern U, for encouraging my potential and never allowing me to be distracted. And I owe deep gratitude to the Timbuktu Academy at Southern U, especially the directors Diola Bagayoko and Ella Kelley, for always challenging me to excel and for affording me many opportunities to research both at Southern University and abroad. I also thank all my college friends for helping me to discover myself, including Brandon Johnson and Aubrey Turner.

I know I would not be the scholar I am today without much encouragement from friends and

family outside academia. I thank Che Ahn, my pastor and mentor, for many heart-to-heart talks and for teaching me to pursue excellence. I truly honor and thank Ryan Turner, who has stood by me in my best times and worst times, and whom I am proud to call a dear friend. I give much thanks and love to Mom, Dad, my siblings Trey and Kelli, and all my relatives for their constant love and encouragement, and for always believing nothing is impossible for me. Finally, I thank the love of my life and my best friend, Bethany Roquemore, whose unwavering devotion, intellectual curiosity, and adventurous spirit will bring me great joy throughout all my years.

Abstract

In this work, we evaluate the evidence for some of the more exotic ideas in cosmology for which scientists are searching today, these anomalies being dark matter, statistical anisotropy, and non-Gaussianity. *Dark matter*, which is estimated to comprise 83% of the matter in our universe, still remains undiscovered. We search data from the Energetic Gamma Ray Experiment Telescope for a gamma-ray line in the energy range 0.1–10 GeV from the $10^\circ \times 10^\circ$ region around the Galactic center. Our null results lead to upper limits to the line flux from the Galactic center. We use these limits to place constraints on the particle's two-photon annihilation cross section as a function of its mass, which we show to produce stronger limits than those derived from measurements of the 511-keV line.

Next, we investigate the possibility that cosmic inflation deviates from statistical isotropy. Statistical isotropy is a common assumption that should be tested. We develop cosmic-microwave-background statistics for a direction-dependent primordial power spectrum. We then construct minimum-variance estimators for the coefficients of a spherical-harmonic expansion of the direction-dependence of the primordial power spectrum. We find that a power quadrupole as small as 2.0% can be detected by the Planck satellite. We also constrain statistical anisotropy of the quadrupolar form using a sample of photometric luminous red galaxies measured by the Sloan Digital Sky Survey. Not detecting evidence, we place limits on an axisymmetric quadrupole model. We find discrepancies between our results and a cosmic microwave background analysis that claimed a positive detection. We also find the quadrupolar asymmetry limits to be between -0.41 and 0.38 with 95% probability.

Finally, we prepare a search for evidence of non-Gaussianity in the the early universe. Scale-dependent bias has been shown to be a competitive probe of non-Gaussianity in large-scale structure, and constraints have been calculated using various tracers of the matter distribution. We seek to extend this analysis to the latest sample of photometric quasars measured by the Sloan Digital Sky Survey to search for evidence of scale-dependent bias in large-scale structure. Specifically we construct three data samples at various redshifts, removing various systematic effects. We calculate the cross-correlation angular power spectra between two of the data samples to search for any remaining systematics. We find a positive detection on large scales, which leads us to the conclusion that more systematics testing is needed to render this QSO catalog useful to constrain non-Gaussianity.

Contents

List of Figures

List of Tables

Chapter 1

Introduction and Summary

1.1 The Quest for Precision

The current standard picture of cosmology, a patchwork of several ideas that together describe our universe very precisely, is a triumph of the pursuit of precision cosmology over the previous three decades. The very early universe seems to have undergone a period of exponential expansion called *inflation* that has made our observable universe isotropic and without curvature. The particle driving this early expansion, a single scalar field called the *inflaton*, decayed, producing matter density fluctuations that exhibit an isotropic and nearly Gaussian distribution. We also know based on the expansion history of our universe that its fundamental elements consist of *dark matter*, an exotic material that does not interact electromagnetically with other particles, and *dark energy*, a mysterious force with negative pressure that drives the current accelerated expansion, with normal matter and radiation comprising less than 5% of the universe's energy budget. This patchwork of ideas agrees very well with observations of the cosmic microwave background (CMB) radiation and large-scale structure (LSS).

While these ideas together are a competitive model for our universe, each individual idea struggles to find compelling observational clues to reveal its nature. We know that dark matter must consist mostly in the form of weakly-interacting massive particles (WIMPs), yet these particles have yet to be discovered in particle detectors or colliders. Measurements of the CMB and LSS are just beginning to reach the precision necessary to distinguish between various inflation models, while anisotropic inflation, multi-field inflation, and the ekpyrotic model (cyclic expansion) remain viable alternatives. The next generation of experiments are set to usher in a new era of precision cosmology where the true natures of dark matter and inflation can be revealed. In this thesis, we report our investigations of dark matter and inflation alternatives that have contributed to our current understanding of the early universe as well as motivated further studies in this field.

Much evidence exists for WIMP dark matter, a theorized particle that only interacts with other particles through the weak force and gravity, as a major component of the universe [1, 2, 3]. Dark

matter halos explain the flat rotation curves of stars in most galaxies at large distances as well as the stability of most galaxies. On large scales, the spectrum of matter perturbations and temperature fluctuations of the CMB require most of the matter in the universe to be of a nonbaryonic form, favoring WIMPs as the preferred theory. The main competitors to dark matter are modified gravity theories [4, 5, 6], yet the so-called "bullet cluster" [7], in which the center of mass was shown to be separated from the center of visible matter, greatly favors dark matter as the correct explanation. The nonbaryonic nature of this particle leads us speculate its identity is within a particle theory beyond the Standard Model. Supersymmetry (SUSY) [8], a solution to the hierarchy problem in particle physics, requires every Standard Model fermion to have a bosonic superpartner, and vice-versa. SUSY behaves as a broken symmetry in nature, causing the superparticles to be much heavier than the Standard Model particles. A WIMP candidate naturally arising from this theory is the neutralino, the lightest stable particle in SUSY and is expected to have a mass between 10 GeV to a few TeV. Though the neutralino is the most favored candidate, particles with lower masses have still received much interest. Neutralinos with lighter masses, or light dark matter, have been shown to be possible in theories where the unification of SUSY gauge particles, or *gauginos*, at high energies is not assumed [9]. Some SUSY theories even allow neutralino masses as low as 100 MeV [10, 11]. One way to detect these particles is through their annihilation signal, which indirectly includes gamma rays. Specifically, a gamma ray spectrum in the case of WIMP annihilation should include a line with an energy equal to the WIMP mass [12]. Though these searches are currently being done using the Fermi Gamma-Ray Space Telescope [13], dark matter with masses less than 10 GeV should be detectable using data from its predecessor, the Energetic Gamma-Ray Experiment Telescope (EGRET) [14]. Particularly, we should be able to constrain the cross section to gamma rays by using this data.

The most ubiquitous characteristics of our universe are its homogeneity and isotropy. Although matter perturbations such as galaxies and clusters prevent pure homogeneity and isotropy to be possible, symmetry still suggests that the universe is *statistically* homogeneous and isotropic. In this case, the distributions of both matter and CMB perturbations are isotropic and homogeneous as viewed by any observer at rest with respect to the CMB. These assumptions are taken for inflation models; however, several signals in the CMB have suggested that statistical isotropy (SI) could be broken [15, 16, 17, 18]. These signals include cold spots, alignment of multipole moments, and power asymmetries between the Galactic hemispheres. These reported signals have led to many theoretical studies to find their explanation, including investigations of modified inflation [19, 20, 21, 22, 23, 24, 25, 26, 27, 28] and modified dark energy [29, 30]. Most of the *a posteriori* detections of SI violations, including all of those mentioned earlier, have been shown to be statistically insignificant when performing a proper *a priori* analysis [31]. While the Wilkinson Microwave Anisotropy Probe (WMAP) [32] has helped constrain SI violation considerably, we hoped to find

if Planck [33], the next-generation CMB probe, could present the first truly precise constraints (or possible detection) of statistical anisotropy.

One *a priori* signal that has been shown to be significant is a quadrupolar asymmetry in the CMB. In particular, an inflation model proposed by Ackerman et al. [24] called for a matter power spectrum of fluctuations that depended on its wavevector's scale and direction, producing a statistically anisotropic observable universe exhibiting quadrupolar asymmetry. Although this particular model has been shown to be unstable [34], the quadrupolar matter power spectrum serves as a capable straw-man test of future statistically asymmetric models. In particular, a claimed detection of quadrupolar asymmetry was presented using WMAP data [35]. Though this detection was later shown to be in the direction of the Ecliptic [36] and thus highly suspected to be due to systematic effects [37, 38], this motivated the search for a compatible signal in LSS, particularly within the galaxy distribution. With the Sloan Digital Sky Survey (SDSS) [39] containing the largest well-sampled catalog of luminous red galaxies (LRGs), we expected that a constraint could be placed on statistical anisotropy using this data.

Another signature of standard inflation that is currently being tested is Gaussianity. The standard single-field, slow-roll inflation has a number of potential observables that can distinguish it from other inflation models and alternatives, including the primordial power spectrum of perturbations, B-mode polarization, the lack of isocurvature perturbations, and Gaussianity. In particular, Gaussianity is the idea that the primordial perturbations to the inflaton that produced the LSS we see today exhibit a Gaussian distribution. Although even the standard inflation model exhibits some non-Gaussianity, this signal is undetectable because it would be much less than the signal due to nonlinearities [40]. However, current cosmological probes have not ruled out alternatives to the standard model, such as multi-field inflation or the ekpyrotic model. In order to try to confirm or rule out these alternatives, gravitational perturbations produced by the inflaton are written as $\Phi = \phi_g + f_{NL}\phi_g^2$, where f_{NL} parametrizes the amount of non-Gaussianity [41, 42]. Much work has been done to constrain f_{NL}. The most popular statistic in this endeavor has been the CMB bispectrum, or three-point correlation function, which vanishes for $f_{NL} = 0$. From this statistic we now know $|f_{NL}| \lesssim 100$ [43]. Alternative probes using LSS include the galaxy bispectrum, which suffers from nonlinearities, and galaxy and dark matter clustering, which suffer from low-number statistics. One method that has been successful in probing non-Gaussianity using LSS is searching for scale-dependent halo bias [44, 45]. In standard structure-formation models, matter perturbations inside dark matter halos clump together to produce fluctuations in the number density of galaxies, with the bias being the ratio between the fluctuations in galaxy number density and matter density. This bias is considered to be redshift-dependent but normally scale-independent. In standard inflation, large-scale density fluctuations that produce matter halos are uncorrelated with the small-scale fluctuations that form galaxies. This is no longer true when non-Gaussianity is present,

causing small-scale fluctuations to be modulated by the large-scale ones. Thus, we would see greater power on large scales, and this manifests as a bias correction that scales as k^{-2}. There have been many searches for this effect in LSS, and these constraints are becoming competitive with CMB bispectrum constraints. One tracer of the matter density that is of great interest is quasars. These are some of the brightest objects at large distances, making them useful in constraining LSS at redshifts $z \gtrsim 1$. One of the latest analyses used a quasar sample that included quasars from redshifts $1.45 < z < 2$[45]. Since then, the quasar sample has been extended to larger redshifts ranges, with redshifts as low as $z = 0.9$ and as large as $z = 2.9$. With a larger range, we should be able to constrain f_{NL} more precisely.

In this thesis, we discuss precision measurements that have advanced our quest to find or rule out dark matter, statistical anisotropy, and non-Gaussianity. In Chapter 2, we set constraints on the cross section for light dark matter to annihilate into photons using measurements of the diffuse gamma ray background from EGRET. The next two chapters focus on statistical anisotropy searches. In Chapter 3, we show how future CMB probes like *Planck* will be able to constrain quadrupolar asymmetry, while Chapter 4 discusses actual constraints we set on quadrupolar asymmetry using LSS data from SDSS. Finally, we present work towards placing limits on non-Gaussianity from photometric quasars in Chapter 5.

1.2 Constraints on Light Dark Matter

In Chapter 2, we search data from the Energetic Gamma Ray Experiment Telescope (EGRET) for a gamma-ray line in the energy range 0.1–10 GeV from the $10^\circ \times 10^\circ$ region around the Galactic center. Any significant gamma-ray line emission found could have been produced by WIMP annihilation, in which two nonrelativistic WIMPs collide and annihilate to become two gamma-ray photons of equal energy. In the limit of negligible WIMP speeds, the energy of the gamma-ray lines equals the WIMP mass. We probe the Galactic center because this is where the ratio of annihilation photons, which vary as $\rho^2_{\rm DM}$, to the background cosmic rays is largest. We begin by constructing the gamma ray differential flux in the range 100 MeV $< E_\gamma <$ 10 GeV in the galactic coordinate range $-5^\circ < l < 5^\circ$ and $-5^\circ < b < 5^\circ$ using EGRET data. We then fit this differential flux with various astrophysical templates including nuclear interactions in the interstellar medium, electron bremsstrahlung, and unresolved point sources within our Galaxy, which we then subtract to find the residual flux. Taking into account energy uncertainties, we search for evidence of a gamma-ray line. Our null result leads to upper limits to the line flux at each energy in the range 0.1–10 GeV. Assuming WIMP annihilation as the sole source of gamma-ray lines from the Galactic center and using the relation between the flux product and the dark matter halo density profile, we construct upper limits to the WIMP two-photon annihilation cross section as a function of WIMP mass for

various dark matter halo models. We also show that for a toy model in which Majorana WIMPs in this mass range annihilate only to electron-positron pairs, these upper limits supersede those derived from measurements of the 511-keV line and continuum photons from internal bremsstrahlung at the Galactic center.

1.3 Upcoming CMB Probes of Statistical Anisotropy

We develop cosmic microwave background statistics in Chapter 3 for a primordial power spectrum that depends on the direction, as well as the magnitude, of the Fourier wavevector. We use the anisotropic inflation model proposed by Ackerman, Carroll, and Wise (ACW) as our toy model, with a parameter g_{2M} scaling the quadrupolar part of the power spectrum. We begin by introducing the formalism of anisotropic power spectrum effects on the spherical harmonic coefficients of the CMB temperature fluctuations. This formalism is generalized for the non-quadrupolar case by scaling each multipole L term of the power spectrum with g_{LM}. We find that the angular power spectrum C_l is supplemented by the set of moments $D_{ll'}^{LM}$ that connects power between different scales. We then consider a simple estimator we call the *power multipole moments* that searches in a model-independent way for anisotropy in the square of the temperature (and/or polarization) fluctuations. Though we can use this estimator to search for a general form of statistical anisotropy, we find that it is sub-optimal for power asymmetry. We then construct the minimum-variance estimators for the coefficients of a spherical-harmonic expansion of the direction-dependence of the primordial power spectrum. To illustrate, we apply these statistics to an inflation model with a quadrupole dependence of the primordial power spectrum on direction and find that a power quadrupole as small as 2.0% can be detected with the Planck satellite limited by partial sky coverage. We present the formalism for using polarization fluctuations in Appendix A.

1.4 New Limits to Statistical Anisotropy Using LSS

In Chapter 4, we set limits on quadrupolar asymmetry in the primordial power spectrum using the SDSS Data Release 5 (DR5) photometric LRG sample as a tracer of the matter distribution. As in the previous chapter, we parametrize quadrupolar asymmetry in terms of the ACW model, with the parameter g_{2M} scaling the quadrupolar variation in the power spectrum. We first develop the formalism for anisotropic power spectrum effects on the spherical harmonic coefficients of the galaxy number density perturbations. We use this formalism to construct estimators for the g_{2M}s. After testing the robustness of our estimators, we use them to derive estimates of g_{2M} while allowing for other systematic effects in the calibration. We find a null result for our search; however, we use our results to construct upper limits to g_{2M}. We then compare our results to a claimed detection

of quadrupolar asymmetry in the CMB. By converting our five g_{2M} parameters into a quadrupolar asymmetry magnitude g_* (given an asymmetry direction), we show that our result using LSS is incompatible with the CMB result. This leads to the conclusion that the CMB result is due to instrumental error and not cosmological in origin. We then marginalize our estimates of g_{2M} over asymmetry direction to get a 95% confidence interval for g_* given by $-0.41 < g_* < +0.38$. In Appendix C, we calculate connection coefficients for the real spherical harmonics listed in Appendix B used in our calculations. We also calculate the effective scales for g_{2M} probed by the CMB and LSS in Appendix D.

1.5 Search for Non-Gaussianity Using LSS

In Chapter 5, we seek to prepare photometric quasar maps in order to constrain local-type non-Gaussianity in the primordial pertubations created during inflation by probing the scale-dependence of the halo bias. We parametrize non-Gaussianity in terms of f_{NL}, which scales the non-Gaussianity-inducing quadratic correction to the gravitational perturbation field. Using the formalism developed for scale-dependent bias in terms of f_{NL}, we derive estimators for the angular power spectrum of perturbations in quasar number density in terms of f_{NL}. We also model systematic effects that must be projected out to constrain f_{NL} properly. We calculate the cross-correlation angular power spectrum between the first and third slices to search for systematics. We see that systematic errors persist despite our efforts to remove them. We conclude more systematic analysis must be undertaken to produce clean autocorrelation power spectra of the quasar maps. These spectra will be useful in constructing limits on f_{NL}. In Appendix E we determine the redshift distributions for the three redshift slices.

Chapter 2

Search with EGRET for a Gamma-Ray Line from the Galactic Center

2.1 Introduction

Weakly-interacting massive particles (WIMPs) provide promising candidates for the dark matter in Galactic halos [1, 2, 3]. The most deeply explored WIMP candidate is the neutralino, the lightest superpartner in many supersymmetric extensions of the standard model [8]. Although the favored mass range for neutralinos is usually $\gtrsim 10$ GeV, there are other WIMP candidates with masses in the 0.1–10 GeV range. For example, neutralinos with masses as low as 6 GeV are plausible if gaugino unification is not assumed [9]. Neutralinos with masses as low as 100 MeV are plausible in the next-to-minimal supersymmetric standard model (NMSSM) [10, 11]. Also, scalar and spin-1/2 particles with masses in the MeV range have been considered [46] to explain the 511-keV gamma-ray line observed by INTEGRAL [47, 48], a line whose strength, as explained in Ref. [46], has defied easy explanation from traditional astrophysics.

One way to detect WIMPs is to search for monoenergetic gamma rays produced by pair annihilation in the Galactic halo [12]. These gamma rays have energies equal to the WIMP mass m_χ. Such a line spectrum could be easily distinguished from the continuum spectrum from more prosaic gamma-ray sources (e.g., cosmic-ray spallation), and thus serve as a "smoking gun" for dark-matter annihilation.

Since the dark-matter density is highest at the Galactic center, the flux of WIMP-annihilation photons should be greatest from that direction. On the other hand, the continuum background should also be highest from the Galactic center. We estimate that for a Navarro-Frenk-White

[0]The material presented in this chapter was first published in *Search with EGRET for a gamma-ray line from the Galactic center*, Anthony R. Pullen, Ranga-Ram Chary, and Marc Kamionkowski, Phys. Rev. D **76**, 063006 (2007). Reproduced here with permission, copyright (2007) by the American Physical Society.

profile [49], the WIMP-annihilation flux from the $10^\circ \times 10^\circ$ region from the Galactic center should exceed that from the Galactic anticenter by a factor ~ 100, while the flux of cosmic-ray–induced photons at energies O(GeV) is only about 8 times higher from the Galactic center than from the Galactic anticenter. Thus, the Galactic center is the preferred place to look for a WIMP-annihilation signal. It is also the location of the 511-keV anomaly that has motivated the consideration of lower-mass WIMPs.

In this chapter, we search data from the Energetic Gamma Ray Experiment Telescope (EGRET) [14] on the Compton Gamma Ray Observatory (CGRO) for a gamma-ray line in the energy range 100 MeV to 10 GeV from a $10^\circ \times 10^\circ$ region around the Galactic center. We found no evidence for a gamma-ray line from the Galactic center in this energy range. From these null results, we can bound the cross section $\langle \sigma v \rangle_{\gamma\gamma}$ for WIMP annihilation to two photons for WIMPs in this mass range.

The plan of this chapter is as follows: In Section 2.2, we discuss how EGRET data are cataloged. In Section 2.3, we reconstruct from the EGRET data the differential flux of photons as a function of energy. In Section 2.4, we fit to the data a model of the flux produced by cosmic rays and point sources near the Galactic center. In Section 2.5, we search for a line excess of photons from WIMP annihilation. In Section 2.6, we report upper limits to $\langle \sigma v \rangle_{\gamma\gamma}$ as a function of m_χ for WIMPs within the mass range of 0.1 GeV to 10 GeV for a variety of dark-matter-halo models. In Section 2.7, we show that in a toy model in which the WIMP annihilates only to electron-positron pairs, this upper limit is stronger over this mass range than limits derived from the 511-keV line and from lower-energy continuum gamma rays from internal bremsstrahlung.

2.2 Source of Data

We obtained publicly available data from the CGRO Science Support Center (COSSC).[1] We used the EGRET photon lists (QVP files), which contain event lists of all photons detected during a given viewing period. The data that we used from these files are the photon's Galactic latitude, Galactic longitude, zenith angle, energy, and energy uncertainty. We also required the exposure files, which contain the detector's effective area multiplied by the viewing time of the detector for a particular viewing period multiplied by EGRET's 1-sr field of view. The exposure is provided as a function of latitude, longitude, and energy range. We also obtained the counts files, which contain the number of photons at various spatial coordinates and energy ranges within a viewing period. The energy bins, along with their respective energy ranges, are shown on the COSSC site.

[1] http://cossc.gsfc.nasa.gov/docs/cgro/cossc/egret/

Table 2.1: Viewing periods used in analysis. The more dominant viewing periods are in bold and have an exposure of $> 10^6$ cm^2 s sr at 150–300 MeV, over our region of interest.

5.0	**7.2**	**13.1**	**16.0**	20.0	23.0	**27.0**
35.0	38.0	42.0	43.0	**209.0**	**210.0**	**214.0**
219.0	**223.0**	**226.0**	229.0	**229.5**	231.0	**232.0**
302.3	**323.0**	**324.0**	**330.0**	**332.0**	**334.0**	**336.5**
339.0	**421.0**	**422.0**	**423.0**	**423.5**	**429.0**	

2.3 Construction of Gamma-Ray Flux

We begin by constructing the photon differential flux as a function of energy. We use data only from a square region on the sky from $-5°$ to $5°$ Galactic longitude and $-5°$ to $5°$ Galactic latitude. Each viewing period covers a particular region of the sky, and there were 34 viewing periods for our region of interest. These viewing periods were found using Table 1 in the Third EGRET Catalog [50] and are listed in Table 2.1.

The differential photon flux can be determined from the counts files provided by EGRET, but these provide only counts in 10 energy bins, each with a width comparable to the photon energy in that bin. However, we will below search for lines with energies spanning the full energy range. This analysis is performed (as discussed below) by fitting the measured photon distribution to a continuum plus a line broadened by a Gaussian, consistent with the instrumental resolution, about each central line energy. We therefore work with the EGRET events and exposure files, which list an energy and effective exposure, respectively, for each photon, and reconstruct the differential energy flux in 119 energy bins. Before doing so, however, we first construct the differential energy flux from the events files with the same 10 bins as in the EGRET counts files, to be sure that our event-file analysis recovers the EGRET counts files, the most commonly used EGRET data product.

We first split the data into the 10 energy bins used by EGRET. Since the exposure files record a photon index value of 2.1 for the photon distribution (a value more-or-less consistent with the fluxes arrived at in Figs. 2.1 and 2.2), the average energy $E_{\rm avg}$ of photons in an energy bin $[E_{\rm min},E_{\rm max}]$ is

$$E_{\rm avg} = 11 \times \frac{E_{\rm min}^{-0.1} - E_{\rm max}^{-0.1}}{E_{\rm min}^{-1.1} - E_{\rm max}^{-1.1}} \text{ MeV}. \tag{2.1}$$

Variation of the photon index values over the range [1.7,2.7] only changes $E_{\rm avg}$ by $\sim 1\%$ for these energy bins and by $\sim 0.01\%$ for the 119 smaller energy bins. This variation also only changes the average exposures by less than 10%, which does not affect our final results significantly. Thus, our assumption of a value of 2.1 for the photon index is a reasonable one.

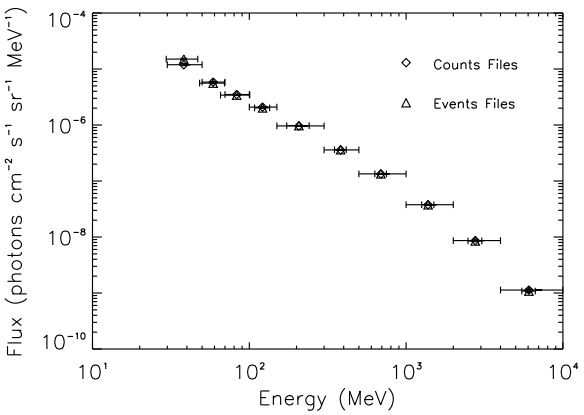

Figure 2.1: The differential flux within ten energy bins with error bars denoting energy uncertainty for events data and half-bin sizes for counts data.

We calculate the differential flux (photons cm^{-2} s^{-1} sr^{-1} MeV^{-1}) from the counts files using

$$F(E_i) = \frac{n(E_i)}{\varepsilon(E_i)\Delta E_i}, \tag{2.2}$$

where E_i is the average energy of one of the ten large energy bins, $n(E_i)$ is the number of photons within that energy bin, $\varepsilon(E_i)$ is the total exposure from the exposure files over the viewing region within that energy bin, and ΔE_i is the size of the energy bin. The quantities $n(E_i)$ and $\varepsilon(E_i)$ are both summed over all viewing periods and all positions within the region of interest. The uncertainty $\sigma_F(E_i)$ in the flux is

$$\sigma_F(E_i) = \frac{\sqrt{n(E_i)}}{\varepsilon(E_i)\Delta E_i}. \tag{2.3}$$

We assume Gaussian errors in the photon energy. The energy uncertainty is just the median of the energy uncertainties of the individual photons within that energy bin, taken from the events data.

We then constructed from the events file the photon number $n(E_i)$ in each counts-file energy bin. We found that in order to reproduce the counts data from the events file, we needed to reject photons with zenith angles greater than 100° and energy uncertainties greater than 40% of the photon energy. This zenith cut also rejects albedo gamma rays from the Earth's atmosphere. The photon differential fluxes obtained from both the counts files, and the events files (binned in the same way as the counts files) are shown in Fig. 2.1. We were not able to match the counts- and events-file photon numbers at the first energy bin to within 25%. However, for reasons discussed below, we discarded this energy bin (below 0.1 GeV) from our analysis.

We then proceeded to construct the differential flux from the events files, applying the same photon cuts, with narrower bins, to facilitate the analysis in Section 2.5. We split the data into 119 energy bins, with each bin ranging in energy from $E_{\rm min,i} = 30 \times 1.05^i$ MeV to $E_{\rm max,i} = 30 \times 1.05^{i+1}$

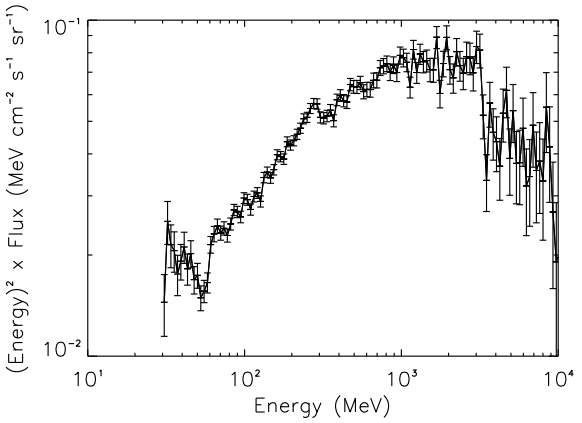

Figure 2.2: The photon differential flux using 120 energy bins.

MeV, where i ranges from 0 to 118. To calculate exposures, we interpolated $\log[\varepsilon(E_n)]$ over $\log(E_n)$, where E_n is an average energy for a large energy bin n, and $\varepsilon(E_n)$ is the same exposure for the large bin n used for the ten large bins earlier. Fig. 14 of Ref. [14] shows that the exposures do not vary rapidly for energies $\gtrsim 0.1$ GeV, and so this interpolation should be sufficient for our purposes. The flux is shown in Fig. 2.2. We note that Figs. 2.1 and 2.2 agree with EGRET's measurement of the diffuse gamma-ray spectrum in the same region of sky, shown in Fig. 4 of Ref. [51]. We also note a bump in the differential flux in Fig. 2.2 at around 3 GeV. We believe this artifact is due to the miscalibration of Class B photon events [52].

2.4 Determination of Continuum Gamma-Ray Flux

The line we seek is an excess over a continuum, and we must therefore model that continuum before we can search for an excess. Our aim in this section is thus to find a simple functional form that accurately models the continuum over the resolution scales of the instrument. A simple linear interpolation over each space of several energy-resolution elements would be sufficient, but we instead consider several astrophysically motivated functional forms, although the details of the precise astrophysical origin for the continuum are not important for our search for a line excess.

We were able to find a good fit to the continuum by a linear combination of three astrophysical sources for the diffuse gamma-ray background from the Galaxy. In the first source, nuclear interactions, cosmic rays collide with nuclei in interstellar matter to produce neutral pions, which decay mostly into gamma rays [53]. The second process is bremsstrahlung from cosmic-ray electrons interacting with interstellar matter [53]. The third, interior-point-source emission, comes from unresolved point sources within our Galaxy, such as gamma-ray pulsars [54]. We also considered exterior-point-source emission [55] and inverse-Compton scattering of interstellar radiation

from cosmic-ray electrons, but found that the first three sources listed above were sufficient to model the flux. Ref. [53] gives the differential gamma-ray production functions for the nuclear and bremsstrahlung contributions. The production functions are for the cosmic-ray spectrum in the solar neighborhood. We assumed the production functions at the Galactic center are proportional to the production functions in the solar neighborhood.

The functional form of the differential flux to which we fitted the data was $F_{\rm fit}(E) = \alpha F_{\rm nuc}(E) + \beta F_{\rm brem}(E) + \sigma F_{\rm int}(E)$, where $F_{\rm nuc}(E)$, $F_{\rm brem}(E)$, and $F_{\rm int}(E)$ are the differential photon fluxes from nuclear interactions, bremsstrahlung, and interior point sources, respectively, and α, β, and σ are amplitudes determined by fitting the data. The source functions for nuclear interactions and bremsstrahlung are

$$F_{\rm nuc}(E) = \begin{cases} 2.63\left(\frac{E}{\rm GeV}\right)^{-2.36}\exp\left[-0.45\left(\ln\left(\frac{E}{\rm GeV}\right)\right)^2\right], & 0.01\ {\rm GeV} < E < 1.5\ {\rm GeV}, \\ 3.3\left(\frac{E}{\rm GeV}\right)^{-2.71}, & 1.5\ {\rm GeV} < E < 7.0\ {\rm GeV}, \\ 4.6\left(\frac{E}{\rm GeV}\right)^{-2.86}, & E > 7.0\ {\rm GeV}, \end{cases} \tag{2.4}$$

$$F_{\rm brem}(E) = \begin{cases} 0.44\left(\frac{E}{\rm GeV}\right)^{-2.35}, & 0.01\ {\rm GeV} < E < 5.0\ {\rm GeV}, \\ 2.1\left(\frac{E}{\rm GeV}\right)^{-3.3}, & 5.0\ {\rm GeV} < E < 40\ {\rm GeV}, \end{cases} \tag{2.5}$$

where the source functions are given in units of cm^{-2} s^{-1} sr^{-1} GeV^{-1}. We assume interior point sources to be gamma-ray pulsars. Three pulsars seen by EGRET were the Crab, Geminga, and Vela pulsars, which have photon indices of -2.12, -1.42, and -1.62, respectively [54]. We approximate the photon index as having the average value of -1.7, so that

$$F_{\rm int}(E) = \left(\frac{E}{\rm GeV}\right)^{-1.7}\ {\rm cm}^{-2}\ {\rm s}^{-1}\ {\rm sr}^{-1}\ {\rm GeV}^{-1}\ . \tag{2.6}$$

The fitted flux [$F_{\rm fit}(E_i)$] and the subsequent contributions from each physical process are shown in Fig. 2.3.

2.5 Analysis of Excess Photons in Gamma-Ray Spectrum

We next construct a residual number of counts by subtracting the fitted number

$$N_{\rm fit}(E_i) = F_{\rm fit}(E_i)\varepsilon(E_i)\Delta E_i \tag{2.7}$$

from the observed number $N(E_i)$ of counts. The counts $N(E_i)$ and $N_{\rm fit}(E_i)$ are displayed in Fig. 2.4.

We take the residual spectrum to be the upper limit to the number of photons in each energy bin that could come from WIMP annihilation. However, to search for the signal we must take into

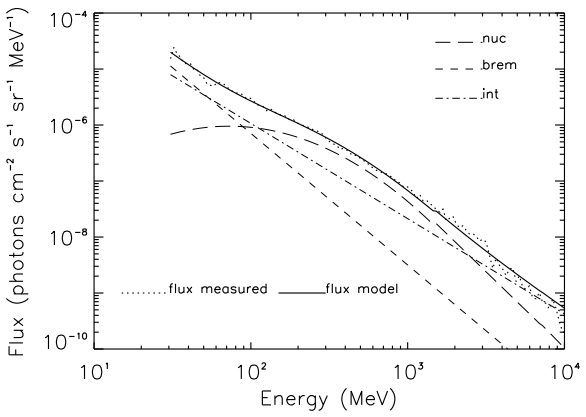

Figure 2.3: The measured and model gamma-ray flux along with contributions from nuclear interactions (nuc), bremsstrahlung (brem), and interior point sources (int).

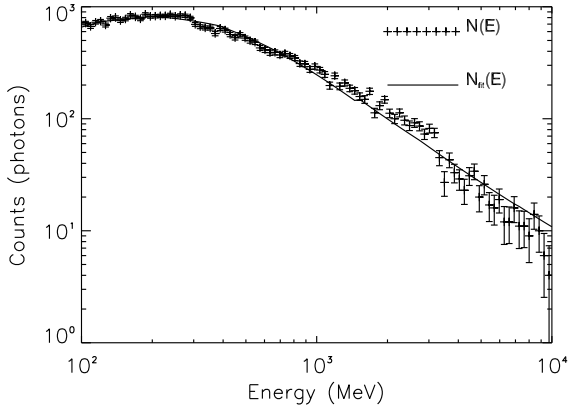

Figure 2.4: The spectrum of actual counts, $N(E_i)$, and the fitted spectrum, $N_{\rm fit}(E_i)$.

account the finite energy resolution. With infinite energy resolution, the WIMP-annihilation excess would appear as a monochromatic peak over a smooth background distribution. However, because of energy uncertainties, each photon captured by EGRET will appear to have an energy equal to its true energy plus an error, which we take to be Gaussian. Thus, monochromatic photons will be spread over neighboring energy bins. Because our bins are logarithmically spaced, the Gaussian will appear skewed, but it will still be distinguishable from the background spectrum.

Suppose our true spectrum before measurement consists of a continuum $C(E_i)$ produced by background radiation and an excess N_p of photons with energy E_p. After measurement, the continuum will change shape but remain smooth, while the excess will spread out as a Gaussian profile over multiple bins. The Gaussian skews negligibly, so we approximate the excess as a standard Gaussian.

Table 2.2: Dimensionless resolution R of EGRET at various energies

Energy (MeV)	R
100	9.42
200	11.21
500	12.39
1000	12.08
3000	11.49
10000	9.07

Thus, we model the data $D(E_i)$ as

$$D(E_i) = C(E_i) + N_p f_p(E_i), \tag{2.8}$$

where $f_p(E_i)$ is a normalized Gaussian of the form,

$$f_p(E_i) = \frac{\exp\left[-(E_i - E_p)^2/2\sigma^2_{E_p}\right]}{\sum_l \exp\left[-(E_l - E_p)^2/2\sigma^2_{E_p}\right]}. \tag{2.9}$$

In Eq. (2.9), the denominator is summed over all energy bins within $3\sigma_{E_p}$ of the Gaussian central energy E_p. The energy uncertainty σ_{E_p} at energy E_p, is given by

$$\sigma_{E_p} = \frac{E_p}{R(E_p)}, \tag{2.10}$$

where $R(E_p)$ is the dimensionless resolution at energy E_p. The fractional full-width at half-maximum (% FWHM), or $\sqrt{2\ln 2}$ times twice the reciprocal of the resolution, is shown for various energies in Fig. 20 in Ref. [14]. From the % FWHM, we produce a table of resolution vs. energy, shown in Table 2.2. We calculate the resolution at each energy by interpolating $\log[R(E)]$ over $\log(E)$. Because the first value for R given in Table 2.2 is for energy $E = 100$ MeV, we cannot extrapolate $\log(R)$ to lower energies with certainty. Therefore, we restrict our analysis to the energy interval 0.1 GeV–10 GeV.

The number $N_p(E_i)$ can be deduced at each energy bin in the spectrum by solving Eq. (2.8) for N_p, assuming $D(E_i)$, $C(E_i)$, and $f_p(E_i)$ are known. Each $N_p(E_i)$ has an uncertainty,

$$\sigma_{N_p}(E_i) = \frac{\sqrt{C(E_i)}}{f_p(E_i)}, \tag{2.11}$$

due to continuum fluctuations. Most bins in the spectrum contain large numbers of photons. Therefore, we average N_p using Gaussian statistics to calculate $\overline{N}_p$ and $\sigma_{\overline{N}_p}$, the value and uncertainty of the excess, for each energy bin E_p greater than 100 MeV. The resulting ratio of $\overline{N}_p$ to $\sigma_{\overline{N}_p}$ is shown

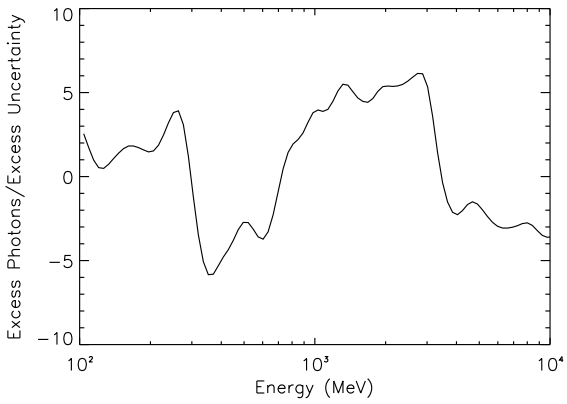

Figure 2.5: Ratio of excess photons to the excess uncertainty.

in Fig. 2.5.

Fig. 2.5 does show statistically significant deviations of the data from our model for the continuum. To determine if this residual favors the Gaussian model, we compare χ^2 for a Gaussian model to χ^2 for a constant-excess model. We calculate χ^2 for both models over a $\pm 3\sigma_{E_p}$ range centered at the excess center. The Gaussian is $\overline{N}_p f_p$. We also compare the residual with a constant excess N_c, where dN_c/dE is constant and N_c is proportional to the energy-bin size. We normalize N_c such that the lowest energy bin $3\sigma_{E_p}$ from the Gaussian center has 10 photons. We compared χ^2 for the excess at energies $E = 210$ MeV and $E = 2000$ MeV, two energies that have high excess-photons-to-excess-uncertainty ratios (see Fig. 2.5). At both energies we found χ^2 to be smaller for the constant excess, a simpler model, than for the Gaussian. Thus, we show that the residual does not favor the Gaussian model, and we do not attribute any of these deviations to a WIMP-annihilation line (see Fig. 2.6). Rather, it appears that there is some continuum contribution that our analysis has not taken into account.

We therefore use $\overline{N}_p$ to calculate an upper limit to the line flux. This line flux is different from the differential flux used in previous sections in that this flux is not divided by the energy bin size. Since $\overline{N}_p$ has positive and negative values, we take the 2σ upper limit to the line flux $\Phi_u(E_p)$ to be

$$\Phi_u(E_p) = \begin{cases} (\overline{N}_p + 2\sigma_{\overline{N}_p})/\varepsilon(E_i), & \overline{N}_p \geq 0, \\ 2\sigma_{\overline{N}_p}/\varepsilon(E_i), & \overline{N}_p < 0. \end{cases} \tag{2.12}$$

The 2σ upper limit to the line flux is shown in Fig. 2.7.

We illustrate the reliability of the upper limit to the line flux by repeating the analysis in Section 2.5 for a sliding-window continuum model. At each energy bin E_i we fitted the diffuse flux data within 3 to $9\sigma_{E_i}$ of E_i to a single power law. The amplitude and index of the power law, which varied with energy bin, were then used to construct the background radiation continuum $C(E_i)$ in

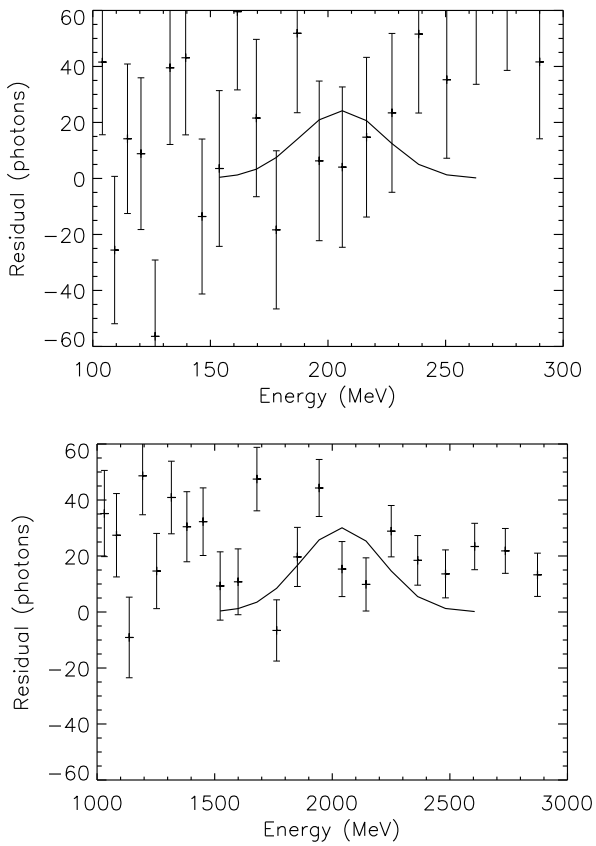

Figure 2.6: The residual number of counts (crosses) and the expected Gaussian (solid curve) from a smeared line excess. The top panel shows the residual and Gaussian at $E = 210$ MeV, while the bottom panel shows the same at $E = 2000$ MeV. The ratio of excess photons to excess uncertainty is high at these energies. Notice in both panels the residual does not resemble the Gaussian. For $E = 210$ MeV and $E = 2000$ MeV, respectively, χ^2 for the Gaussian is 17.3 and 38.0 and χ^2 for the constant excess is 11.0 and 23.9. Thus, the Gaussian model is not favored.

Section 2.5 needed to search for a line excess. No significant excess was found, and an upper limit to the line flux was determined. This 2σ upper limit, shown in Fig. 2.7, agrees quite well with the previous upper limit in Section 2.5 except around 3 GeV, where the previous upper bound is more conservative. To be conservative, we chose the upper limit to the line flux from the multi-component continuum fits, for the rest of our analysis.

2.6 Upper Limits to the Annihilation Cross Section

If WIMPs comprise the Galactic halo, then the flux of line photons from WIMP annihilation is (for Majorana WIMPs)

$$\Phi(E_\gamma = m_\chi) = \frac{\langle \sigma v \rangle_{\gamma\gamma}}{4\pi m_\chi^2} \int_{l.o.s} \rho_\chi^2 \, dl, \tag{2.13}$$

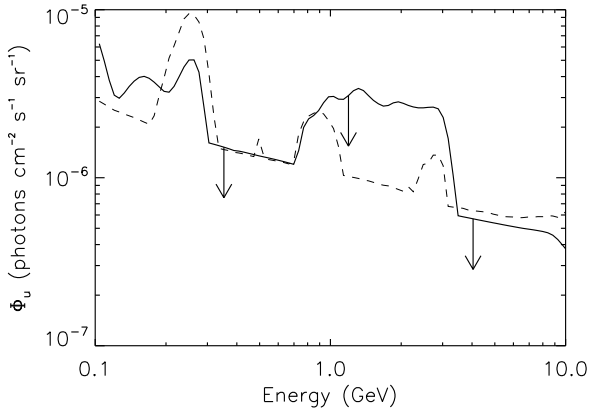

Figure 2.7: Upper limits to the line flux Φ_u from the Galactic center. The solid line is the upper limit derived from the continuum model in Section 2.4. The dashed line is the upper limit derived from the sliding window technique.

where Φ is the line flux of photons in units of photons cm^{-2} s^{-1} sr^{-1}, $\langle\sigma v\rangle_{\gamma\gamma}$ is the velocity-averaged cross section for the WIMP to annihilate to two photons, m_χ is the WIMP mass (which is equal to the photon energy E_γ), and ρ_χ is the density profile of the WIMP halo. The integral is along the line of sight, and dl is the differential distance along the line of sight. The residual in the previous section gives the average line-of-sight line flux within a $10^\circ \times 10^\circ$ region around the Galactic center. Therefore, we integrate Eq. (2.13) over our viewing region to find the relation between $\langle\sigma v\rangle_{\gamma\gamma}$ and m_χ.

The density profile of the WIMP halo must be known in order to integrate Eq. (2.13). The functional form of the halo density profile is motivated by theory and simulations, with parameters chosen for consistency with the measured Milky Way rotation curve. We assume the following parametrization of the density profile,

$$\rho(r) = \rho_0 \frac{(r_0/a)^\gamma [1 + (r_0/a)^\alpha]^{(\beta-\gamma)/\alpha}}{(r/a)^\gamma [1 + (r/a)^\alpha]^{(\beta-\gamma)/\alpha}}. \tag{2.14}$$

Here, ρ_0 is the local density of the halo at the solar system; r_0 is the distance from the solar system to the Galactic center, which we take to be 8.5 kpc; a is the core radius; and α, β, and γ are parameters that determine the halo model. Various combinations of α, β, and γ have been used in simulations and are of particular interest. We chose to study the Ka and Kb profiles proposed by Kravtsov et al. [56]; the NFW profile proposed by Navarro, Frenk, and White [49]; and the modified isothermal profile, or Iso, which is commonly used. These profiles are listed in Table 2.3. The quantities ρ_0 and a are chosen for each profile so that the profile will account for the Galactic rotation curve. These values are taken from Fig. 5 in Ref. [57]. We insert each of these profiles into Eq. (2.13) and integrate over our viewing region to find the line flux Φ in terms of $\langle\sigma v\rangle_{\gamma\gamma}$ and m_χ.

Table 2.3: Parameters for each profile type.

Profile	α	β	γ	ρ_0 (GeV/cm^3)	a (kpc)
Ka	2	3	0.2	0.4	11
Kb	2	3	0.4	0.4	12
NFW	1	3	1	0.3	25
Iso	2	2	0	0.3	4

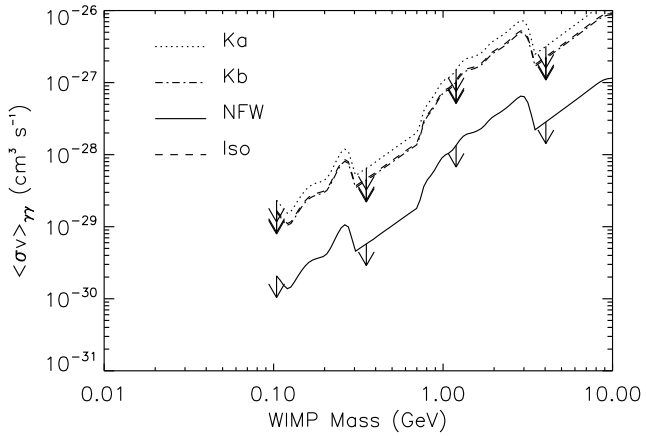

Figure 2.8: The 2σ upper limits to the velocity-averaged annihilation cross section $\langle\sigma v\rangle_{\gamma\gamma}$ as a function of WIMP mass for various halo-density profiles.

The resulting upper limit to the annihilation cross section $\langle\sigma v\rangle_{\gamma\gamma}$ is shown in Fig. 2.8 as a function of WIMP mass m_χ for each halo model listed in Table 2.3.

2.7 Discussion

To illustrate the possible utility of this new bound, we consider a toy model in which WIMPs are Majorana fermions that couple to electrons via exchange of a scalar boson (the U boson [58, 59]) of mass m_U (assumed to be much heavier than both WIMPs and electrons) through the Lagrangian density,

$$\mathcal{L} = \frac{C_U f_{A\,e}}{2m_U^2}\overline{\chi}\gamma_\mu\gamma_5\chi\overline{\psi_e}\gamma^\mu\gamma_5\psi_e, \tag{2.15}$$

where C_U and $f_{A\,e}$ are axial couplings of the U boson to the WIMP field χ and the electron field ψ_e, respectively. Annihilation of WIMPs with O(MeV) masses to electron-positron pairs has been considered as a possible explanation [46] for the observed flux, $\Phi_{511} = 9.9^{+4.7}_{-2.1} \times 10^{-4}$ photons cm^{-2} s^{-1} [48], of 511-keV photons as measured at the Galactic center by the SPI camera on the INTEGRAL satellite. In this scenario, positrons from WIMP annihilation then annihilate with electrons in the IGM to produce these 511-keV photons. The annihilation rate—and therefore the

cross section for annihilation to electron-positron pairs, and thus the coupling $C_U f_{A\,e}/m_U^2$—are determined by the flux of 511-keV photons. More precisely, the 511-keV flux determines an upper bound to this annihilation rate, cross section, and coupling, but we will here suppose the entire 511-keV flux to be from positrons from WIMP annihilation.

Ref. [60] pointed out that if WIMPs annihilate to electron-positron pairs, they can also undergo annihilation to an electron-positron-photon three-body final state, a process we refer to as internal bremsstrahlung. If $\langle\sigma v\rangle_{e^+e^-}$ is the cross section for annihilation to electron-positron pairs (as calculated, e.g., in Refs. [58, 59, 61]), then the differential cross section for bremsstrahlung of a photon of energy E_γ is

$$\frac{d\langle\sigma v\rangle_{\rm Br}}{dE_\gamma} = \langle\sigma v\rangle_{e^+e^-}\frac{\alpha_e}{\pi}\frac{1}{E_\gamma}\left[\ln\left(\frac{s'}{m_e^2}\right)-1\right]\left[1+\left(\frac{s'}{s}\right)^2\right], \tag{2.16}$$

where $s = 4m_\chi^2$, $s' = 4m_\chi(m_\chi - E_\gamma)$, and α_e is the fine-structure constant. The quantity $E_\gamma^2 d\langle\sigma v\rangle_{\rm Br}/dE_\gamma$ increases roughly linearly with E_γ for $E_\gamma < m_\chi$ and peaks at a value (for our WIMP mass range of 0.1–10 GeV) less than 10% smaller than the WIMP mass. The measured upper limits to the flux were approximated in Ref. [60] $E_\gamma^2 d\Phi_{\rm Br}/dE_\gamma \lesssim 7\times10^{-3}$ MeV cm^{-2} s^{-1} sr^{-1} over the energy range 1–100 MeV. This flux was averaged over a region on the sky centered at the Galactic center from $-30°$ to $30°$ Galactic longitude and $-5°$ to $5°$ Galactic latitude. For the purposes of this illustrative exercise, we extend this bound up to 10 GeV (roughly consistent with the line limit we have derived).

Each annihilation to an electron-positron pair produces two 511-keV photons either directly (7% of all annihilations) or by producing positronium and decaying (23.3% of all annihilations); the rest produce noncontributing continuum photons [60, 62]. The resulting flux of 511-keV photons is (for Majorana particles)

$$\Phi_{511} = \frac{\xi\langle\sigma v\rangle_{e^+e^-}}{4\pi m_\chi^2}\int \rho_\chi^2\, dl\, d\Omega, \tag{2.17}$$

where $\xi = 0.303$ is the fraction of positrons that undergo two-photon annihilation, the dl integral is along the line of sight and the $d\Omega$ integral is over the SPI camera's field of view, a 16°-diameter circle around the Galactic center. Likewise, the differential flux of photons from internal bremsstrahlung is

$$\frac{d\Phi_{\rm Br}}{dE_\gamma} = \frac{d\langle\sigma v\rangle_{\rm Br}/dE_\gamma}{8\pi m_\chi^2\Delta\Omega}\int \rho_\chi^2\, dl\, d\Omega, \tag{2.18}$$

where $\Delta\Omega \simeq 0.182$ sr is the solid angle over the $60°$ by $10°$ Galactic region mentioned earlier.

The two-photon annihilation cross section $\langle\sigma v\rangle_{\gamma\gamma}$ for the Lagrangian of Eq. (2.15) is given by [63]

$$\langle\sigma v\rangle_{\gamma\gamma} = \frac{\alpha_e^2 m_\chi^2 C_U^2 f_{A\,e}^2}{\pi^3 m_U^4}\left|I(\xi_e)\right|^2, \tag{2.19}$$

where $\xi_e = m_e^2/m_\chi^2$, $I(\xi_e) = \frac{1}{2}\left[1 + \xi_e J(\xi_e)\right]$, and $J(\xi_e)$ is given by

$$J(\xi_e) = \left(\frac{1}{2}\ln\frac{1+\sqrt{1-\xi_e}}{1-\sqrt{1-\xi_e}} - \frac{i\pi}{2}\right)^2, \tag{2.20}$$

for $\xi_e \leq 1$. For our WIMP mass range 0.1–10 GeV, $\xi_e \ll 1$ and $I(\xi_e) \simeq 1/2$. The cross section for annihilation to electron-positron pairs $\langle\sigma v\rangle_{e^+e^-}$ is given by [59, 61]

$$\langle\sigma v\rangle_{e^+e^-} = \frac{C_U^2 f_{A\,e}^2}{2\pi m_U^4}\left[\frac{4}{3}m_\chi^2\overline{v_\chi^2} + m_e^2\right], \tag{2.21}$$

where $\overline{v_\chi^2} = \frac{3}{4}v_c^2$ is the mean-square center-of-mass velocity and $v_c \simeq 220$ km/s is the WIMP rotation speed, assuming the electron energy $E_e = m_\chi \gg m_e$ and $m_U \gg m_\chi$. We use Eqs. (2.19) and (2.21) to derive upper limits to the coupling $C_U f_{A\,e}/m_U^2$ appearing in the Lagrangian of Eq. (2.15).

Fig. 2.9 shows the upper limit, assuming an NFW halo-density profile, to the coupling $C_U f_{A\,e}/m_U^2$ from measurements of the 511-keV line [46], the limit to the bremsstrahlung-photon flux [60], and our 2σ limit to the line-photon flux. We see that for the model assumptions and WIMP mass range considered here, the limit to the two-photon annihilation cross section derived from our 2σ limit to the line-photon flux is the strongest of these three. At first, this result may seem surprising, given that the two-photon annihilation process is higher order in α_e, but this suppression is counteracted by the helicity suppression of the cross section for annihilation of Majorana fermions to electron-positron pairs. Refs. [64, 65] considered also gamma-rays from in-flight annihilation from e^+e^- pairs, but their analysis was restricted to energies < 100 MeV.

Of course, the 2σ limit to the line-photon flux may not always provide the best limit to the two-photon annihilation cross section for every WIMP model. It may well be that other models—e.g., those in which the dark-matter particle is a scalar [66]—can produce a ratio of 511-keV photons to line photons large enough to cause the 511-keV limit to supersede the line photon limit.

Acknowledgments

We thank S. Profumo for useful discussions and comments and J. Beacom for useful comments on an earlier draft. ARP was supported by an NSF Graduate Fellowship. RC was partially funded under NASA contract 1407. MK was supported by DoE DE-FG03-92-ER40701, NASA NNG05GF69G, and the Gordon and Betty Moore Foundation.

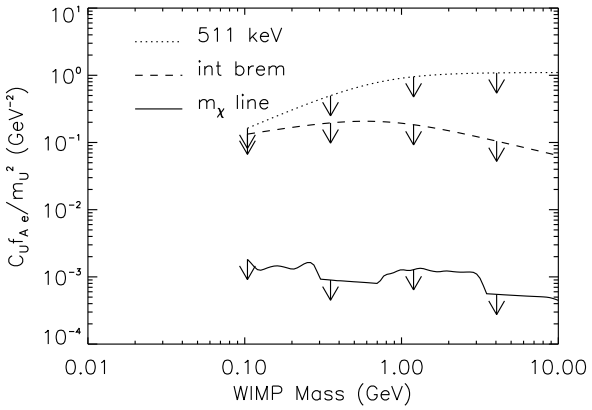

Figure 2.9: Upper limits to the ratio $C_U f_{Ae}/m_U^2$ as a function of WIMP mass for the NFW halo-density profile. The limits were calculated from the observed 511 keV emission, the constraints on internal bremsstrahlung, and our derived limit to the line photon flux.

Chapter 3

Cosmic Microwave Background Statistics for a Direction-Dependent Primordial Power Spectrum

3.1 Introduction

It is well known that the homogeneity and isotropy of the universe are only approximate. There are departures from homogeneity and isotropy that are now well-quantified by measurements of the cosmic microwave background (CMB) and galaxy surveys. In current cosmological theory, the notions of homogeneity and isotropy have been superseded by the notions of *statistical* homogeneity and isotropy. The density of matter may differ from one point in the universe to another, but the distribution of matter is described as a realization of a random field with a variance that is everywhere the same and the same in every direction. This is generally the prediction of structure-formation models, and in particular, of inflationary models.

Still, statistical isotropy and homogeneity are assumptions that can be tested quantitatively, and the precision with which they can be tested is improving rapidly with the still-accumulating wealth of cosmological data. Preliminary (and controversial) indications for a preferred direction in the CMB [15, 16, 17, 18] have recently motivated the study of departures from statistical isotropy. Subsequent theoretical work has shown that although statistical isotropy is a generic prediction of inflation, inflation models can in fact be constructed to violate statistical isotropy [19, 20, 21, 22, 23, 24, 25, 26, 27, 28]. Dark-energy models might also accommodate departures from statistical isotropy [29, 30]. These models provide useful straw men against which the success of the standard inflationary predictions of statistical isotropy can be quantified.

[0]The material presented in this chapter was first published in *Cosmic microwave background statistics for a direction-dependent primordial power spectrum*, Anthony R. Pullen and Marc Kamionkowski, Phys. Rev. D **76**, 103529 (2007). Reproduced here with permission, copyright (2007) by the American Physical Society.

The growing interest in such models motivates us to study generalized tests for statistical isotropy. In a statistically isotropic universe, the primordial distribution of matter is a realization of a random field in which Fourier modes of the density field have variances, a power spectrum $P(\mathbf{k})$, that depend only on the magnitude k of the wavevector $\mathbf{k}$. If we drop the assumption of statistical isotropy, the power spectrum will depend on the direction $\hat{\mathbf{k}}$ as well. If $\delta(\mathbf{k})$ is the Fourier amplitude of the fractional density perturbation, then the power spectrum is defined by

$$\langle \delta(\mathbf{k})\delta^*(\mathbf{k}')\rangle = \delta_D(\mathbf{k}-\mathbf{k}')P(\mathbf{k}), \tag{3.1}$$

where the angle brackets denote an average over all realizations of the random field, and δ_D is a Dirac delta function; note that we are still preserving the assumption that different Fourier modes are uncorrelated. The most general power spectrum can then be written,

$$P(\mathbf{k}) = A(k)\left[1+\sum_{LM} g_{LM}(k)Y_{LM}(\hat{\mathbf{k}})\right], \tag{3.2}$$

where $Y_{LM}(\hat{\mathbf{k}})$ (with $L \geq 2$) are spherical harmonics, and $g_{LM}(k)$ quantify the departure from statistical isotropy as a function of wavenumber k. Since the density field is real, Fourier modes for $\mathbf{k}$ are related to those of $-\mathbf{k}$, in such a way that the multipole moment L must be even. In the limit $g_{LM}(k) \to 0$, we recover the usual statistically isotropic theory with power spectrum $A(k)$. The implementation, Eq. (3.2), of power anisotropy is motivated in part by the inflationary model of Ref. [24], which predicts $g_{2M}(k) \neq 0$.

Here we consider several CMB tests for statistical isotropy. The first, which we refer to as "power multipole moments", is a simple and intuitive estimator that involves measurement of the multipole moments of the square of the temperature/polarization fields.[1] As an example, we apply this statistic to an inflationary model [24] that predicts a quadrupole in the matter power spectrum.

Although power multipole moments provide a nice model-independent test for departures from statistical isotropy, more sensitive probes can be developed if the particular form of the departure is specified. To illustrate, we thus construct the minimum-variance estimators for the anisotropy coefficients $g_{LM}(k)$ under the assumption that they are constants. The naive power multipole moments, although intuitively simple, co-add a number of modes with equal weight. The minimum-variance estimator co-adds modes with weights that depend on their signal-to-noise, so that (as the name suggests) the variance of the estimator is minimized. We show that this statistic provides a far stronger probe for the g_{LM}s.

The plan of this chapter is as follows: Section 3.2 reviews some CMB basics. Section 3.3 calcu-

[1] There has already been some evidence for a dipole in the CMB power [16, 18] that is analogous to the higher multipole moments that we are considering here, but which cannot be due to anisotropy in the primordial power spectrum because it has $L = 1$. There have also been searches [17] for anisotropy along the lines considered here, and Ref. [67, 68] discusses similar statistics.

lates the correlations of CMB spherical-harmonic coefficients if there are departures from statistical isotropy. As we discuss there, the power spectrum C_l, which describes the two-point CMB statistics if there is statistical isotropy, is generalized to a set of moments $D_{ll'}^{LM}$ if statistical isotropy is broken. In Section 3.4, we introduce and calculate the power multipole moments and calculate the standard errors with which these moments can be recovered. We apply this statistic to a quadrupole in the matter power spectrum, calculating the sensitivities of several CMB experiments to such a quadrupole. Section 3.5 discusses minimum-variance estimators for the quantities $D_{ll'}^{LM}$ that parametrize the departures $g_{LM}(k)$ from statistical isotropy. We then construct from these the minimum-variance estimators for the quadrupole moments of the primordial power spectrum, calculate their variance, and evaluate their sensitivity to departures from statistical isotropy. We make some concluding remarks in Section 3.6. Throughout the main body of the chapter, we discuss statistics for only a temperature map, in order to make the presentation clear. Appendix A generalizes to include the full temperature-polarization information. Our numerical results are for a full temperature-polarization map, as well as for temperature or polarization alone.

3.2 Preliminaries

A CMB experiment provides the temperature $T(\hat{\mathbf{n}})$ as a function of position $\hat{\mathbf{n}}$ on the sky. The map $T(\hat{\mathbf{n}})$ can be expanded in terms of spherical harmonics $Y_{lm}(\hat{\mathbf{n}})$,

$$a_{lm} = \frac{1}{T_0} \int d\hat{\mathbf{n}}\, Y_{lm}^*(\hat{\mathbf{n}}) T(\hat{\mathbf{n}}). \tag{3.3}$$

The a_{lm}s are Gaussian random variables, and if there is statistical isotropy, then they are statistically independent for different l and m: $\langle a_{lm} a_{l'm'}^* \rangle = C_l \delta_{ll'} \delta_{mm'}$.[2] The set of C_ls is the CMB temperature power spectrum. We will see that when statistical isotropy is violated, there are correlations induced between a_{lm}s for different l and m [24]. If there is statistical isotropy, the two-point autocorrelation function is

$$\begin{aligned} C(\hat{\mathbf{n}}, \hat{\mathbf{n}}') &= \langle T(\hat{\mathbf{n}}) T(\hat{\mathbf{n}}') \rangle \\ &= T_0^2 \sum_l \frac{2l+1}{4\pi} C_l P_l(\hat{\mathbf{n}} \cdot \hat{\mathbf{n}}'); \end{aligned} \tag{3.4}$$

i.e., the correlation function depends only on the separation between the two points. If statistical isotropy is violated, this is not necessarily true.

[2]Strictly speaking, it is not the a_{lm}s that are statistically independent, but rather their real and imaginary parts.

3.3 Off-Diagonal Correlations for Anisotropic Power

Consider a primordial matter power spectrum $P(\mathbf{k})$ given by Eq. (3.2). We expand $T(\hat{\mathbf{n}})$ in $\mathbf{k}$ space in the form,

$$\frac{T}{T_0}(\hat{\mathbf{n}}) = \int d^3k \sum_l (-i)^l (2l+1) P_l(\hat{\mathbf{k}}\cdot\hat{\mathbf{n}}) \delta(\mathbf{k}) \Theta_l(k), \tag{3.5}$$

where $\Theta_l(k)$ is the contribution to the lth temperature moment from wavevector $\mathbf{k}$. With these conventions, $\Theta_l(k)$ is real. With our expression, Eq. (3.2), we can write the covariance matrix as

$$\langle a_{lm} a^*_{l'm'} \rangle = \delta_{ll'}\delta_{mm'} C_l + \sum_{LM} \xi^{LM}_{lml'm'} D^{LM}_{ll'}. \tag{3.6}$$

Here, the set of C_ls, given by

$$C_l = (4\pi)^2 \int_0^\infty dk\, k^2 A(k) [\Theta_l(k)]^2, \tag{3.7}$$

is the usual CMB power spectrum for the case of statistical isotropy. Departures from statistical isotropy introduce the second term, where

$$D^{LM}_{ll'} = (4\pi)^2 (-i)^{l-l'} \int_0^\infty dk\, k^2 A(k) g_{LM}(k) \Theta_l(k) \Theta_{l'}(k), \tag{3.8}$$

and

$$\begin{aligned} \xi^{LM}_{lml'm'} &= \int d\hat{\mathbf{k}}\, Y^*_{lm}(\hat{\mathbf{k}}) Y_{l'm'}(\hat{\mathbf{k}}) Y_{LM}(\hat{\mathbf{k}}) \\ &= (-1)^{m'} \left(G^L_{ll'}\right)^{1/2} C^{LM}_{lml',-m'}, \end{aligned} \tag{3.9}$$

where $C^{LM}_{lml'm'}$ are Clebsch-Gordan coefficients, and

$$G^L_{ll'} \equiv \frac{(2l+1)(2l'+1)}{4\pi(2L+1)} \left(C^{L0}_{l0l'0}\right)^2. \tag{3.10}$$

Throughout, we use upper-case indices LM for power anisotropies, and lower-case indices lm for temperature/polarization anisotropies. For L even, $\xi_{lml'm'}$ are nonvanishing only for $l-l'$ even, and so the $D^{LM}_{ll'}$ are real. Eqs. (3.8) and (3.9) agree with similar results in Ref. [68], and they recover the results of Ref. [24] for $L = 2$.

If primordial perturbations are statistically isotropic and Gaussian, then the statistics of the CMB temperature map are specified fully by the power spectrum, the set of C_ls. If primordial perturbations have a departure from statistical isotropy that can be written in terms of spherical harmonics $Y_{LM}(\hat{\mathbf{k}})$, then the two-point statistics are described additionally by the set of multi-

pole moments $D_{ll'}^{LM}$. These quantities are thus the generalization of the C_ls if there is statistical anisotropy.

3.4 Power Multipole Moments

3.4.1 Theoretical predictions

It is natural to expect that a spherical-harmonic pattern of anisotropy in the matter power spectrum manifests itself in a similar pattern in the CMB power. It is thus natural to consider a set of "power multipole moments",

$$b_{LM} = \frac{1}{T_0^2} \int d\hat{\mathbf{n}}\, Y_{LM}^*(\hat{\mathbf{n}}) \left\langle T^2 \right\rangle (\hat{\mathbf{n}}), \tag{3.11}$$

where $\left\langle T^2 \right\rangle (\hat{\mathbf{n}}) = C(\hat{\mathbf{n}}, \hat{\mathbf{n}})$ is the expectation value of the square of the temperature at position $\hat{\mathbf{n}}$ in the sky; it is the autocorrelation function at zero lag. With this statistic, we simply look for anisotropies in the power. These statistics have several advantages. In addition to having a form familiar from similar statistics [e.g., Eq. (3.3)] for temperature fluctuations, they have simple analytic expressions in terms of $P(\mathbf{k})$. There are also (as we show below), relatively simple expressions for the cosmic-variance– and instrumental-noise–induced errors in the measurement of these statistics.

The variance $\left\langle T^2 \right\rangle (\hat{\mathbf{n}})$ as a function of position $\hat{\mathbf{n}}$ is given by

$$\frac{\left\langle T^2 \right\rangle (\hat{\mathbf{n}})}{T_0^2} = \sum_{lml'm'} \left\langle a_{lm} a_{l'm'}^* \right\rangle Y_{lm}(\hat{\mathbf{n}}) Y_{l'm'}^*(\hat{\mathbf{n}}). \tag{3.12}$$

We put this into Eq. (3.11) and use

$$\sum_{mm'} C_{lml,-m'}^{LM} C_{lml',-m'}^{L'M'} = \delta_{LL'} \delta_{MM'}, \tag{3.13}$$

to obtain (for $L \geq 2$)

$$b_{LM} = \sum_{ll'} G_{ll'}^{L} D_{ll'}^{LM}. \tag{3.14}$$

3.4.2 Statistical noise

We now calculate the standard error, due to cosmic variance and instrumental noise, with which the power multipole moments can be measured. To do so, we consider a full-sky map $T^{\rm map}(\hat{\mathbf{n}})$ of the temperature in $N_{\rm pix}$ equal-area pixels. The temperature in each pixel receives contributions from signal and from noise. Thus, in pixel i, $T^{\rm map} = T(\hat{\mathbf{n}}_i) + T_i^{\rm n}$, where $T(\hat{\mathbf{n}}_i)$ is the temperature measured in pixel i, which will be the signal temperature smoothed by a Gaussian beam of full-width half-maximum (FWHM) $\theta_{\rm fwhm}$, plus a noise $T_i^{\rm n}$. We assume that the noise is isotropic and that the noises in different pixels are uncorrelated with variance σ_T^2: i.e., $\left\langle T_i^{\rm n} T_j^{\rm n} \right\rangle = \sigma_T^2 \delta_{ij}$. The power spectrum for

the map is thus $C_l^{\rm map} = |W_l|^2 C_l + C_l^{\rm n}$, where $C_l^{\rm n} = (4\pi/N_{\rm pix})\sigma_T^2$ is the noise power spectrum, and W_l is a window function that takes into account the effects of beam smearing; for a Gaussian beam of FWHM $\theta_{\rm fwhm}$, it is $W_l = \exp(-l^2\sigma_b^2/2)$ with $\sigma_b = \theta_{\rm fwhm}/\sqrt{8\ln 2} = 0.00742(\theta_{\rm fwhm}/1^\circ)$.

Since the instrumental noise is isotropic by assumption, we get an unbiased estimator for b_{LM} (for $L \geq 2$) from

$$\widehat{b}_{LM}^{\rm map} = \frac{1}{T_0^2}\int d\hat{\mathbf{n}}\, Y_{LM}^*(\hat{\mathbf{n}})\,[T^{\rm map}(\hat{\mathbf{n}})]^2\,. \tag{3.15}$$

Cosmic variance and instrumental noise induce a variance in the b_{LM}s, which we define as

$$\Xi^{LM} \equiv \left\langle \widehat{b}_{LM}\widehat{b}_{LM}\right\rangle, \tag{3.16}$$

where we have assumed the null hypothesis, $g_{LM} = 0$. For this null hypothesis of a statistically isotropic Gaussian random map,

$$\begin{aligned}\Xi^{LM} &= \frac{2}{T_0^4}\int d\hat{\mathbf{n}}\, d\hat{\mathbf{n}}'\, C^{\rm map}(\hat{\mathbf{n}},\hat{\mathbf{n}}')C^{\rm map}(\hat{\mathbf{n}},\hat{\mathbf{n}}') \\ &\quad \times Y_{LM}(\hat{\mathbf{n}})Y_{LM}^*(\hat{\mathbf{n}}') \\ &= 2\sum_{ll'} G_{ll'}^L C_l^{\rm map} C_{l'}^{\rm map}\end{aligned} \tag{3.17}$$

where $C^{\rm map}(\hat{\mathbf{n}}_1,\hat{\mathbf{n}}_2)$ is the two-point correlation function for the *map*, obtained from the expression, Eq. (3.4), for the correlation function by replacing C_l by $C_l^{\rm map}$, and we have used $\sum_{mm'}(C_{lml'm'}^{LM})^2 = 1$. Note that the absence of any M dependence of $\Xi_{\rm AA'}^{LM}$ is as we expected. Moreover, it follows from Eq. (3.13) that the estimators for the different b_{lm}s are uncorrelated: $\left\langle \widehat{b}_{LM}\widehat{b}_{L'M'}\right\rangle \propto \delta_{LL'}\delta_{MM'}$.

Given a power spectrum of the form Eq. (3.2), specified by the functions $g_{LM}(k)$, predictions for the $b_{LM}^{\rm map}$ can be evaluated with Eq. (3.14) replacing $D_{ll'}^{LM}$ in that equation by $D_{ll'}^{LM,{\rm map}} = D_{ll'}^{LM} W_l W_{l'}$ and evaluating the $D_{ll'}^{LM}$ with Eq. (3.8). The $b_{LM}^{\rm map}$ can then be measured using Eq. (3.15) with variances given by Eq. (3.17).

3.4.3 A worked example

As a simple example, suppose the $g_{LM}(k)$ are constants, independent of k. We can then take g_{LM} outside the integral in Eq. (3.8). An estimator for g_{LM} is then $\widehat{g}_{LM} = \widehat{b}_{lm}^{\rm map}/(b_{lm}^{\rm map}/g_{LM})$. Defining $F_{ll'} \equiv D_{ll'}^{LM}/g_{LM}$ for this case, the variance with which each g_{LM} can be measured is then

$$\sigma_{g_{LM}}^2 = \frac{2\sum_{ll'} G_{ll'}^L C_l^{\rm map} C_{l'}^{\rm map}}{\left[\sum_{ll'} G_{ll'}^L F_{ll'} W_l W_{l'}\right]^2}. \tag{3.18}$$

Moreover, the measured g_{LM} are statistically independent as a consequence of the statistical independence of the $\widehat{b}_{LM}$.

To illustrate, we apply this result to an inflationary model [24] that has a power spectrum with a quadrupole dependence on the angle.[3] We use the $\Theta_l(k)$ calculated by CMBFAST [69] to obtain $F_{ll'}$. We assume only scalar perturbations and the current best-fit cosmological parameters.

The numerical results are given in Table 3.1, but before reviewing them, we provide some very rough estimates to get some feel for the numbers. To do so, ignore instrumental noise and suppose that $W_l = 1$ for all $l \leq l_{\rm max}$. For $L = 2$, $F_{ll'} \neq 0$ only for $l' = l$ or $l' = l \pm 2$. Moreover, for these combinations of ll' and for $l \gg 2$, we approximate the numerical results (which we use for the numerical results in the table) for $F_{ll'}$ as $F_{l,l+2} \simeq -0.5\, C_l$. Also, $(C^{20}_{l0l0})^2 \sim (5/8) l^{-1}$ for $l \gg 1$, and $(C^{20}_{l0(l\pm2)0})^2$ is 1.5 times as large. Eq. (3.18) can then be approximated $\sigma^2_{g_{2M}} \sim 256\pi [\sum_l l (C_l)^2]/[\sum_l l C_l]^2$. If the power spectrum has the form $C_l \propto l^{-2}$ (a *very* rough approximation to the temperature power spectrum for $l \lesssim 1000$), then $\sigma^2_{g_{2M}} \sim 128\pi l^{-2}_{\rm min} [\ln(l_{\rm max}/l_{\rm min})]^{-2}$. For example, using $l_{\rm min} = 2$ and $l_{\rm max} = 1000$ yields $\sigma_{g_{2M}} \sim 1.23$.

Of course, there is nothing about the derivation of Eq. (3.18) that is specific to a temperature map, and this result can be applied equally well, e.g., to the E-mode polarization. If we approximate the polarization power spectrum by $C_l \sim$ const, then we find $\sigma^2_{g_{2M}} \simeq 512\pi l^{-2}_{\rm max}$, or $\sigma_{g_{2M}} \sim 5 \times 10^{-2}$ for $l_{\rm max} \simeq 1000$.

We now return to the numerical results for $\sigma_{g_{2M}}$ listed in Table 3.1 for the Wilkinson Anisotropy Probe (WMAP) [32], which has now collected three years of data, the Planck satellite [33], to be launched in 2008, and EPIC [70], a satellite mission currently under study. The parameters assumed for each model are listed, as well as results obtained using Eq. (3.14) assuming only TT is used or EE only. Appendix A generalizes Eq. (3.14) to the case where the full temperature-polarization is used (including the TE correlation), and we present numerical results for this case in the Table as well. We also list results, labeled "CVO" (cosmic variance only), for a hypothetical experiment that has perfect angular resolution and no instrumental noise. These numbers are for hypothetical full-sky experiments, but a realistic experiment will likely only be able to use $\sim 65\%$ of the sky for cosmology. If so, then each estimate for $\sigma_{g_{2M}}$ must be increased by a factor $(0.65)^{-1/2}$, about 25%. We also note that the theory cannot specify the direction $\hat{\mathbf{e}}$ of the quadrupole, and so a search for a quadrupole would require evaluation of all five g_{2M}s. A "3σ" detection would thus require that the sum of the squares of the g_{2M}s need to exceed $(3\sigma_{g_{2M}})^2$, which is independent of M.

The order of magnitude that we would expect for $\sigma_{g_{2M}}$ is $\sim N^{-1/2}_{\rm pix}$, where $N_{\rm pix} \sim l^2_{\rm max}$ is the number of resolution elements on the sky, comparable to the precision with which one can measure the variance (the monopole) of the temperature-fluctuation amplitude. The numerical results listed

[3] Note that our g_{20} is $(2/3)\sqrt{4\pi/5} g_*$, where g_* is the coefficient in Ref. [24] of $(\hat{\mathbf{k}} \cdot \hat{\mathbf{z}})^2$ if the preferred direction is taken to be $\hat{\mathbf{z}}$.

Table 3.1: The standard error $\sigma_{g_{2M}}$ to the amplitude of a quadrupole anisotropy in the matter power spectrum for different experiments. The instrumental temperature and polarization noises and beam width are listed for each experiment. We show results for the power multipole moments (pmm)for TT only, EE only, and the full result. We also show in the last three columns $\sigma^{\rm mv}_{g_{2M}}$ from the minimum-variance estimator for each experiment, for TT only, EE only, and the full result.

Experiment	σ_T (μK)	σ_P (μK)	$\theta_{\rm fwhm}$	$\sigma^{\rm pmm}_{g_{2M}}$ (TT)	$\sigma^{\rm pmm}_{g_{2M}}$ (EE)	$\sigma^{\rm pmm}_{g_{2M}}$ (total)
WMAP	30.0	42.6	$21'$	1.3	11	1.2
Planck	13.1	26.8	$5'$	1.6	0.16	0.16
EPIC	0.021	0.068	$52'$	1.2	0.55	0.42
Cosmic variance	0	0	0	1.8	0.014	0.014

Experiment	$\sigma^{\rm mv}_{g_{2M}}$ (TT)	$\sigma^{\rm mv}_{g_{2M}}$ (EE)	$\sigma^{\rm mv}_{g_{2M}}$ (total)
WMAP	0.024	2.4	0.024
Planck	0.0052	0.033	0.0050
EPIC	0.016	0.019	0.011

in Table 1 for the error to g_{2M} obtained from the power quadrupole moment $\widehat{b}_{2M}$ are not quite as good as this $N_{\rm pix}^{-1/2}$ expectation. The origin of this discrepancy can be traced to two sources. First of all, the two-dimensional CMB signal is degraded from the three-dimensional power spectrum; a Fourier mode in the $\hat{\mathbf{z}}$ direction gives rise to some temperature fluctuation near the north pole, and not just at the equator. This is manifest in the large coefficients (e.g., the factor of 512π) in our analytic estimates.

However, another reason that the estimator $\widehat{b}_{2M}$ does not provide a sensitive probe of a quadrupole departure from statistical isotropy is that it is not an optimal estimator for g_{2M}. This estimator sums the "signals" $D^{LM}_{ll'}$, but it does not weight these signals properly. This can be seen by noting that for a $C_l \propto l^{-2}$ power spectrum, for example, the error obtained from Eq. (3.18) can be reduced by applying a low-pass filter: i.e., by increasing the minimum values of ll' in the sums. (A simple calculation shows that with the properly chosen lower-l limit, $\sigma_{g_{2M}}$ can be reduced by a factor of 30.) If the precision of the result is improved by removing data, then something is sub-optimal.

3.5 The Minimum-Variance Estimator

3.5.1 The estimator and its variance

The $\widehat{b}_{LM}$ estimator is a simple and intuitive quantity that can be measured to test for statistical isotropy in a model-independent way. However, if one has a specific theory, defined by the functions $g_{LM}(k)$ or some quantities that parametrize the $g_{LM}(k)$, then there will be estimators that can be constructed to measure optimally those parameters. For example, if the g_{LM}s are all constants, then one can measure them better than the numerical results for the power multipole moments b_{LM}

would suggest. Below, we will derive the minimum-variance estimator for g_{LM}.

Before moving on, it is instructive and will be useful below to re-derive the variance to $\widehat{b}_{LM}^{\rm map}$. We return to Eq. (3.14) and note that $b_{LM}^{\rm map}$ can be written as a sum over $D_{ll'}^{LM,{\rm map}} \equiv D_{ll'}^{LM} W_l W_{l'}$. We then return to Eq. (3.6) to derive the minimum-variance estimator for $D_{ll'}^{LM,{\rm map}}$. Given a map $a_{lm}^{\rm map}$, each mm' pair provides an estimator for $D_{ll'}^{LM,{\rm map}}$, through

$$\widehat{D}_{ll',mm'}^{LM,{\rm map}} = \frac{a_{lm}^{\rm map} a_{l'm'}^{{\rm map},*} - C_l \delta_{ll'} \delta_{mm'}}{\xi_{lml'm'}^{LM}}, \tag{3.19}$$

with variance

$$\left\langle \left(\widehat{D}_{ll',mm'}^{LM,{\rm map}} \right)^2 \right\rangle = \frac{(1+\delta_{ll'}\delta_{mm'}) C_l^{\rm map} C_{l'}^{\rm map}}{\left(\xi_{lml'm'}^{LM}\right)^2}. \tag{3.20}$$

The estimators for different mm' pairs are uncorrelated (if we use the real and imaginary parts of the a_{lm}s), so the estimators can be summed over all mm' pairs, inversely weighted by the variance, to obtain a minimum-variance estimator. If $l = l'$, we sum only over $m' \geq m$ to avoid double-counting pairs. However, the factor $(1 + \delta_{ll'}\delta_{mm'})$ then weights the $m = m'$ modes twice as much, if $l = l'$, and thus allows us to re-write the sum over all m and m'. The result for the estimator can thus be written, for both $l = l'$ and $l \neq l'$, as

$$\widehat{D}_{ll'}^{LM,{\rm map}} = \frac{\sum_{mm'} a_{lm}^{\rm map} a_{l'm'}^{{\rm map},*} \xi_{lml'm'}^{LM}}{G_{ll'}^{L}}. \tag{3.21}$$

We recognize these to be the bipolar-spherical-harmonic coefficients of Refs. [67], with a slightly different weight. The variance of this estimator is then

$$\left\langle \left(\widehat{D}_{ll'}^{LM,{\rm map}} \right)^2 \right\rangle = \frac{(1+\delta_{ll'}) C_l^{\rm map} C_{l'}^{\rm map}}{G_{ll'}^{L}}. \tag{3.22}$$

The variance, Eq. (3.18), with which each b_{lm} can be measured simply follows by summing the variances of each term in Eq. (3.14).

Now, to construct the minimum-variance estimator, we simply note that the statistically independent quantities predicted by the theory are the $D_{ll'}^{LM}$'s, the generalizations of the C_l's for a theory without statistical isotropy. We have constructed above estimators for these quantities, and we have their variances. For a theory with constant g_{LM}'s, each $D_{ll'}^{LM}$ provides an estimator through $\widehat{g}_{LM,ll'} \equiv \widehat{D}_{ll'}^{LM} / F_{ll'}$. We then sum these, inversely weighted by their variance to obtain the minimum-variance estimator,

$$\widehat{g}_{LM} = \frac{\sum_{l' \geq l} F_{ll'} W_l W_{l'} \widehat{D}_{ll'}^{LM,{\rm map}} \left\langle \left(\widehat{D}_{ll'}^{LM,{\rm map}} \right)^2 \right\rangle^{-1}}{\sum_{l' \geq l} (F_{ll'} W_l W_{l'})^2 \left\langle \left(\widehat{D}_{ll'}^{LM,{\rm map}} \right)^2 \right\rangle^{-1}}, \tag{3.23}$$

obtained from the entire map. The variance $\sigma^2_{g_{LM}}$ of this estimator is then obtained by summing the inverse variances of all the estimators. Again, the sums are over $l' \geq l$, but the factor $(1 + \delta_{ll'})$ in Eq. (3.22) allows us to write the sum over all ll',

$$\frac{1}{\sigma^2_{g_{LM}}} = \sum_{ll'} G^L_{ll'} \frac{(F_{ll'} W_l W_{l'})^2}{2 C_l^{\rm map} C_{l'}^{\rm map}}. \tag{3.24}$$

3.5.2 Illustration: The Power Quadrupole

To illustrate, we now evaluate this expression for $L = 2$. Again, in this case, the only ll' combinations that contribute are $l' = l$ and $l' = l \pm 2$. We assume $l, l' \gg 1$, approximate $F_{l,l+2} \simeq -0.5\, C_l$, as above, and evaluate $C^{LM}_{l0l'0}$ as in Sec. 3.4.3. We can then write,

$$\frac{1}{\sigma^2_{g_{2M}}} \simeq 0.035 \sum_l \frac{l C_l^2 (W_l)^4}{(C_l^{\rm map})^2}, \tag{3.25}$$

which we can further approximate as $0.017\, l^2_{\rm max}$, where $l_{\rm max}$ is the multipole moment at which $C_l^{\rm n} \simeq C_l (W_l)^2$. The end result is then $\sigma_{g_{2M}} \simeq 7.6/l_{\rm max}$, quite close to what we would have expected by simply counting the number $N_{\rm pix} \simeq l^2_{\rm max}$ of usable pixels. For the WMAP and Planck temperature maps, $l_{\rm max}$ is roughly 650 and 2000, respectively, implying $\sigma_{g_{2M}} \sim 1.2 \times 10^{-2}$ and 3.8×10^{-3}, respectively, implying very significant improvements in the sensitivity over the power multipole moments.

Table 3.1 lists the exact numerical results, obtained by evaluating Eq. (3.24) exactly, for both TT only and EE only. Again, Appendix A generalizes Eq. (3.24) for the full temperature-polarization map, including the TE cross-correlation, and numerical results for this case are also included. The table shows that by weighting the modes correctly, we get an improvement of a factor of ~ 2 for WMAP and Planck EE and more than an order-of-magnitude improvement for WMAP and Planck TT; this is in accord with our arguments that the signal-to-noise in the TT power multipole moments was particularly poorly chosen. Although EPIC will have vastly improved instrumental sensitivity, with its modest angular resolution, it is not particularly well suited to search for departures from statistical isotropy. Again, the minimum-variance numbers in the table must be increased by about 25% to account for partial-sky coverage. And again, since the preferred direction is not known *a priori*, the sum of the squares of the g_{2M}s must exceed $(3\sigma_{g_{2M}})^2$ to claim a "3σ" detection of a departure of statistical isotropy.

3.6 Concluding Remarks

We have considered CMB tests for the statistical isotropy of the primordial power spectrum. The power spectrum of Eq. (3.2) is the most general power spectrum if the assumption of statistical

isotropy is dropped. In the more general case, the CMB power spectrum C_l is generalized to a set of moments $D_{ll'}^{LM}$, which are closely analogous to the bipolar-spherical-harmonic coefficients of Ref. [67]. The power multipole moments b_{LM} provide simple and intuitive statistics that can be used to search in a model-independent way for departures from statistical isotropy. If, however, a particular model is introduced by specifying a particular parametrization of the functions $g_{LM}(k)$, then minimum-variance statistics can be introduced to improve the precision with which these parameters can be constrained. For example, we constructed explicitly the minimum-variance estimators for the coefficients g_{LM} for the case in which they are k-independent. We applied these results to a model in which there is a quadrupole in the primordial power spectrum, and the results are shown in Table 3.1. We see that the best probe of a primordial quadrupole moment will come from Planck TT, for which we anticipate $\sigma_{g_{2M}} = 0.0052$. Multiplying this by 1.25 to account for a 65% sky coverage, and then by the factor of 3 required for a "3σ" detection, we find that the smallest quadrupole amplitude that will be detectable by Planck will be around 2.0%.

To reduce clutter in the equations and to keep the main line of reasoning clear, we have derived equations in the main body of the chapter for the case where either the temperature or the polarization is used, but not both. Appendix A generalizes the analysis to allow the use of the full temperature-polarization information, including the TE cross-correlation.

What about other probes? Consider, for example, the Sloan Digital Sky Survey [39]. The volume and galaxy density of the main galaxy survey allows measurement, roughly speaking, of the amplitudes of $N_{\rm modes} \sim 10^5$ independent Fourier modes of the density field, in the linear regime, and these measurements are cosmic-variance limited. Measurement of the quadrupole of the power spectrum can then simply be done by comparing the amplitudes of Fourier modes in different directions. The standard error to the power multipole moments will thus be $\sigma_{g_{LM}} \sim \sqrt{2/N_{\rm modes}} \sim 10^{-2}$, comparable in order of magnitude to what can be achieved with the CMB. Of course, a realistic search will be hampered by the irregular volume of the survey, redshift-space distortions, and anisotropies (line-of-sight–versus–angular) inherent to the measurement technique. But then again, there will be degradations (foregrounds, sky cuts, etc.) to the idealized CMB measurements we have considered. Of course, if $g_{LM}(k)$ varies with k, then the constraints provided by the CMB and galaxy surveys will be complementary, to the extent that the wavenumbers k probed by the CMB and galaxy surveys differ. Looking forward, there is ultimately the possibility of accessing with 21 cm fluctuations approximately 10^{15} modes of the primordial density field [71], allowing values as small as $g_{LM} \sim 10^{-7}$ to be probed, but this is in the very far future.

Acknowledgements

We thank D. Babich, K. Gorski, M. Wise, and C. Pahud for useful comments on an earlier draft. MK acknowledges the hospitality of the Aspen Center for Physics, where part of this work

was completed. AP acknowledges the support of the NSF. This work was supported by DOE DE-FG03-92-ER40701, NASA NNG05GF69G, the Gordon and Betty Moore Foundation, and a NASA Einstein Probe mission study grant, “The Experimental Probe of Inflationary Cosmology”.

Chapter 4

Non-Detection of a Statistically Anisotropic Power Spectrum in Large-Scale Structure

4.1 Introduction

Statistical isotropy (SI) is one of the most standard predictions of structure-formation and inflationary models. In this hypothesis, the density fluctuations in the universe are a realization of a random field whose statistical properties (e.g., power spectra) are invariant under rotations. When probing density fluctuations using the cosmic microwave background (CMB) temperature, SI is generally assumed in the analysis. However, searches for violations of SI, or statistical anisotropy, are now being performed with increasing precision as the amount of CMB data has grown. These searches are revealing possible evidence for statistical anisotropy in the CMB [15, 16, 17, 18], including a possible detection of quadrupolar anisotropy [35, 36, 31]. In response, many have proposed inflationary and dark-energy theories with parameters that quantify departures from SI [19, 20, 21, 22, 23, 24, 25, 26, 27, 28, 75, 76, 77]. The detection of quadrupolar anisotropy in the CMB now appears to be contaminated by systematic effects (possibly beam asymmetry [38], although this is debated [36]); as such it is desirable to constrain quadrupolar anisotropy by other techniques.

One way to quantify statistical anisotropy is to allow the three-dimensional power spectrum of matter density fluctuations $P(\mathbf{k})$ to depend on the direction of $\mathbf{k}$. This is a full description for Gaussian but anisotropic initial perturbations. This approach was motivated by the inflationary model of Ref. [24], a model for which Pullen & Kamionkowski [78] constructed parameter estimators for CMB analysis. As usual, if $\delta(\mathbf{k})$ is the Fourier amplitude of the fractional matter density

[0]The material presented in this chapter was first published in *Non-detection of a statistically anisotropic power spectrum in large-scale structure*, Anthony R. Pullen and Christopher Hirata, JCAP **1005**, 027 (2010). Reproduced here with permission, copyright (2010) by the Institute of Physics and SISSA.

perturbation, an anisotropic power spectrum is defined via

$$\langle \delta(\mathbf{k})\delta^*(\mathbf{k}')\rangle = (2\pi)^3\delta_{\rm D}(\mathbf{k}-\mathbf{k}')P(\mathbf{k})\,, \tag{4.1}$$

where the angle brackets denote an average over all realizations of the random field, and $\delta_{\rm D}$ is a Dirac δ-function; note that we still preserve the assumption that different Fourier modes are uncorrelated (statistical *homogeneity*). A direction-dependent $P(\mathbf{k})$ can be decomposed via

$$P(\mathbf{k}) = \bar{P}(k)\left[1+\sum_{LM} g_{LM}(k)R_{LM}(\hat{\mathbf{k}})\right], \tag{4.2}$$

where $\bar{P}(k)$ is the isotropically averaged matter power spectrum, and $R_{LM}(\hat{\mathbf{k}})$ (with $L \geq 2$) are real spherical harmonics. Physically, g_{LM} gives the magnitude of statistical anisotropy on order L, with M giving the direction of that anisotropy. Also, $g_{LM} = 0$ for odd L because a real scalar density field always has $\delta(\mathbf{k}) = \delta^*(-\mathbf{k})$ and hence $P(\mathbf{k}) = P(-\mathbf{k})$.

We define the real spherical harmonics $R_{LM}(\mathbf{k})$ in terms of the complex spherical harmonics $Y_{LM}(\mathbf{k})$ by

$$R_{LM} = \begin{cases} \frac{1}{\sqrt{2}}(Y_{LM} + Y^*_{LM}) & \text{if } M > 0 \\ Y_{L0} & \text{if } M = 0 \\ \frac{(-1)^M}{\mathrm{i}\sqrt{2}}(Y^*_{LM} - Y_{LM}) & \text{if } M < 0\,; \end{cases} \tag{4.3}$$

these are easily seen to obey the usual orthonormality rules, but have the advantage of making the g_{LM} coefficients real. The expressions for $L = 2$ are given in Appendix B.

The purpose of this analysis is to measure or constrain the anisotropy using large-scale structure data. Given the recent debate over the detection of quadrupolar anomalies in WMAP, and the evidence that the signal is contaminated by systematic effects [36, 31], it is worth using other datasets as well to constrain models with anisotropic power. In this analysis we will assume for simplicity that g_{LM} is scale-invariant. This is both a simplifying assumption, but is also a good first approximation in at least some classes of modified inflationary models [24]. We will also focus only on the quadrupole anisotropy g_{2M}; this is the phenomenologically simplest type of anisotropy allowed, and also emerges from anisotropic inflation models in the limit of very weak anisotropy [24].

Galaxy surveys probe matter fluctuations because on large scales, the galaxy density is related to the matter density in accordance with a linear bias model:

$$\left\langle \delta_g(\mathbf{k})\delta_g^*(\mathbf{k}')\right\rangle = (2\pi)^3\delta_D(\mathbf{k}-\mathbf{k}')b_g^2P(\mathbf{k})\,, \tag{4.4}$$

where $\delta_g(\mathbf{k})$ is the Fourier amplitude of the fractional galaxy density perturbation, and b_g is the linear

galaxy bias. The galaxy survey probe has been used to estimate $P(\mathbf{k})$ by stacking the measured angular matter power spectra C_l in eight photometric redshift slices ranging from $z = 0.2$ to 0.6 [79]. By performing a similar analysis and including the anisotropy parameters g_{2M} in the power spectrum, we can use galaxy surveys to estimate quadrupole anisotropy while assuming fiducial values for the other cosmological parameters.

The plan of this chapter is as follows: In Section 4.2 we describe the SDSS data used and why we choose LRGs to trace the galaxy distribution. Section 4.3 calculates the angular correlations statistical anisotropy produces in galaxy surveys and constructs estimators of the g_{2M}s and other systematic power spectrum variations. We present estimates of these parameters in Section 4.4, and in Section 4.5 we present our conclusions. Wherever not explicitly mentioned, we assume a flat ΛCDM cosmology with $\Omega_M = 0.3$, $\Omega_b = 0.05$, $h = 0.7$, $n_s = 1.0$, and $\sigma_8 = 0.9$. Since ours is a search for anisotropy, small changes in the cosmology will result only in changes in the calibration of the g_{2M} estimator; they do not alter the null hypothesis.

4.2 Choice of Sample

There are several ways to use galaxy survey data to search for statistical anisotropy. In principle, one could use a 3-dimensional redshift survey and search for anisotropy in the power spectrum. This would however be very technically involved: redshift-space distortions make the line of sight direction special. With sufficient sky coverage one could break the distinction between redshift-space distortions and true statistical anisotropy. However, in this analysis we choose the technically simpler route of using photometric galaxy catalogues, which can be studied using estimators analogous to those for the CMB.

The photometric data we use come from the Sloan Digital Sky Survey (SDSS) [80]. The SDSS consists of a 2.5 m telescope [81] with a 5-filter (*ugriz*) imaging camera [82] and a spectrograph. Automated pipelines are responsible for the astrometric solution [83] and photometric calibration [84, 85, 86, 87]. Bright galaxies, luminous red galaxies (LRGs), and quasars are selected for follow-up spectroscopy [88, 89, 90, 91]. The data used here were acquired between August 1998 and October 2004 and are included in SDSS Data Release 5 [92].

We use a sample of photometrically classified luminous red galaxies. LRGs are the most luminous galaxies in the universe, making them appealing for probing maximal volume. They also tend to be old stellar systems with uniform spectral energy distributions and a strong discontinuity at 4000 Å, which enables precise photometric redshifts and hence measurements of $\{g_{2M}\}$ in multiple redshift slices. This both reduces statistical error bars and allows tests for consistency. The cuts that define the photometric LRG sample are enumerated in Ref. [93]. The sample is divided into 8 photometric redshift slices of thickness $\Delta z_{\rm p} = 0.05$ ranging from $z_{\rm p,min} = 0.2$ to $z_{\rm p,max} = 0.6$, using the "single-

Table 4.1: Properties of the 8 LRG redshift slices; $z_{\rm p}$ is the photometric redshift range, and $z_{\rm mean}$ is the mean (true) redshift of the slice. N_{gal} is the number of galaxies in the redshift slice, and b_g is the linear bias.

Label	$z_{\rm p}$	$z_{\rm mean}$	N_{gal}	b_g
z00	0.20-0.25	0.233	30812	1.74
z01	0.25-0.30	0.276	38168	1.52
z02	0.30-0.35	0.326	37963	1.67
z03	0.35-0.40	0.376	55951	1.94
z04	0.40-0.45	0.445	77798	1.75
z05	0.45-0.50	0.506	138901	1.73
z06	0.50-0.55	0.552	126318	1.80
z07	0.55-0.60	0.602	93973	1.85

template" photo-z algorithm of Ref. [93]. We plot the redshift distributions in Fig. 4.1, while their properties are given in Table 4.1.

Our galaxy catalogue is a subset of that used by Ref. [94], but we restrict our attention to Galactic latitudes $b > 45°$. This was done in Ref. [79] to prevent stellar contamination in the data, and we decided to use the same cut accordingly. We pixelize these galaxies as a number overdensity, $\delta_g = (n - \overline{n})/\overline{n}$, onto a HEALPix pixelization [95] of the sphere, with $1,418,213$ pixels. This corresponds to a solid angle of 4662 deg^2 (as opposed to 3528 used in Ref. [79]). The LRG maps thus generated are shown in Fig. 4.2.

4.3 Formalism and Estimators

4.3.1 Galaxy density projections on the sky

We relate angular correlations in the sky to the direction-dependent matter power spectrum $P(\mathbf{k})$, which follows the derivation in Ref. [79] for the statistically isotropic case. A photometric galaxy survey measures the 2-dimensional projected galaxy overdensity $\delta_g(\hat{\mathbf{n}})$, which is related to the full 3-dimensional density via

$$\delta_g(\hat{\mathbf{n}}) = \int \mathrm{d}\chi f(\chi)\delta_g(\mathbf{x} = \chi\hat{\mathbf{n}})\,, \tag{4.5}$$

where χ is the comoving distance, and $f(\chi)$ is the radial selection function, which is the normalized redshift distribution for the redshift slice. (We leave out redshift space distortions here, but include them below.) By Fourier transforming $\delta_g(\mathbf{x})$ and using the identity

$$\mathrm{e}^{-\mathrm{i}\mathbf{k}\cdot\hat{\mathbf{n}}\chi} = \sum_{l=0}^{\infty}(2l+1)\mathrm{i}^l j_l(k\chi)P_l(\hat{\mathbf{k}}\cdot\hat{\mathbf{n}})\,, \tag{4.6}$$

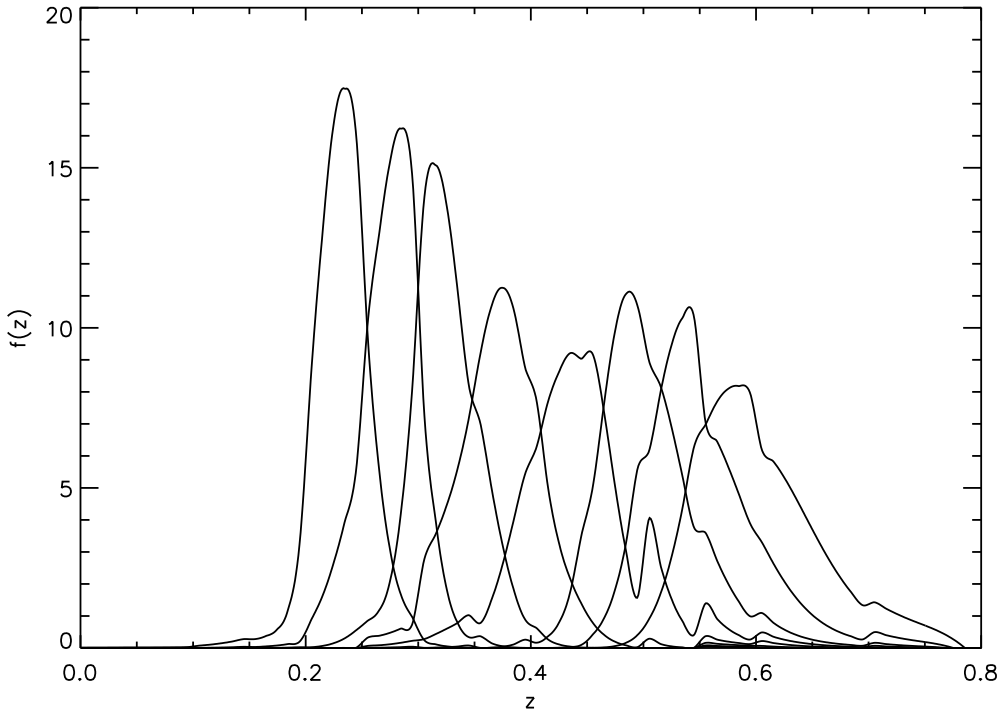

Figure 4.1: The redshift distributions for the 8 photometric LRG redshift slices.

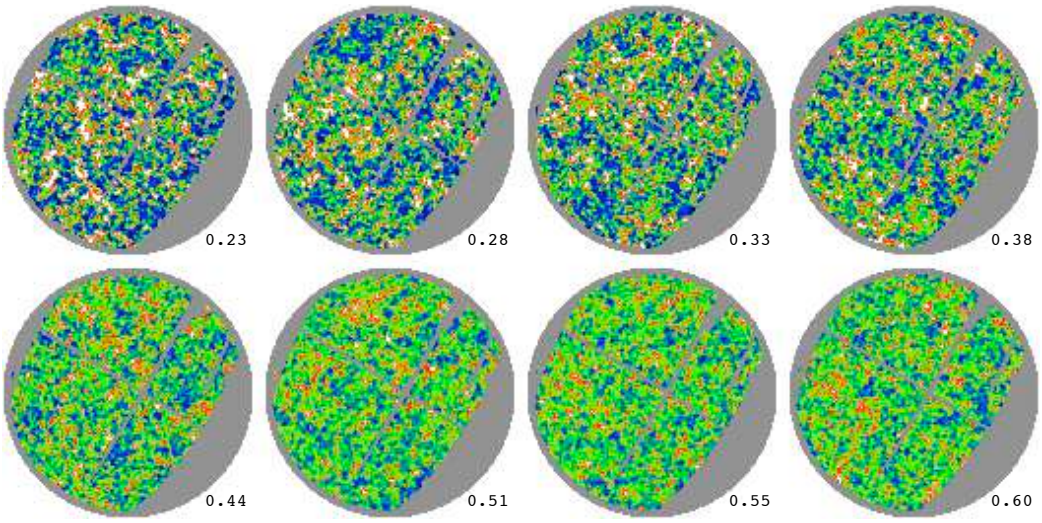

Figure 4.2: The LRG density in the 8 photometric redshift slices. The 45° radius caps are displayed in a Lambert azimuthal equal-area projection, with the north Galactic pole at the centre, $l = 0°$ at right, and $l = 90°$ at bottom. The labels indicate the characteristic redshift of each slice.

we obtain

$$\delta_g(\hat{\mathbf{n}}) = \sum_{l=0}^{\infty} \mathrm{i}^l (2l+1) \int \frac{\mathrm{d}^3 k}{(2\pi)^3} P_l(\hat{\mathbf{k}} \cdot \hat{\mathbf{n}}) \delta_g(\mathbf{k}) W_l(k) \,, \tag{4.7}$$

where

$$W_l(k) = \int \mathrm{d}\chi f(\chi) j_l(k\chi) \tag{4.8}$$

is the window function, and $j_l(x)$ and $P_l(x)$ are the l^{th}-order spherical bessel functions and Legendre polynomials, respectively.

The statistical properties of the 2-dimensional galaxy field can be derived in analogy to those for the CMB [78], with $W_l(k)$ replacing the CMB radiation transfer function $\Theta_l(k)$.[1] If statistical isotropy is valid, then the two-point galaxy correlation function can be written as

$$C_g(\hat{\mathbf{n}}, \hat{\mathbf{n}}')|_{\mathrm{SI}} = \langle \delta_g(\hat{\mathbf{n}}) \delta_g(\hat{\mathbf{n}}') \rangle \,|_{\mathrm{SI}} = \sum_l \frac{2l+1}{4\pi} C_{g,l} P_l(\hat{\mathbf{n}} \cdot \hat{\mathbf{n}}') \,, \tag{4.9}$$

where $C_{g,l}$ is the angular galaxy power spectrum:

$$C_{g,l} = \frac{2}{\pi} \int_0^{\infty} \mathrm{d}k \, k^2 \bar{P}_g(k) [W_l(k)]^2 \,, \tag{4.10}$$

where $\bar{P}_g(k) = b_g^2 \bar{P}(k)$. However, the presence of statistical anisotropy will cause additional terms to appear other than the ones in Eq. 4.9. Using Eqs. (4.7) and (4.2), we find for the statistically anisotropic case

$$\begin{aligned} C_g(\hat{\mathbf{n}}, \hat{\mathbf{n}}') &= \sum_l \frac{2l+1}{4\pi} C_{g,l} P_l(\hat{\mathbf{n}} \cdot \hat{\mathbf{n}}') \\ &\quad + \sum_{LM} \sum_{lml'm'} D^{LM}_{g,ll'} X^{LM}_{lml'm'} R_{lm}(\hat{\mathbf{n}}) R_{l'm'}(\hat{\mathbf{n}}') \,. \end{aligned} \tag{4.11}$$

Here, the set of $C_{g,l}$s are given by the usual galaxy power spectrum for the case of statistical isotropy. Statistical anisotropy produces the second term, where

$$D^{LM}_{g,ll'} = \mathrm{i}^{l-l'} \frac{2}{\pi} \int_0^{\infty} \mathrm{d}k \, k^2 \bar{P}_g(k) g_{LM} W_l(k) W_{l'}(k) \,, \tag{4.12}$$

and

$$X^{LM}_{lml'm'} = \int d^2\hat{\mathbf{k}} \, R_{lm}(\hat{\mathbf{k}}) R_{l'm'}(\hat{\mathbf{k}}) R_{LM}(\hat{\mathbf{k}}) \tag{4.13}$$

[1] Note that with our definition of the Fourier transform, there is a relative factor of $(2\pi)^3$ between some of our formulas and those of Ref. [78].

is the real 3-harmonic coupling coefficient. Its expression in terms of Wigner 3-j symbols is given in C. Parity implies that $X^{LM}_{lml'm'}$ is nonzero only for $l+l'-L$ even. Since earlier in the Introduction we showed L is even, this requires $l+l'$ to be even and $D^{LM}_{g,ll'}$ to be real. Eqs. 4.10 and 4.12 agree with similar results in Ref. [78], and $X^{LM}_{lml'm'}$ in Eq. 4.13 is analogous to $\xi^{LM}_{lml'm'}$ in Ref. [78]. Throughout this chapter, we use upper-case indices LM for statistical anisotropies in the matter power spectrum, and lower-case indices lm for random anisotropies in the galaxy distribution.

In Fig. 4.3 we show the predicted angular galaxy power spectra $C_{g,l}$ for the eight redshift slices in our analysis assuming our fiducial cosmology. We use CMBFAST [69] to calculate $\bar{P}(k)$, and we use the HALOFIT prescription [96] to evolve $\bar{P}(k)$ into the nonlinear regime. Note that we do not attempt to account for the nonlinear evolution of g_{LM}, which only suppresses the primordial anisotropy by $\lesssim 7\%$ on quasilinear scales [97]. We also display $[-F_{g,l(l+2)}]$, where $F_{g,ll'} = D^{LM}_{g,ll'}/g_{LM}$. We only need to show $F_{g,l(l+2)}$ because we are interested only in quadrupolar statistical anisotropy, or $L=2$. For this case it can be shown that $X^{2M}_{lml'm'}$ is zero except for the cases $l'=l$ and $l'=l\pm 2$, and $F_{g,ll} = C_{g,l}$.[2] Notice that for large l and smooth $f(\chi)$, $W_l(k) \to \sqrt{\pi/l}\, f(l/k)/(2k)$; then we have $W_{l+2} \simeq W_l$ and $F_{g,l(l+2)} \simeq -C_{g,l}$.

We also show in Fig. 4.3 $C_{g,l}$ and $[-F_{g,l(l+2)}]$ when the effect of redshift space distortions is included. We include this effect by substituting for the window function $W_l = W^0_l + W^r_l$, where W^0_l is the window function shown in Eq. 4.8 and W^r_l is given by

$$\begin{aligned} W^r_l(k) &= \beta\Bigg[\frac{2l^2+2l-1}{(2l+3)(2l-1)}W^0_l(k) \\ &\quad - \frac{l(l-1)}{(2l-1)(2l+1)}W^0_{l-2}(k) \\ &\quad - \frac{(l+1)(l+2)}{(2l+1)(2l+3)}W^0_{l+2}(k)\Bigg], \end{aligned} \tag{4.14}$$

and β is the redshift distortion parameter given approximately by $\beta \sim \Omega_m^{0.6}/b_g$. The formulas for redshift space distortions in the angular galaxy power spectrum were derived in Ref. [79].

4.3.2 Estimation of power and statistical anisotropy

We construct a quadratic estimator [98, 99] to measure the anisotropy coefficients g_{2M}. As always when searching for anisotropies, it is necessary to fit simultaneously for the galaxy power spectrum, the anisotropy, and any systematics terms that may be present in the data. The basic premise is to write the galaxy density fluctuation map as a vector $\delta_{\mathbf{g}}$ of length $N_{\rm pix}$. This vector has an $N_{\rm pix}\times N_{\rm pix}$

[2] For nonzero $X^{2M}_{lml'm'}$, the triangle inequality requires $|l-l'| \le L = 2$, and parity requires $l-l'$ to be even.

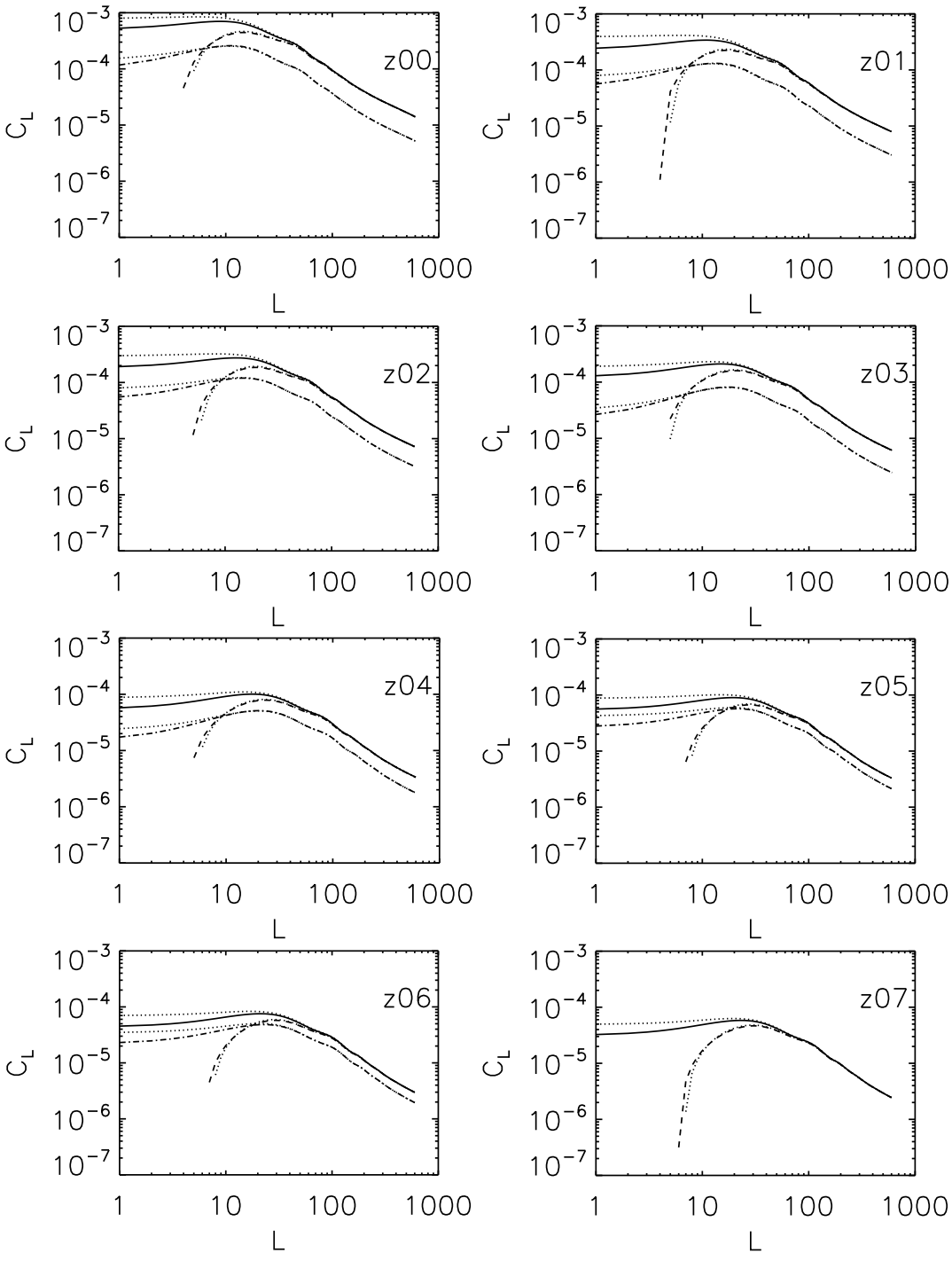

Figure 4.3: The predicted angular power spectra for each of the 8 LRG redshift slices. The solid lines show nonlinear auto power spectra, while the dash-dotted lines show the cross-power power spectra with the adjacent slice at higher redshift. The dashed lines show the predicted $[-F_{g,l(l+2)}]$. The dotted lines show the effect of redshift space distortions on all three spectra.

covariance matrix $\mathbf{C}$, which we parameterize as

$$\mathbf{C} = \sum_{i=1}^{N_t} p_i \mathbf{C}_{,i}, \tag{4.15}$$

where the $\{p_i\}_{i=1}^{N_t}$ are parameters to be estimated and $\{\mathbf{C}_{,i}\}_{i=1}^{N_t}$ are "templates". The notation also serves to remind us that $\mathbf{C}_{,i} = \partial\mathbf{C}/\partial p_i$. In the case of a Gaussian random field, the minimum-variance unbiased quadratic estimators for the $\{p_i\}$ are

$$\hat{\mathbf{p}} = \mathbf{F}^{-1}\mathbf{q}\,, \tag{4.16}$$

where

$$F_{ij} = \frac{1}{2}\mathrm{tr}\left[\mathbf{C}_{,\mathrm{i}}\,\mathbf{w}\mathbf{C}_{,\mathrm{j}}\,\mathbf{w}\right] \tag{4.17}$$

is the Fisher matrix and

$$q_i = \frac{1}{2}\delta_{\mathbf{g}}^{\mathbf{T}}\mathbf{w}\mathbf{C}_{,i}\,\mathbf{w}\delta_{\mathbf{g}}\,. \tag{4.18}$$

Here $\mathbf{w}$ is a weighting matrix, which should be taken equal to the inverse of the covariance matrix $\mathbf{C}$. Fortunately, the estimator $\hat{\mathbf{p}}$ remains unbiased (but not necessarily minimum-variance) for any choice of weight $\mathbf{w}$, and regardless of whether the true galaxy field δ_g is Gaussian or not. For our analysis, we take the weight to be $\mathbf{w} = (\mathbf{S}+\mathbf{N})^{-1}$, where $\mathbf{S}$ is the signal covariance matrix (diagonal in lm-space, and using the theoretical power spectra) and $\mathbf{N}$ is the Poisson noise. The matrix inversion and trace estimation are done by the iterative and stochastic methods described in detail in Refs. [100, 79].

We next turn our attention to the template construction. The simplest template is the Poisson noise itself,

$$C_{ij,N} = \frac{\delta_{ij}}{\overline{n}}\,, \tag{4.19}$$

where $\overline{n}$ is the mean number of galaxies per pixel, and N is the noise amplitude (1 for pure Poisson noise). We may also parameterize the isotropic part of the power spectrum by band power amplitudes $\tilde{C}_n$ with $C_{g,l} = \sum_{n=1}^{N_{\mathrm{bin}}} \tilde{C}_n \eta_l^n$, where η_l^n is a step function that is 1 when l is in bin n and 0 otherwise. The corresponding template is

$$\frac{\partial C_{ij}}{\partial \tilde{C}_n} = \sum_{lm} R_{lm}(\hat{\mathbf{n}}_i) R_{lm}(\hat{\mathbf{n}}_j)\eta_l^n. \tag{4.20}$$

We use 18 bins in l, ranging from $l = 2$ up through 600.

For the anisotropy parameters g_{2M}, the templates are somewhat more complicated. We first extract g_{2M} from the anisotropy amplitude $D^{2M}_{g,ll'}$:

$$D^{2M}_{g,ll'} = g_{2M} F_{g,ll'} \,, \tag{4.21}$$

where

$$F_{g,ll'} = \mathrm{i}^{l-l'} \frac{2}{\pi} \int_0^\infty \mathrm{d}k \, k^2 \bar{P}_g(k) W_l(k) W_{l'}(k) \,. \tag{4.22}$$

Inspection of Eq. 4.11 then leads us to:

$$\begin{aligned} \frac{\partial C_{ij}}{\partial g_{2M}} &= \sum_{lmm'} \Big[C_{g,l} X^{2M}_{lmlm'} R_{lm}(\hat{\mathbf{n}}_i) R_{lm'}(\hat{\mathbf{n}}_j) \\ &\quad + F_{g,l(l+2)} X^{2M}_{lm(l+2)m'} R_{lm}(\hat{\mathbf{n}}_i) R_{(l+2)m'}(\hat{\mathbf{n}}_j) \\ &\quad + F_{g,l(l-2)} X^{2M}_{lm(l-2)m'} R_{lm}(\hat{\mathbf{n}}_i) R_{(l-2)m'}(\hat{\mathbf{n}}_j) \Big] \,. \end{aligned} \tag{4.23}$$

In addition to these "essential" templates, we have also added two others to project out various systematics that could mimic statistical anisotropy. In particular, if there are photometric calibration errors that vary slowly across the survey (either colored or gray)[3], then the depth or effective redshift may vary, which would lead to a modulation of both the signal power spectrum and the noise level across the sky.

We model the modulation of the signal power spectrum by considering a modulation in the fractional density perturbation field in the form $\delta'(\hat{\mathbf{n}}) = [1 + h(\hat{\mathbf{n}})]\delta(\hat{\mathbf{n}})$. This modulation will cause the two-point galaxy correlation function to have an extra factor of $[1 + h(\hat{\mathbf{n}})][1 + h(\hat{\mathbf{n}}')] \simeq 1 + h(\hat{\mathbf{n}}) + h(\hat{\mathbf{n}}')$, assuming $h(\hat{\mathbf{n}}) \ll 1$. We choose to allow $h(\hat{\mathbf{n}})$ to have a quadrupole pattern. (Other forms of slow modulation across the sky, e.g., a dipole, should be degenerate with a quadrupole given that our data is only in a cap of radius 45°.)

In this case $\delta'(\hat{\mathbf{n}})$ can be written as

$$\delta'(\hat{\mathbf{n}}) = \left[1 + \sum_{M=-2}^{2} h_{2M} R_{2M}(\hat{\mathbf{n}}) \right] \delta(\hat{\mathbf{n}}) \,, \tag{4.24}$$

where h_{2M} are the modulation parameters. In the case of modulation with no statistical anisotropy,

[3]Colored errors apply to an error in the relative calibration of different bands, e.g., $g - r$, whereas gray errors leave colors fixed but vary the magnitude of an object.

$C_g(\hat{\mathbf{n}}, \hat{\mathbf{n}}')$ is given by

$$C_g(\hat{\mathbf{n}}, \hat{\mathbf{n}}') = \left\{ 1 + \sum_{M=-2}^{2} h_{2M} \left[R_{2M}(\hat{\mathbf{n}}) + R_{2M}(\hat{\mathbf{n}}') \right] \right\} C_g(\hat{\mathbf{n}}, \hat{\mathbf{n}}')|_{SI} \,, \tag{4.25}$$

where $C_g(\hat{\mathbf{n}}, \hat{\mathbf{n}}')|_{SI}$ is given by Eq. 4.9. By using the identity

$$R_{lm}(\hat{\mathbf{n}}) R_{l'm'}(\hat{\mathbf{n}}) = \sum_{LM} X^{LM}_{lml'm'} R_{LM}(\hat{\mathbf{n}}) \,, \tag{4.26}$$

we find

$$\begin{aligned} C_g(\hat{\mathbf{n}}, \hat{\mathbf{n}}') &= C_g(\hat{\mathbf{n}}, \hat{\mathbf{n}}')|_{\rm SI} \\ &\quad + \sum_{lml'm'M} h_{2M} \left(C_{g,l} + C_{g,l'} \right) X^{2M}_{lml'm'} R_{lm}(\hat{\mathbf{n}}) R_{l'm'}(\hat{\mathbf{n}}'), \end{aligned} \tag{4.27}$$

hence

$$\begin{aligned} \frac{\partial C_{ij}}{\partial h_{2M}} &= \sum_{lmm'} \Bigg[2 C_{g,l} X^{2M}_{lmlm'} R_{lm}(\hat{\mathbf{n}}_i) R_{lm'}(\hat{\mathbf{n}}_j) \\ &\quad + (C_{g,l} + C_{g,l+2}) X^{2M}_{lm(l+2)m'} R_{lm}(\hat{\mathbf{n}}_i) R_{(l+2)m'}(\hat{\mathbf{n}}_j) \\ &\quad + (C_{g,l} + C_{g,l-2}) X^{2M}_{lm(l-2)m'} R_{lm}(\hat{\mathbf{n}}_i) R_{(l-2)m'}(\hat{\mathbf{n}}_j) \Bigg]. \end{aligned} \tag{4.28}$$

An analogous construction for modulation of the Poisson noise gives

$$\frac{\partial C_{ij}}{\partial f_{2M}} = \frac{\delta_{ij}}{\overline{n}} R_{2M}(\hat{\mathbf{n}}_i) \,. \tag{4.29}$$

These 10 parameters (h_{2M} and f_{2M}) are jointly estimated with $\{\tilde{C}_n, g_{2M}\}$.

4.3.3 Gaussian simulations

We test our estimator on a suite of simple simulations in order to verify its ability to detect anisotropy when it is present (and to measure zero when anisotropy is not present). Gaussian simulations are sufficient for this purpose since a quadratic estimator by construction cannot be sensitive to higher moments of the data.

We perform two tests, one without anisotropy or modulation and one with both. In each test, we use the power spectrum $C_{g,l}$ and $F_{g,l(l+2)}$ of redshift slice z00 for our fiducial cosmology to construct 50 sets of simulated galaxy perturbation maps over the pixels in our analysis' viewing region. We also add Gaussian noise to each pixel, with the variance in the noise set equal to $1/\overline{n}_{\rm gal}$, where $\overline{n}_{\rm gal}$ is the average number of galaxies per pixel for the redshift slice (consistent with Poisson fluctuations).

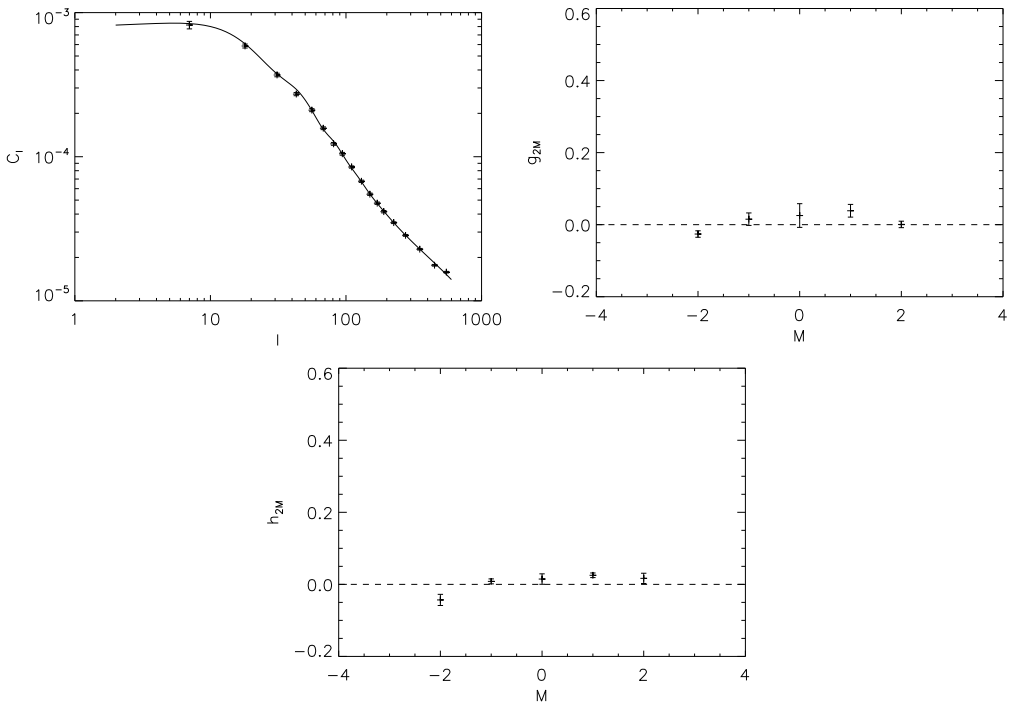

Figure 4.4: The parameter values for the simulation test with no input anisotropy or modulation, including 1-sigma errors. The top-left panel shows the $\tilde{C}_n$, the top-right panel shows the g_{2M}s, and the bottom panel shows the h_{2M}s.

Then, we run each simulation through the algorithm to find an estimated set of parameters $\tilde{C}_n$, g_{2M}, and h_{2M}. We then average these parameters over all 50 simulations to find an output set of parameters, which we then compare to our input parameters for constructing the simulations. Since we do not input $\tilde{C}_n$ directly, we instead compare the output $\tilde{C}_n$ to $C_{g,l}$ at the median l of bin n. Note that the variance used to compare the input and output parameter sets is equal to the variance of one simulation, taken from the diagonal of the inverse-Fisher matrix, divided by the number of simulations.

For the first test, our simulations had input parameters $g_{2M} = h_{2M} = 0$ for all M. Since there is no covariance between the simulated $\delta_{g,lm}$, the real spherical harmonic coefficients of $\delta_g(\hat{\mathbf{n}})$, we can simulate each $\delta_{g,lm}$ independently. A plot of the input and output parameter values for $\tilde{C}_n$, g_{2M}, and h_{2M} are shown in Fig. 4.4. In the figures we see good agreement between the input and output values. This test shows us that our algorithm should not see anisotropy or modulation where there is none. We also see that the error for $g_{2,0}$ is larger than the errors for the other g_{2M}s. This is due to a lack of data in the equatorial plane while $g_{2,0}$ parametrizes a quadrupole along the z-direction. Our data set makes this type of quadrupole less distinguishable from a uniform excess over the whole sky than with other quadrupole types.

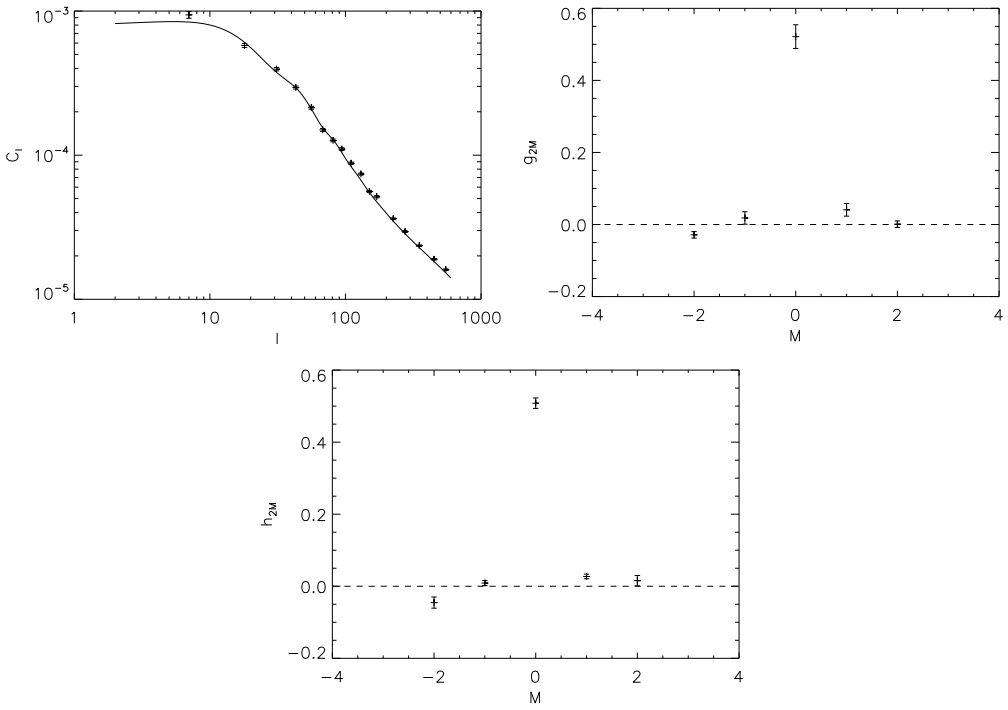

Figure 4.5: The parameter values for the simulation test with input anisotropy and modulation, including 1-sigma errors. The top-left panel shows the $\tilde{C}_n$, the top-right panel shows the g_{2M}s, and the bottom panel shows the h_{2M}s. Note that the input values for g_{20} and h_{20} are 0.5.

In the second test, we simulate anisotropic power and modulation in the z-direction by setting $g_{20} = h_{20} = 0.5$. Now that the $\delta_{g,lm}$s are correlated, their simulation is no longer trivial. To construct the simulation, we define the matrix $E^{(m)}_{ll'}$, equal to $\langle \delta_{g,lm} \delta_{g,l'm} \rangle$ in the case $g_{2M} = h_{2M} = 0$ for all M except $M = 0$. This matrix is given by

$$E^{(m)}_{ll'} = C_{g,l}\delta_{ll'} + g_{20} F_{g,ll'} X^{20}_{lml'm} + h_{20}(C_{g,l} + C_{g,l'}) X^{20}_{lml'm} \,. \tag{4.30}$$

To construct our simulation, we perform a Cholesky decomposition on $\mathbf{E^{(m)}}$ to find the triangular matrix $\mathbf{L^{(m)}}$ such that $\mathbf{E}^{(m)} = \mathbf{L}^{(m)}\mathbf{L}^{(m)\,T}$. We use $\mathbf{L^{(m)}}$ to construct $\delta^{\mathbf{(m)}}_{\mathbf{g}} = \mathbf{L^{(m)}x^{(m)}}$, where $\mathbf{x^{(m)}}$ is a Gaussian random matrix with zero mean and unit variance. This setup gives us the desired covariances we need in the $\delta_{g,lm}$s. A plot of the input and output parameter values for $\tilde{C}_n$, g_{2M}, and h_{2M} in this case are shown in Fig. 4.5. In the figures we see good agreement between the input and output values, including for g_{20} and h_{20}.

4.4 Results

We show our results for $C_{g,l}$ in Fig. 4.6. Because our galaxy sample covers only 11% of the sky, the powers in C_l and g_{2M} become degenerate, and the isotropic and anisotropic templates become highly correlated. Thus, when calculating C_l, we remove the anisotropic templates for g_{2M}, h_{2M}, and f_{2M} so that power in the C_ls is favored. When using this approach, we see agreement between the measured power spectra and the predicted spectra.

Our results for g_{2M} are shown in Fig. 4.7. For each multipole of g_{2M}, we see consistency with the null result among the redshift slices except for the measurement of g_{20} in redshift slice z03. At this redshift, we measure $g_{20} = 0.925 \pm 0.258$ (Fisher uncertainty) or ± 0.315 (uncertainty derived from N-body simulations, as described in Sec. 4.4.1). This formally corresponds to a 3.59σ (Fisher) or 2.94σ (simulation) detection significance; however all of the other redshift slices have g_{20} within 1σ of zero. This is puzzling and in principle could indicate either a statistical fluke or a systematic error that afflicts the z03 slice. We note that the statistical significance is marginal: given that we calculated $5 \times 8 = 40$ g_{2M}s, the probability of having at least one of them deviate by 2.94σ is 12% (assuming a Gaussian distribution). On the other hand, the z03 slice is also the redshift at which the LRG colour locus changes direction [79]. The z03 slice also has the highest bias, which would make it susceptible to nonlinear errors.

The results we found for the other multipoles were consistent for each redshift slice only when we allowed h_{2M} and f_{2M} to vary from the null result. We show the results for h_{2M} in Fig. 4.8 and f_{2M} in Fig. 4.9. Note that many of the h_{2M}s and f_{2M}s are inconsistent with zero, which hint at possible systematic errors of these forms.

4.4.1 Combined statistical anisotropy estimate

To find an estimate of g_{2M} combining all of the redshift slices, we construct a minimum-variance estimator of the form

$$\widehat{g}_{2M} = \frac{\sum_i g_{2M,i}/\sigma^2_{g_{2M,i}}}{\sum_i 1/\sigma^2_{g_{2M,i}}}\,, \tag{4.31}$$

where $g_{2M,i}$ is the estimate of g_{2M} in redshift slice i and $\sigma^2_{g_{2M,i}} = (F^{-1})_{MM}$ for redshift slice i. A crude estimate of the uncertainty in $\widehat{g}_{2M}$ is given by

$$\frac{1}{\sigma^2_{g_{2M}}} = \sum_i \frac{1}{\sigma^2_{g_{2M,i}}} \tag{4.32}$$

This uncertainty estimate neglects covariances between the redshift slices and non-Gaussian (trispectrum) corrections to the errors in individual slices. We therefore expect it to somewhat underestimate

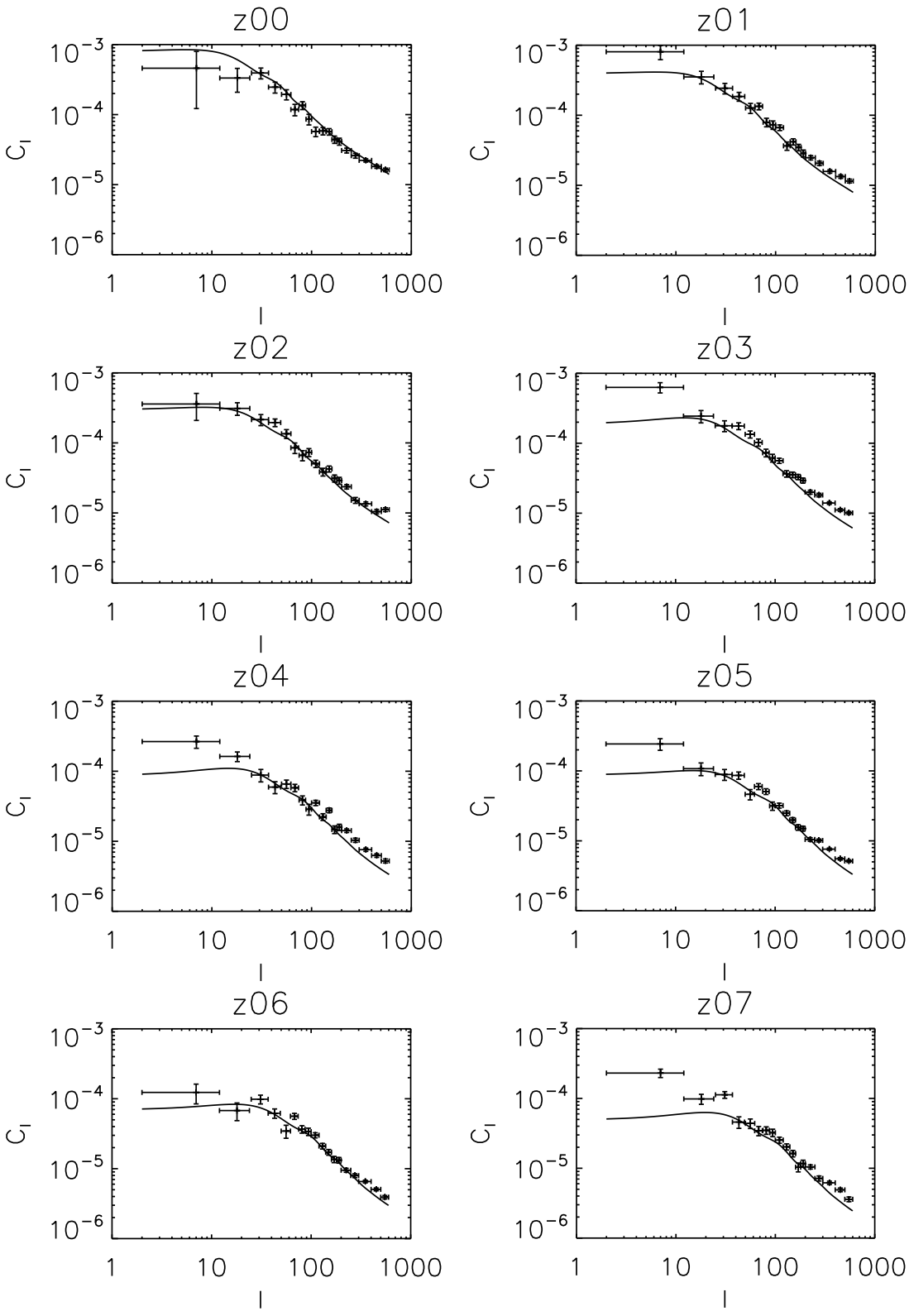

Figure 4.6: The measured angular power spectrum for the 8 LRG redshift slices. The solid lines are the predicted nonlinear power spectra for our fiducial cosmological model, and the crosses are the measured spectra.

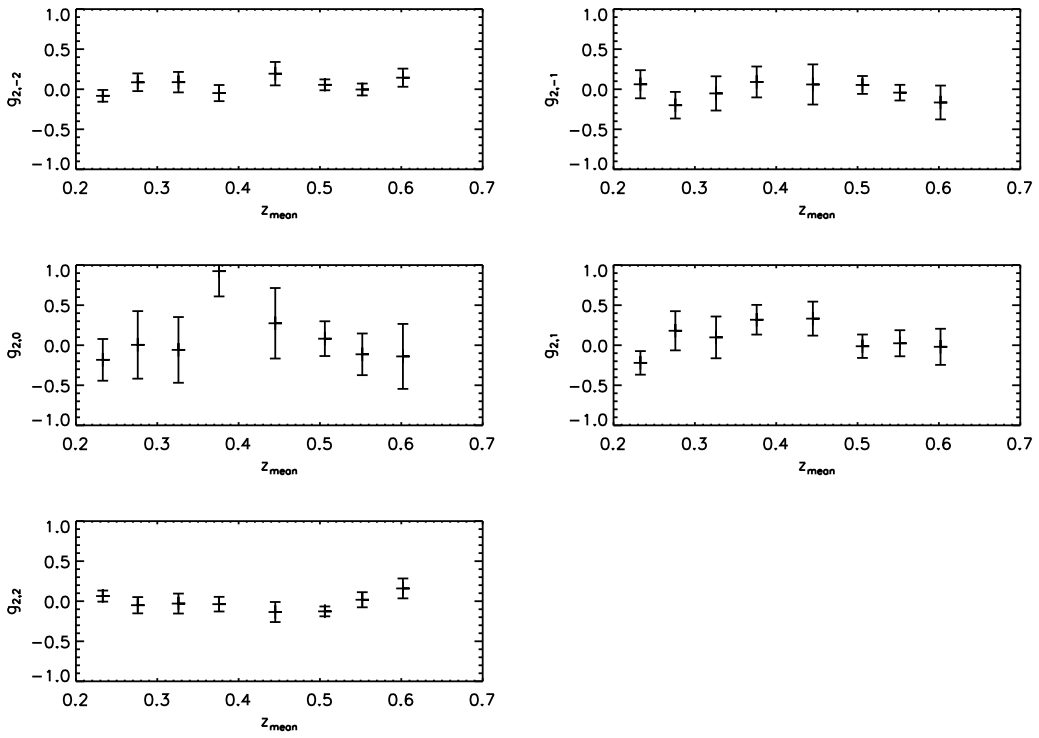

Figure 4.7: The quadrupole anisotropy parameters vs. redshift slice for each multipole with 1σ errors from the simulations. Note $g_{20} = 0.925$ for redshift slice z03, formally a 2.94σ detection.

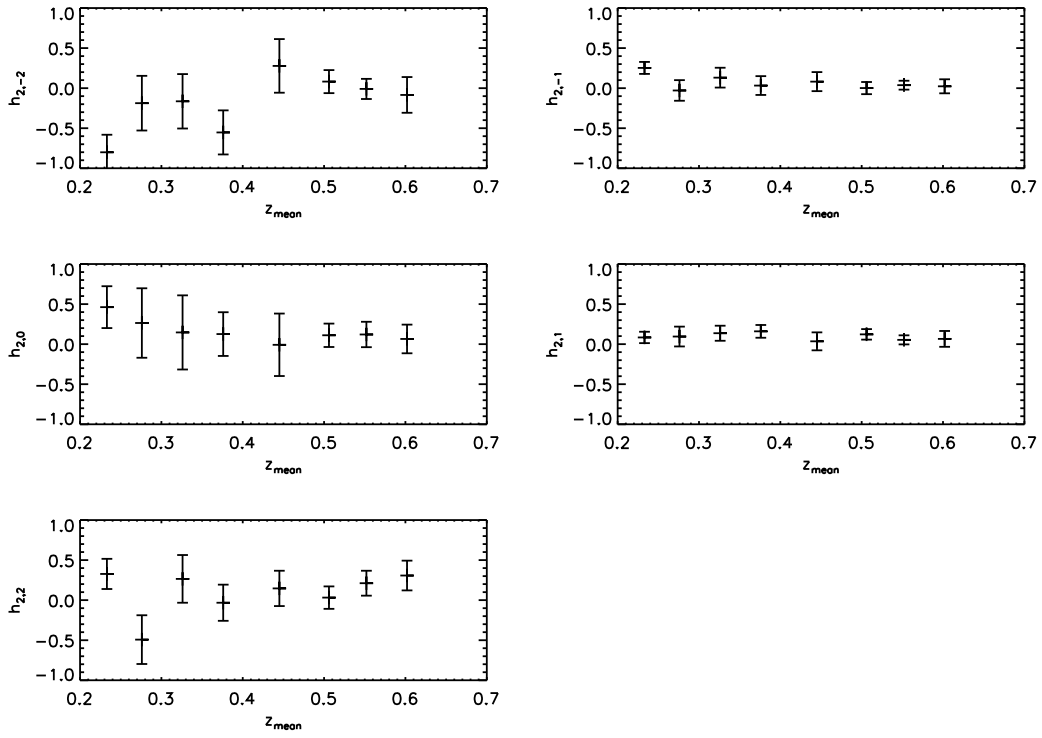

Figure 4.8: The quadrupole modulation parameters vs. redshift slice for each multipole with 1σ errors from the simulations.

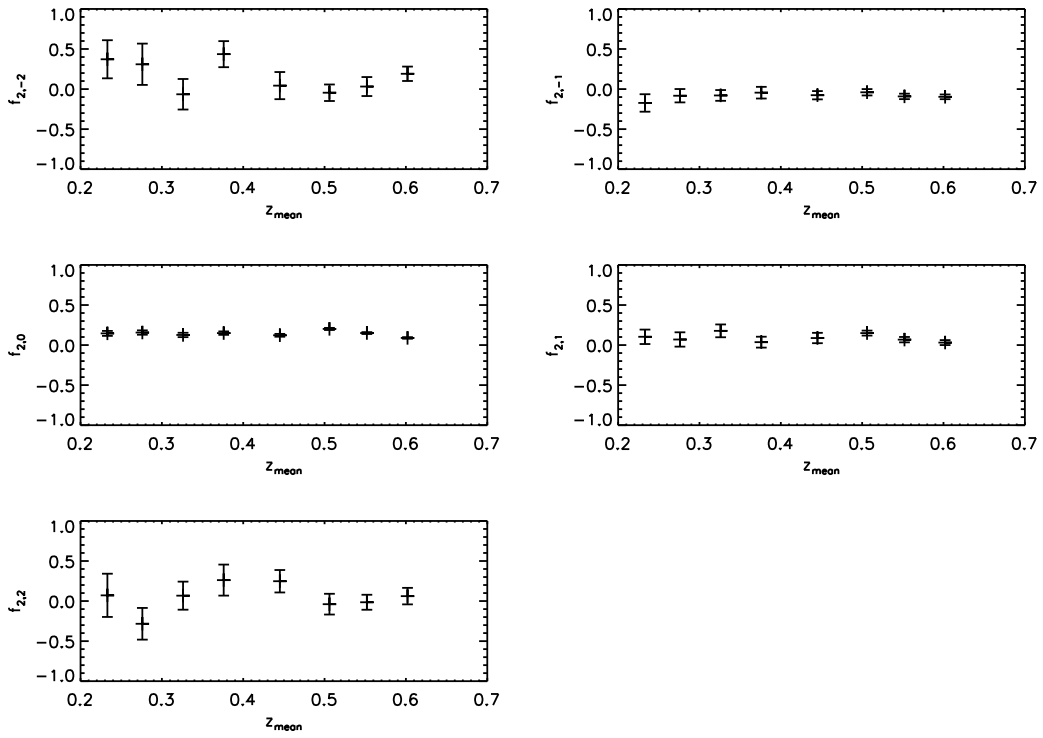

Figure 4.9: The Poisson noise modulation parameters vs. redshift slice for each multipole with 1σ errors from the simulations.

the true uncertainty in $\widehat{g}_{2M}$. For this reason we expect that error bars derived from N-body simulations (as described next) are more reliable. The $\widehat{g}_{2M}$ values and their uncertainties as calculated by Eq. 4.32 are shown in the top panel of Fig. 4.10.

We may alternatively estimate the covariance matrix $C_{MM'}$ of g_{2M} using N-body mock catalogues, which contain the correct slice-to-slice correlations and a more realistic description of the true non-Gaussian density field. We used a suite of 10 simulation boxes of size $(2h^{-1}\ \mathrm{Gpc})^3$ with periodic boundary conditions, described in more detail in Ref. [101]. For simplicity, and since our objective is to obtain a covariance matrix rather than a precision prediction of the power spectrum, we have used the halo catalogue from a single simulation output at $z = 0.3$. We populate each halo with a galaxy (or two galaxies if $M_{\rm halo} > M_2$) and use its "true" redshift (including the halo peculiar velocity) and the photo-z error distribution [93] to assign a photometric redshift. A catalogue of galaxies is then constructed by taking each halo down to some minimum mass $M_{{\rm min},i}$ fixed by the requirement to have the correct number of galaxies in the ith photo-z slice. The parameter M_2 controls the amplitude of the "1-halo" term in the power spectrum arising from multiple galaxies per halo (in the sense that the 1-halo term is set to zero if $M_2 = \infty$). We choose M_2 by first constructing a mock catalogue with $M_2 = \infty$. The excess power ΔC_l in the $300 \leq l < 600$ range is then determined for each photo-z slice. The 3D number density of doubly-occupied haloes n_d required to produce this excess power is then estimated as

$$n_d = \frac{\bar{n}^2}{2\, dV/d\Omega} \Delta C_l. \tag{4.33}$$

An average value of n_d is taken over all slices ($n_d = 1.8 \times 10^{-5} h^3\,\mathrm{Mpc}^{-3}$) and this is used to set a mass threshold ($M_2 = 7.8 \times 10^{13} h^{-1} M_\odot$).[4] This procedure generates an entire simulated photo-z survey, including all 8 slices and the correct correlations among different slices due to large scale structure.

We construct 40 realizations of the survey, using each of the 10 boxes 4 times with different observer locations. We then estimate g_{2M} for each simulation and redshift slice, which we marginalize using Eq. 4.31 to find an estimate of $\widehat{g}^{(\alpha)}_{2M}$ for each simulation α. We use these estimates to construct the covariance matrix of the form

$$C_{MM'} = \frac{1}{39} \sum_{\alpha=1}^{40} (\widehat{g}^{(\alpha)}_{2M} - \overline{g}_{2M})(\widehat{g}^{(\alpha)}_{2M'} - \overline{g}_{2M'})\,, \tag{4.34}$$

where $\overline{g}_{2M}$ is g_{2M} averaged over the simulations. The diagonal elements of $C_{MM'}$ give the uncertainties in g_{2M}. We plot $\widehat{g}_{2M}$ with these uncertainties in the bottom panel of Fig. 4.10. We see in this case all the measurements are within one sigma of the null result, which is consistent with

[4] In principle, this procedure could be iterated with computation of a new ΔC_l, etc., however the method is probably too crude to justify such a procedure.

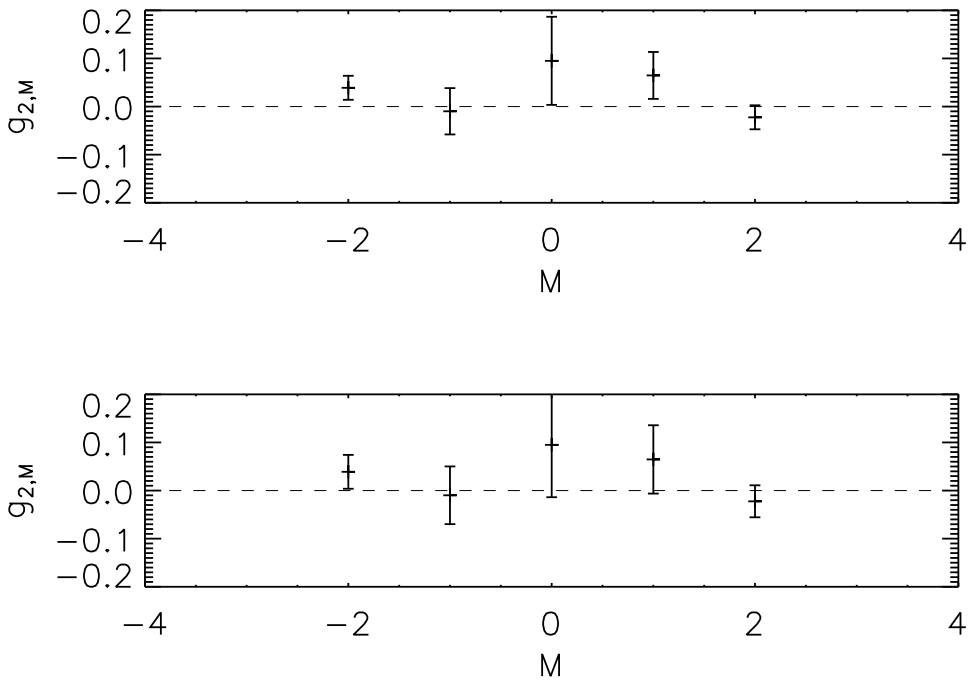

Figure 4.10: The quadrupole anisotropy parameters for each multipole marginalized over redshift slice with 1-sigma errors. The top panel includes errors calculated from the Fisher matrix. The bottom panel includes errors calculated using N-body simulations. Note that both results are consistent within two sigma with the null result, shown as the dashed line in both plots.

statistical isotropy.

The final values of g_{2M} and their covariance matrix are given in Table 4.2.

Finally, as a systematics test, we consider how the g_{2M}s change when we do *not* project out the extra templates $\{f_{2M}, h_{2M}\}$. We have shown in Table 4.3 the changes in g_{2M} when none of the systematics templates are included ("g_{2M} only") and when the f_{2M} templates are left out but h_{2M} is included ("g_{2M} & h_{2M}"). As we can see from the table, the exclusion of the f_{2M} templates has essentially no effect, but there is a substantial change in g_{2M} when the h_{2M} templates are excluded as well. However, since we expect the main effect of systematic power spectrum modulation across the sky to be taken into account via the h_{2M}s, and given that they change the result by $< 3\sigma$, we do not expect a significant residual systematic after the h_{2M}s and f_{2M}s have been projected out.

4.4.2 Comparison with CMB results

Groeneboom et al. [36] report evidence for a quadrupolar power asymmetry in the 5-year WMAP data. They investigated models of the form:

$$P(\mathbf{k}) = P(k)[1 + g_*(\hat{\mathbf{k}} \cdot \hat{\mathbf{n}})^2], \tag{4.35}$$

Table 4.2: The anisotropy coefficients, averaged over the 8 redshift slices, using the more conservative covariance matrix from the N-body simulations. Their covariance matrix is also given.

M	$g_{2M}/10^{-2}$	$\mathrm{Cov}[g_{2M}, g_{2M'}]/10^{-3}$				
-2	3.901	1.238	-0.327	0.741	0.879	-0.283
-1	-0.979	-0.327	3.599	-0.164	-0.566	-0.042
0	9.508	0.741	-0.164	11.866	-0.761	-1.348
1	6.479	0.879	-0.566	-0.761	5.044	-0.015
2	-2.235	-0.283	-0.042	-1.348	-0.015	1.106

Table 4.3: The changes in the anisotropy coefficients, averaged over the 8 redshift slices, when only some of the systematics templates are included. We present Δg_{2M} values, which are equal to the g_{2M} from the full analysis minus those with only some of the systematics templates, and the number of sigmas by which the correction differs from zero, $\Delta g_{2M}/\sigma(\Delta g_{2M})$.

	g_{2M} only		g_{2M} & h_{2M}
M	Δg_{2M}	$\Delta g_{2M}/\sigma(g_{2M})$	Δg_{2M}
-2	0.0128	0.63	0.0004
-1	0.1591	2.02	0.0027
0	0.2827	1.94	-0.0050
1	0.2830	2.78	0.0004
2	-0.0003	0.02	-0.0003

where g_* is the amplitude of the asymmetry and $\hat{\mathbf{n}}$ is its preferred axis. For $|g_*| \ll 1$, this is equivalent to our Eq. 4.2 with

$$\sum_{LM} g_{LM} R_{LM}(\hat{\mathbf{k}}) = g_* \left[(\hat{\mathbf{k}} \cdot \hat{\mathbf{n}})^2 - \frac{1}{3} \right] = \frac{2}{3} g_* P_2(\hat{\mathbf{k}} \cdot \hat{\mathbf{n}}) \tag{4.36}$$

and a slightly rescaled definition of the power spectrum, $P(k) = \bar{P}(k)(1 - \frac{1}{3} g_*)$. Here the $-\frac{1}{3}$ ensures that there is no $L = 0$ term in Eq. 4.36. Using the spherical harmonic addition theorem, we can see that this requires

$$g_{LM} = \frac{8\pi}{15} g_* \delta_{L2} R_{2M}(\hat{\mathbf{n}}). \tag{4.37}$$

We may use this to construct an estimator for g_* assuming a particular direction $\hat{\mathbf{n}}$; here we will take $\hat{\mathbf{n}}$ to be in the Groeneboom & Eriksen direction so that we can test for consistency with their value of g_*. The best estimator is

$$\hat{g}_* = \frac{15}{8\pi} \frac{\sum_{MM'} [\mathrm{Cov}^{-1}]_{MM'} \hat{g}_{2M} R_{2M'}(\hat{\mathbf{n}})}{\sum_{MM'} [\mathrm{Cov}^{-1}]_{MM'} R_{2M}(\hat{\mathbf{n}}) R_{2M'}(\hat{\mathbf{n}})}, \tag{4.38}$$

with uncertainty

$$\sigma(\hat{g}_*) = \frac{15}{8\pi} \frac{1}{\sqrt{\sum_{MM'} [\mathrm{Cov}^{-1}]_{MM'} R_{2M}(\hat{\mathbf{n}}) R_{2M'}(\hat{\mathbf{n}})}}; \tag{4.39}$$

here Cov is the 5×5 covariance matrix of the estimators for g_{2M} (see Table 4.2).

Using the WMAP W-band maps, and considering multipoles in the CMB out to $l_{\max} = 400$, Groeneboom et al. [36] find an asymmetry of $g_*^{\rm CMB} = 0.29 \pm 0.031$ with an axis of maximum power in the direction $(l, b) = (94°, 26°)$, which they attribute to an unknown systematic effect because different signals are observed in the V and W bands and the apparent alignment with the Ecliptic poles. Using the above projection procedure, we find an amplitude $g_*^{\rm LRG} = 0.006 \pm 0.036$ in this direction. Groeneboom et al. also did their fit using the WMAP V-band maps, finding $g_*^{\rm CMB} = 0.14 \pm 0.034$ in the direction $(l, b) = (97°, 27°)$; when we project our LRG anisotropy coefficients onto this axis, we find $g_*^{\rm LRG} = 0.007 \pm 0.037$. Foregrounds and noise mis-estimation have been disfavored as possible candidates [31]. A possible cause for the appearance of statistical anisotropy in the CMB data would be the ellipticity of the WMAP beams, which when combined with the survey strategy could result in a preferred axis in the direction of the Ecliptic Poles [35, 102, 37, 38]. Specifically, Hanson et al. [38] find that once asymmetric beam effects are subtracted, the data is consistent with the isotropic model; however Groeneboom et al. [36] evaluated the resulting effect and found it to be negligible. The WMAP 7-year analysis finds no known instrumental effect other than beam asymmetry that can cause the anomaly, but they have not yet completed a full simulation of beam asymmetry effects on quadrupolar power modulation [31]. We also note the the WMAP team has already accounted for these beam effects in their estimation of the power spectrum, so this systematic in the quadrupolar anisotropy does *not* affect the cosmological parameters derived from WMAP.

Thus the cause of the apparent asymmetry in the WMAP maps is not definitively known. In any case, our LRG analysis finds no anisotropy in this direction. It is possible that g_{2M} is different at the two scales probed by the CMB and the LRG sample. In most variants of inflation, where each e-fold of expansion is similar to the previous one with $\sim \mathcal{O}(1/N)$ deviations (where N is the number of e-folds remaining), we would expect g_{2M} to vary smoothly with the number of e-folds, or $\ln k$. We find the effective scales probed by Groeneboom et al.'s CMB analysis [36] and our LRG analysis are 0.020 Mpc^{-1} and 0.15 Mpc^{-1}, respectively (see D), which differ by only 2.0 e-folds. It would be very surprising if inflation were not only anisotropic but also managed to produce a scale-dependent anisotropy that varied over so short a baseline.

4.4.3 Direction-marginalized constraint on g_*

The above analyses have either set constraints on a general g_{2M} (a 5-dimensional parameter space) or on g_* for a fixed anisotropy axis (a 1-dimensional parameter space). It is however of interest to set constraints on general axisymmetric quadrupolar anisotropies, such as Eq. 4.36, which would arise if there were a single preferred axis during inflation. This is a 3-dimensional parameter space: there is an amplitude g_* and a direction $\hat{\mathbf{n}} \in \mathrm{S}^2$.

We may set constraints on g_* via a Bayesian analysis in which a uniform prior is placed on $\hat{\mathbf{n}}$, as has been done in several previous statistical anisotropy analyses [35, 103]. Our problem - setting a limit on the amplitude of an anisotropy while marginalizing over its direction - is similar to that performed by Ref. [103] for the large scale structure dipole; we follow the same methodology, although we note that for the quadrupolar asymmetry g_* could be positive or negative ("prolate" and "oblate" power anisotropies are different and cannot be rotated into each other). The marginalized likelihood function for g_* is

$$\begin{aligned}\mathcal{L}(g_*) &= \int \exp\left\{-\frac{1}{2}\sum_{MM'}[\mathrm{Cov}^{-1}]_{MM'}\left[\hat{g}_{2M}-\frac{8\pi}{15}g_* R_{2M}(\hat{\mathbf{n}})\right]\right. \\ &\quad \left.\times\left[\hat{g}_{2M'}-\frac{8\pi}{15}g_* R_{2M'}(\hat{\mathbf{n}})\right]\right\} d^2\hat{\mathbf{n}}, \end{aligned} \tag{4.40}$$

where $\hat{g}_{2M}$ are the estimated anisotropy coefficients and Cov is their 5×5 covariance matrix. If we set a uniform prior on g_*, as done by Groeneboom & Eriksen [35], then we may divide $\mathcal{L}(g_*)$ by its integral $\int \mathcal{L}(g_*)\,dg_*$ and treat it as a posterior probability distribution. If we do this, then we find that 68% of the posterior distribution is contained within $-0.12 < g_* < +0.10$ and 95% within $-0.41 < g_* < +0.38$. Note that the distribution has very non-Gaussian tails because of the large uncertainty on g_{20}: a quadrupole anisotropy aligned with the Galactic axis would be difficult to detect given our sky coverage. There is a small probability for such an alignment to occur and not produce measurable g_{2M} $(M \neq 0)$ even if g_* is large.

4.5 Conclusions

We have conducted a search for statistical anisotropy in the galaxy distribution. Statistical anisotropy can manifest from the direction-dependent primordial power spectrum shown in Eq. 4.2 with the magnitude of the anisotropy parametrized by g_{LM}. This phenomenon causes the angular galaxy power spectrum $C_{g,l}$ to be generalized by $D^{LM}_{g,ll'}$, which includes g_{LM}. We used estimators formulated by Padmanabhan et al. [79] and a sample of LRGs from SDSS to search for evidence of quadrupolar anisotropy parametrized by g_{2M}. We found g_{2M} for all M to be within 2σ of zero. Using our estimates of g_{2M} and assuming a symmetry axis in the direction $(l, b) = (94^\circ, 26^\circ)$, we calculated the anisotropy amplitude $g_* = 0.006 \pm 0.036\,(1\sigma)$. This confirms that the previously identified anisotropy in the WMAP maps (already believed to be a systematic effect) is not of primordial origin. When marginalizing over the symmetry axis direction and assuming a uniform prior for g_*, we constrain $-0.41 < g_* < +0.38$ with a 95% confidence level.

Looking forward, we expect much better sensitivity to g_* from future galaxy surveys. For fixed sky coverage, the uncertainty in g_{2M} is proportional to the inverse square-root of the number of

modes measured, i.e., it is proportional to $l_{\rm max}^{-1} N_z^{-1/2}$ where $l_{\rm max}$ is the maximum multipole at which the galaxy distribution is well-sampled, and N_z is the number of effectively independent redshift slices. The largest advance may be possible with future large-volume spectroscopic surveys intended to study baryon oscillations. Here the effective number of redshift slices is $N_z \sim k_{\rm max} \Delta r/\pi$, where Δr is the radial width of the survey; for surveys that reach out to $z \approx 2$ this is $N_z \sim 100$ (instead of 8 here). As this redshift corresponds to a factor of ~ 3 increase in distance relative to the SDSS LRGs, we would expect that for similar sampling $nP(k)$ $l_{\rm max}$ should increase by a factor of 3. Thus such a survey should in principle be able to improve measurements of g_{2M} by an order of magnitude relative to those presented here. Further improvements in g_{20} might also be possible if improvements in the dust map or work in redder bands allows one to work at lower Galactic latitudes.

Acknowledgements

We thank N. Padmanabhan and S. Ho for providing the LRG sample and for their useful feedback. We also thank M. Kamionkowski for helpful comments.

AP acknowledges the support of the NSF. This work was supported by DOE DE-FG03-92-ER40701, NASA NNG05GF69G, the Gordon and Betty Moore Foundation, and a NASA Einstein Probe mission study grant, "The Experimental Probe of Inflationary Cosmology".

CH is supported by the US Department of Energy under contract DE-FG03-02-ER40701, the National Science Foundation under contract AST-0807337, and the Alfred P Sloan Foundation.

Funding for the Sloan Digital Sky Survey (SDSS) and SDSS-II has been provided by the Alfred P Sloan Foundation, the Participating Institutions, the National Science Foundation, the US Department of Energy, the National Aeronautics and Space Administration, the Japanese Monbukagakusho, the Max Planck Society, and the Higher Education Funding Council for England. The SDSS Web site is http://www.sdss.org/.

The SDSS is managed by the Astrophysical Research Consortium (ARC) for the Participating Institutions. The Participating Institutions are the American Museum of Natural History, Astrophysical Institute Potsdam, University of Basel, University of Cambridge, Case Western Reserve University, The University of Chicago, Drexel University, Fermilab, the Institute for Advanced Study, the Japan Participation Group, The Johns Hopkins University, the Joint Institute for Nuclear Astrophysics, the Kavli Institute for Particle Astrophysics and Cosmology, the Korean Scientist Group, the Chinese Academy of Sciences (LAMOST), Los Alamos National Laboratory, the Max Planck Institute for Astronomy (MPIA), the Max Planck Institute for Astrophysics (MPA), New Mexico State University, Ohio State University, University of Pittsburgh, University of Portsmouth, Princeton University, the United States Naval Observatory, and the University of Washington.

Chapter 5

Search for Non-Gaussianity with Photometric Quasars

5.1 Introduction

Inflation is the standard paradigm for the generation of perturbations in large-scale structure (LSS) [106, 107, 108, 109]. Although the inflationary paradigm has successfully predicted various properties of the observable universe, including flatness and a nearly scale-invariant spectrum of perturbations [110, 111, 112, 113, 114], the correct model of inflation has yet to be determined. The simplest inflation models predict nearly Gaussian primordial perturbations, though more complex models such as multi-field inflation posit a departure from a Gaussian distribution. Alternatives to inflation, such as the ekpyrotic model, also predict non-Gaussian primordial perturbations. Since a detection of non-Gaussianity in cosmological data would discriminate between these fundamentally different models, much work is being done to constrain non-Gaussianity, both in LSS through the galaxy distribution and through anisotropies in the cosmic microwave background (CMB). Primordial non-Gaussianity is readily probed through measurement of the bispectrum of the CMB, in which a nonzero measurement constitutes a "smoking gun" detection, modulo any systematic effects. Some alternative probes of non-Gaussianity in LSS include the galaxy bispectrum, which is plagued by nonlinearities, and galaxy cluster abundances and dark-matter halo clustering, which suffer from low-number statistics. The accepted parametrization of primordial non-Gaussianity is to introduce a quadratic term to the primordial potential Φ, written as

$$\Phi = \phi + f_{\rm NL}(\phi^2 - \langle\phi^2\rangle)\,, \tag{5.1}$$

where ϕ is a Gaussian random field [41, 42]. This form describes local-type non-Gaussianity with an amplitude $f_{\rm NL}$. The latest constraint on $f_{\rm NL}$ is from the Wilkinson Microwave Anisotropy Probe's

[0]The work in progress presented in this chapter was done in collaboration with Christopher Hirata. Reproduced with permission.

(WMAP) [32] Seven-Year bispectrum, which gives $-10 < f_{\rm NL} < +74$ at 95% C.L. [43]. Planck [33], which will soon give results from its first data release, is expected to produce constraints on $f_{\rm NL}$ of order $\sigma(f_{\rm NL}) \sim 7$ [115].

One useful effect of non-Gaussianity that has gained much attention is a distinct scale-dependent bias on large scales in galaxy clustering [44, 45]; probing this effect is the method we seek to employ in this chapter. Specifically, it has been shown that $f_{\rm NL}$-type non-Gaussianity produces a shift in the bias that behaves as $\Delta b(k) \propto f_{\rm NL}/k^2$; hence, a positive (negative) $f_{\rm NL}$ leads to more (less) clustering on large-scales. Various authors have used this method to constrain $f_{\rm NL}$. Slosar et al. [45], using the Sloan Digital Sky Survey (SDSS) [80] Data Release 5 (DR5) [92], derived the constraints $-82 < f_{\rm NL} < +70$ at 95% C.L. for the photometric quasi-stellar-object (photo-QSO) sample and $-29 < f_{\rm NL} < +70$ at 95% C.L. for QSOs combined with other data sets, such as the integrated Sachs-Wolfe effect (ISW) and luminous red galaxies (LRGs). Recently, Tseliakhovich et al. [116] extended this analysis to a two-parameter curvaton model [117, 118, 119, 120, 121, 122] while others have sought to use this method in combination with other data sets [123, 124]. DeBernardis et al. [124] also showed that Planck and EUCLID together could possibly detect $f_{\rm NL} \sim 5$.

In this chapter, we prepare the SDSS Data Release 6 (DR6) [125] Richards et al. photo-QSO sample [126] to constrain $f_{\rm NL}$ with the methodology of Ref. [45]. The photo-QSO sample, probing large redshifts, is able to probe scale-dependent bias more effectively than other matter tracers. The goal is to probe a larger redshift range than the previous analysis, using redshifts as low as $z = 0.9$ and as high as $z = 2.9$. A search for non-Gaussianity using this data set was previously done by Xia et al. in Ref. [127]. The authors used the entire sample (limited to UV-excess QSOs) to constrain f_{NL}. In this work we divide the quasars into three photometric redshift slices, which should probe more modes in order to find tighter constraints on f_{NL}. Much of this work involves removing systematic effects in order to construct accurate angular power spectra. We construct the cross-correlation between two of the redshift slices to test for systematic effects. We find that many problems remain in the data despite our efforts to remove systematics. Future work will involve determining the origin(s) of the remaining systematic issues in order to properly constrain f_{NL} and the curvaton model. The systematics that are removed may also need to be accounted in constructing future QSO samples.

The plan of this chapter is as follows: in Sec. 5.2 we describe the photo-QSO data we use in the analysis. We then show the correction to the galaxy bias due to non-Gaussianity, as well as the methodology we use in this analysis, in Sec. 5.3. In Sec. 5.4, we discuss the methods we used to remove systematics from our data set. We also in this section construct the cross-correlation between the first and third redshift slices to search for systematics. In Sec. 5.5, we discuss our current progress. Wherever not explicitly mentioned, we assume a flat ΛCDM cosmology with parameters compatible with WMAP7 data release.

5.2 Choice of Sample

We use photometric QSOs from SDSS DR6 [125] to trace the matter density and construct its angular spectrum. The SDSS consists of a 2.5 m telescope [81] with a 5 filter (*ugriz*) imaging camera [82] and a spectrograph. Automated pipelines are responsible for the astrometric solution [83] and photometric calibration [84, 85, 86, 87]. Bright galaxies, luminous red galaxies (LRGs), and quasars are selected for follow-up spectroscopy [88, 89, 90, 91]. The data used here were acquired between August 1998 and June 2006 and are included in SDSS Data Release 6 [125].

Specifically, we use the photometric QSO catalog composed by Richards et al. [126] (hereafter RQCat). The entire catalog consists of 1,172,157 objects selected as QSOs from the SDSS DR6 photometric imaging data. QSOs are the brightest objects at large redshifts ($z > 1$), making them better tracers of the matter density at large scales than LRGs. We limit our dataset to UV-excess QSOs with high kernel-density-estimator (KDE) QSO probability densities. Specifically, we implement this choice by requiring the catalog columns **good** > 0, **uvxts** $= 1$, and **qsodens** > 0. We use QSOs from the 3 redshift slices ranging from $z_{\rm p,min} = 0.9$ to $z_{\rm p,max} = 2.9$. For the survey geometry we construct the DR6 survey mask as union of the survey runs downloaded from the SDSS CAS server. We omitted runs 2189 and 2190 because many objects in these runs were cut from the catalog. This mask was pixelized using the MANGLE software [128, 129]. We plot the redshift distributions in Fig. 5.1, while their properties are given in Table 5.1. The procedure for constructing the redshift distributions is described in Appendix E and is similar to that described in Ref. [94]. We pixelize the QSOs as a number overdensity, $\delta_q = (n - \overline{n})/\overline{n}$, onto a HEALPix pixelization [95] of the sphere with $N_{res} = 256$. We then reject pixels with extinction $E(B-V) \geq 0.05$, full widths at half-maximum of its point-spread function (PSF) FWHM ≥ 2 arcsec, and stellar densities (smoothed with a 2° FWHM Gaussian) $n_{stars} \geq 562$ stars/deg^2 (twice the average stellar density), the same cuts implemented in Ref. [94]. We implement these cuts using dust maps from Ref. [130] and stars ($18.0 < r < 18.5$) from the SDSS DR6 [125]. We also reject pixels for which the survey region covers less than 80% of the pixel area. In addition, RQCat contained regions that seemed to be undersampled. We excise angular rectangles around these regions to remove them from the data. The angular rectangles in celestial coordinates that were removed are $(\alpha, \delta) = (122^\circ$–$139^\circ, -1.5^\circ$–$(-0.5)^\circ)$, $(121^\circ$–$126^\circ, 0^\circ$–$4^\circ)$, $(119^\circ$–$128^\circ, 4^\circ$–$6^\circ)$, $(105^\circ$–$120^\circ, 6^\circ$–$25^\circ)$, $(111.5^\circ$–$117.5^\circ, 25^\circ$–$30^\circ)$, $(110^\circ$–$116^\circ, 32^\circ$–$35^\circ)$, $(246^\circ$–$251^\circ, 8.5^\circ$–$13.5^\circ)$, $(255^\circ$–$270^\circ, 20^\circ$–$40^\circ)$, and $(268^\circ$–$271^\circ, 46^\circ$–$49^\circ)$. After these cuts, the survey region comprises 131,787 pixels covering a solid angle of 6913 deg^2. The QSO maps for each slice are shown in Fig. 5.2. Although there appears to be striping along the survey latitudes in redshift slices z01 and z02, we account for this systematic effect in our analysis, as we will show in Sec. 5.4.

Table 5.1: Properties of the 3 QSO photometric redshift slices; $z_{\rm p}$ is the photometric redshift range, and $z_{\rm mean}$ is the mean (true) redshift of the slice, and N_{qso} is the number of QSOs in the redshift slice.

Label	$z_{\rm p}$	$z_{\rm mean}$	N_{qso}
z01	0.9-1.3	1.230	64,320
z02	1.6-2.0	1.731	85,442
z03	2.3-2.9	2.210	11,589

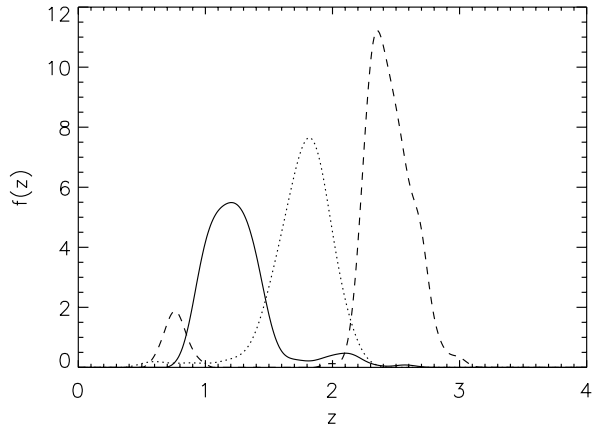

Figure 5.1: The redshift distributions for the QSO photometric redshift slices z01 (solid), z02 (dotted) and z03 (dashed).

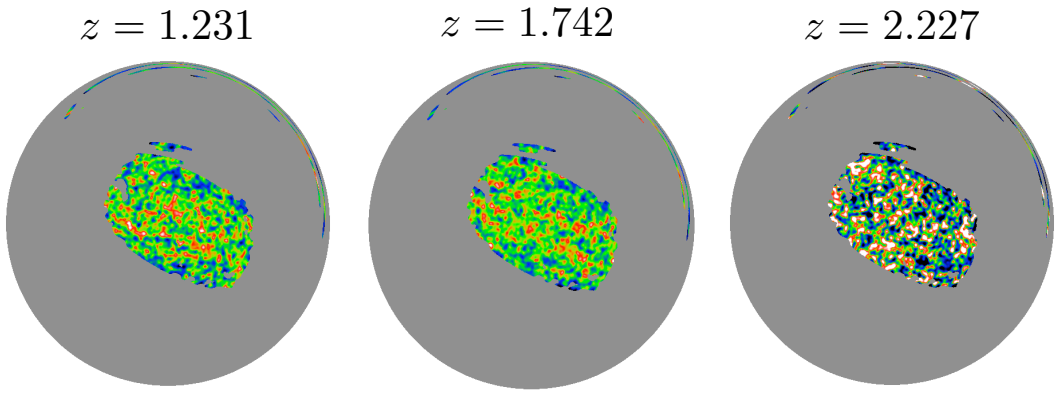

Figure 5.2: The QSO density in the 3 photometric redshift slices. The 180° radius caps are displayed in a Lambert azimuthal equal-area projection, with the north Galactic pole at the centre, $l = 0°$ at right, and $l = 90°$ at bottom. The labels indicate the characteristic redshift of each slice. Notice the striping in redshift slices z01 and z02; we account for this systematic in Sec. 5.4.

5.3 Theory and Method

5.3.1 Scale-dependent bias in the halo distribution as seen in the sky

We assume the halo model scenario (see Ref. [131] for a detailed review), in which all matter is contained in a distribution of halos on large scales which mimics the distribution of matter on small scales. In the Gaussian case, fluctuations on small and large scales are uncorrelated. However, a signature of local-type non-Gaussianity is that the $f_{\rm NL}\phi^2$ term in the gravitational potential causes small-scale matter fluctuations to correlate with large-scale halo fluctuations due to mixing of their respective gravity perturbations. Positive (negative) $f_{\rm NL}$ incurs a positive (negative) correlation between scales and an increase (decrease) in the halo bias on large scales as compared to the Gaussian case. Specifically, this k-dependent shift in the bias was derived for a general halo mass function $n(M)$ in Ref. [45] and is of the form

$$\Delta b(M,k) = \frac{3\Omega_m H_0^2}{c^2 k^2 T(k) D(z)} f_{\rm NL} \frac{\partial \ln n}{\partial \ln \sigma_8}\,, \tag{5.2}$$

while for the case of a universal mass function, such as the Press-Schechter [132] or Sheth-Tormen [133] mass functions, this expression was shown in Ref. [45] to reduce to

$$\Delta b(M,k) = 3 f_{\rm NL}(b-p)\delta_c \frac{\Omega_m}{k^2 T(k) D(z)} \left(\frac{H_0}{c}\right)^2\,, \tag{5.3}$$

the expression first derived in Dalal et al. [44]. Here, $T(k)$ is the transfer function, $D(z)$ is the the growth function normalized such that $D(z=0)=1$, c is the speed of light, Ω_m and H_0 are the matter density and the Hubble parameter today, respectively, σ_8 is the rms overdensity in a sphere of radius $R = 8h^{-1}$ Mpc, and δ_c is the critical density of spherical collapse. The parameter p ranges from 1 for LRGs, which populate all halos equally, to 1.6 for QSOs that populate only recently merged halos. We use $p = 1.6$ in our analysis to model the scale-dependent bias of QSOs.

5.3.2 Angular power spectrum due to scale-dependent bias and non-Gaussianity

We probe scale-dependent bias and estimate $f_{\rm NL}$ using its effects on the angular power spectrum C_l. This spectrum, whose expression, including redshift space distortions, is given in Padmanabhan et al. [79], can be written as a sum of three terms for the scale-dependent bias case in the form

$$C_l = C_l^0 + f_{\rm NL} C_l^f + f_{\rm NL}^2 C_l^{ff}\,. \tag{5.4}$$

The three terms in this expression are integrals given by

$$\begin{aligned} C_l^0 &= 4\pi \int \frac{dk}{k} \Delta^2(k) |W_l^0(k) + W_l^r(k)|^2 \\ C_l^f &= 8\pi \int \frac{dk}{k} \Delta^2(k) [W_l^0(k) + W_l^r(k)]^* W_l^f(k) \\ C_l^{ff} &= 4\pi \int \frac{dk}{k} \Delta^2(k) |W_l^f(k)|^2 \,, \end{aligned} \tag{5.5}$$

where $\Delta(k)$ is the linear matter power spectrum today[1] and

$$\begin{aligned} W_l^0(k) &= \int D(z) f(z) \frac{H(z)}{c} j_l[k\chi(z)] dz \\ W_l^r(k) &= \int \frac{\Omega_m^{0.6}(z)}{b(z)} D(z) f(z) \frac{H(z)}{c} \left\{ \frac{2l^2+2l-1}{(2l+3)(2l-1)} j_l[k\chi(z)] \right. \\ &\quad \left. - \frac{l(l-1)}{(2l-1)(2l+1)} j_{l-2}[k\chi(z)] - \frac{(l+1)(l+2)}{(2l+1)(2l+3)} j_{l+2}[k\chi(z)] \right\} dz \\ W_l^f(k) &= \frac{3\delta_c \Omega_m}{k^2 T(k)} \left(\frac{H_0}{c} \right)^2 \int \left(1 - \frac{p}{b(z)} \right) f(z) \frac{H(z)}{c} j_l[k\chi(z)] dz \,. \end{aligned} \tag{5.6}$$

The scale-independent bias $b(z)$ in Eq. 5.6 is assumed to be inversely proportional to the growth function, e.g.,

$$b(z) = \frac{b_0}{D(z)} \,, \tag{5.7}$$

where b_0 is the bias at redshift zero. We estimate b_0 for each redshift slice by normalizing according to the condition

$$\int \frac{dn}{dz} dz = \int \frac{f(z)}{b(z)} dz = 1 \,, \tag{5.8}$$

as done in Ref. [45]. The C_ls in Eq. 5.5 were calculated for all 3 redshift slices and presented in Fig. 5.3. Because redshift-space distortions and scale-dependent bias are significant on large scales, redshift-space distortions must be taken into account in order to estimate $f_{\rm NL}$ correctly. To illustrate the effects of scale-dependent bias induced by non-Gaussianity on the angular power spectrum, we also graph the behavior of C_l for nonzero $f_{\rm NL}$ in Fig. 5.3

5.3.3 Estimators of non-Gaussianity

In this section we develop the estimators we will use in future work to constrain f_{NL} as well as the curvaton model. The model for the angular power spectrum described in the previous section leads

[1] Ref. [45] confirmed that nonlinearities are negligible for $k < 0.1h$ Mpc^{-1}. For our redshifts, this corresponds to $l < 270$. We only use C_l for $l < 250$, so it is safe to use the linear matter power spectrum in our analysis.

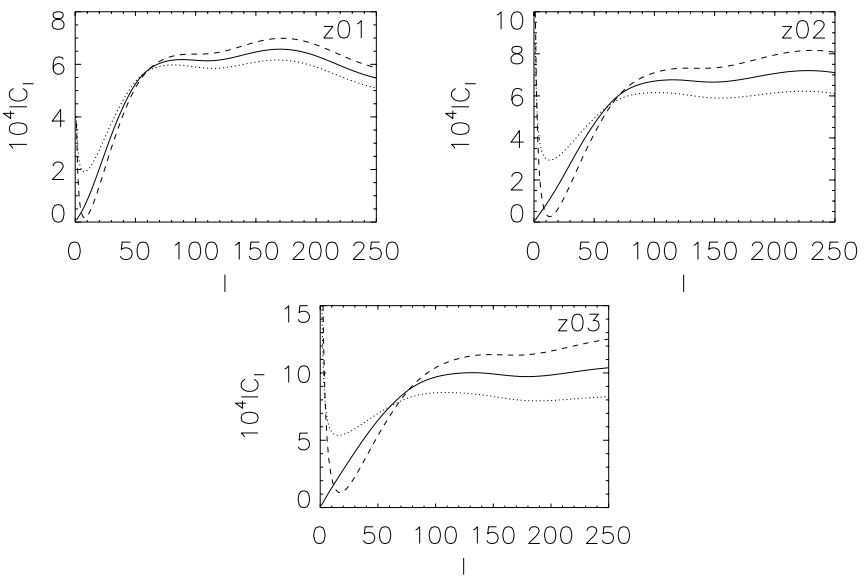

Figure 5.3: The predicted QSO angular power spectra for null and nonzero f_{NL}. The solid lines are the spectra for the Gaussian case, and the dotted (dashed) lines represent the $f_{NL} = 100\,(-100)$ case.

to a three-parameter model of the observed covariance matrix $\mathbf{C}$ for the QSO map of the form

$$\mathbf{C} = p_1\mathbf{C}^0 + p_2\mathbf{C}^f + p_3\mathbf{C}^{ff} + \mathbf{C}^N\,, \tag{5.9}$$

where $\mathbf{C}^0$, $\mathbf{C}^f$, and $\mathbf{C}^{ff}$ are the $N_{\rm pix} \times N_{\rm pix}$ covariance matrices between pixels due to C_l^0, C_l^f, and C_l^{ff}, respectively, of the form

$$C_{ij}^A = \sum_l \left(\frac{2l+1}{4\pi}\right) Q_l C_l^A P_l[\cos(\hat{\mathbf{n}}_i \cdot \hat{\mathbf{n}}_j)]\,, \tag{5.10}$$

$A = \{0, f, ff\}$, $\mathbf{C}^N$ is the Poisson noise matrix given by

$$C_{ij}^N = \frac{\delta_{ij}}{\overline{n}}\,, \tag{5.11}$$

in terms of the mean number of galaxies per pixel $\overline{n}$, and $\mathbf{p} = (p_1, p_2, p_3)$ is a parameter vector in a space describing a class of models for $\mathbf{C}$. For our specific model, p_1 quantifies any missing bias not taken into account (ideally, $p_1 = 1$), $p_2 = f_{\rm NL}$, and $p_3 = f_{\rm NL}^2$. Finally, Q_l is a window function similar to that for CMB anisotropies that appears due to finite pixel size

$$Q_l \;=\; \left\langle \frac{1}{\theta_{\rm pix}^2} \int_{-\theta_{\rm pix}/2}^{\theta_{\rm pix}/2} dx \int_{-\theta_{\rm pix}/2}^{\theta_{\rm pix}/2} dy\, e^{i(l_x x + l_y y)} \right\rangle$$

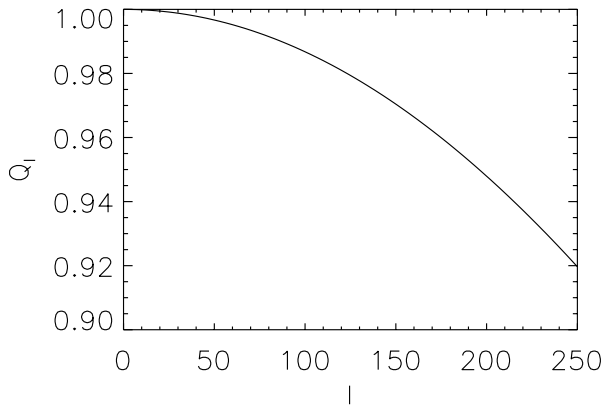

Figure 5.4: The window function Q_l for $\theta_{\rm pix} = 3.997$ mrad.

$$= \frac{1}{2\pi}\int_0^{2\pi} d\phi \frac{\sin^2(l\theta_{\rm pix}\cos\phi/2)\sin^2(l\theta_{\rm pix}\sin\phi/2)}{(l\theta_{\rm pix}/2)^4\cos^2\phi\sin^2\phi}\,, \tag{5.12}$$

where $\theta_{\rm pix}$ is the angular pixel size in radians, which for our map is $\theta_{\rm pix} = 0.003997$. We evaluate this expression numerically and present its behavior for our map in Fig. 5.4.

We will use a quadratic estimator [98, 99] to measure the parameter vector $\mathbf{p}$ according to

$$\hat{\mathbf{p}} = \mathbf{F}^{-1}\mathbf{q}\,, \tag{5.13}$$

where

$$\begin{aligned} F_{ij} &= \frac{1}{2}{\rm tr}\left[\mathbf{C}_{,\rm i}\,\mathbf{C}^{-1}\mathbf{C}_{,\rm j}\,\mathbf{C}^{-1}\right] \\ q_i &= \frac{1}{2}\delta_{\mathbf{q}}^{\mathbf{T}}\mathbf{C}^{-1}\mathbf{C}_{,i}\,\mathbf{C}^{-1}\delta_{\mathbf{q}}\,, \end{aligned} \tag{5.14}$$

are the Fisher matrix and quad vector, respectively, $\delta_{\mathbf{q}}$ is the data vector of length $N_{\rm pix}$ describing the QSO overdensity map of a particular redshift slice, and $\mathbf{C}_{,i} = \partial\mathbf{C}/\partial p_i$. We set $f_{\rm NL} = 0$ as our prior for C_l to construct the covariance matrix templates. Note the matrix inversion and trace estimation are done by the iterative and stochastic methods described in detail in Refs. [100, 79].

Since p_3 is theoretically the square of p_2, these parameters are expected to be correlated. Thus, to get the best estimate of $f_{\rm NL}$, we must perform a Bayesian maximum likelihood analysis where we construct the likelihood function $\mathcal{L}(f_{\rm NL})$ using our estimate $\hat{\mathbf{p}}$ and find the value of $f_{\rm NL}$ that maximizes it as well as the 95% confidence interval. The likelihood function (unnormalized) is of the form

$$\mathcal{L}(f_{\rm NL}) = \prod_{z-{\rm slices}} \exp -\frac{1}{2}\left[({\rm Cov})^{-1}_{p_2,p_2}(f_{\rm NL} - \hat{p}_2)^2\right.$$

$$+ 2(\mathrm{Cov})^{-1}_{p_2,p_3}(f_{\mathrm{NL}} - \hat{p}_2)(f^2_{\mathrm{NL}} - \hat{p}_3) + (\mathrm{Cov})^{-1}_{p_3,p_3}(f^2_{\mathrm{NL}} - \hat{p}_3)^2\Big] \,, \tag{5.15}$$

where Cov is the 2×2 covariance matrix between the estimates of p_2 and p_3 and the exponential is multiplied over the 3 redshift slices.

We will also extend the search for non-Gaussianity to the two-parameter curvaton model probed in Ref. [116]. In the curvaton model, the inflaton φ alone drives the exponential expansion in the early universe while the curvaton σ produces the initial perturbations once inflation is over. The two-parameter model allows both fields to contribute to the initial perturbations. Though the curvaton itself is a Gaussian field, it is predicted to produce significant inflation since the initial perturbations in this model increase as σ^2. This model is parametrized by $\tilde{f}_{\mathrm{NL}}$, the non-Gaussianity parameter due to the curvaton, and ξ, the ratio of inflaton to curvaton contributions to the perturbations. It can be shown that our Eq. 5.4 can be rewritten for this model as

$$C_l = C^0_l + \frac{\tilde{f}_{\mathrm{NL}}}{(1+\xi^2)^2} C^f_l + \frac{\tilde{f}^2_{\mathrm{NL}}}{(1+\xi^2)^3} C^{ff}_l \,, \tag{5.16}$$

where C^0_l, C^f_l, and C^{ff}_l have the same form as in Eq. 5.5. Thus, we can use the same estimates for $\mathbf{p}$ as before to estimate $(\tilde{f}_{\mathrm{NL}}, \xi)$ and to find the 95% confidence contour, except that the likelihood function (unnormalized) is now given by

$$\begin{aligned}\mathcal{L}(\tilde{f}_{\mathrm{NL}}, \xi) = \prod_{z-\mathrm{slices}} \exp -\frac{1}{2} \Bigg\{ & (\mathrm{Cov})^{-1}_{p_2,p_2} \left[\frac{\tilde{f}_{\mathrm{NL}}}{(1+\xi^2)^2} - \hat{p}_2 \right]^2 \\ & + 2(\mathrm{Cov})^{-1}_{p_2,p_3} \left[\frac{\tilde{f}_{\mathrm{NL}}}{(1+\xi^2)^2} - \hat{p}_2 \right] \left[\frac{\tilde{f}^2_{\mathrm{NL}}}{(1+\xi^2)^3} - \hat{p}_3 \right] \\ & + (\mathrm{Cov})^{-1}_{p_3,p_3} \left[\frac{\tilde{f}^2_{\mathrm{NL}}}{(1+\xi^2)^3} - \hat{p}_3 \right]^2 \Bigg\} \,. \end{aligned} \tag{5.17}$$

5.4 Systematics

The Richards et al. catalog we analyze requires much processing in order to be useful to constrain non-Gaussianity. For example, although we remove pixels with large extinctions (see Sec. 5.2), we must perform additional processing to project out the systematic effects that extinction produces in the remaining pixels. Another systematic to project is red stars ($g - r > 1.4$), which prevented Ref. [45] from using the $z < 1.45$ QSO sample in its f_{NL} constraints. We also note apparent striping, which we can project out without having to remove the striping manually. This striping should occur along lines of constant survey latitude η, which are given in terms of celestial coordinates (α, δ) by

$$\tan(\eta + 32.5^\circ) = \tan\delta \csc(\alpha - 95^\circ) \,. \tag{5.18}$$

We use the method demonstrated in Ho et al. [94] where a covariance template for each systematic is added to the prior covariance matrix $\mathbf{C}^{\rm true}$ in order to estimate C_l and $f_{\rm NL}$ correctly, according to the expression

$$\mathbf{C} = \mathbf{C}^{\rm true} + \sum_{i=sys} \zeta_i \mathbf{E}_i \mathbf{E}_i^T \,, \tag{5.19}$$

where $\mathbf{C}$ yields an unbiased estimator when $\zeta \to \infty$ and the vector (over pixel) $\mathbf{E}_i$ is the template for systematic i. The templates are set to be parallel (in pixel space) to the change in $\delta_{\mathbf{q}}$ due to the systematic. This condition gives templates for extinction in the form $E_{{\rm extinc},i} = E(B-V)_i$ and for red stars in the form $E_{{\rm red\,stars},i} = (n_{{\rm red\,stars},i} - \overline{n}_{\rm red\,stars})/\overline{n}_{\rm red\,stars}$. Since SDSS scanned along stripes of constant η with a width of $\Delta\eta = 2.5°$, we separate the survey region into 2.5°-wide stripes and create a template for each slice. The striping template for each stripe consists of either +1 (for pixels in the stripe) or 0 (for pixels outside the stripe). We set ζ_i for each template such that the values of the Fisher and quad vectors converge. This condition is met by setting $\zeta_{\rm extinc} = 100$, $\zeta_{\rm red\,stars} = 1$, and $\zeta_\eta = 100$ for redshift slices z01 and z02. For z03, we raise $\zeta_{\rm extinc}$ and ζ_η to 500 to achieve convergence.

While this method should keep extinction and red stars from contaminating our quadratic estimator, we must test our data to make sure there are not any other systematics we have not taken into account. This is particularly true in searching for non-Gaussianity because large-scale excess power has a degeneracy as both a signature of nonzero f_{NL} and a signature of a systematic error across the map such as photometric calibration errors or stellar contamination. To test for systematics, we construct the cross-correlation power spectrum between redshift slices z01 and z03. A large class of systematic effects should appear in all three redshift slices, resulting in a statistically significant cross-correlation. The resulting spectra is shown in Fig. 5.5. We see that there is a sizable cross-correlation between these redshift slices. In particular, the largest cross-correlation appears in the second l-bin ($7 \leq l < 12$), which shows a 3.38σ-detection. This leads to the suspicion that a systematic error remains in the data samples.

5.5 Discussion

This chapter presents the data samples and analysis tools needed to construct new constraints on non-Gaussianity from scale-dependent bias using photometric quasars in SDSS DR6. We seek to extend previous work by Slosar et al. to a larger redshift range in order to tighten limits on f_{NL}. We divide the photo-QSO catalog by Richards et al. into three redshift slices. We also construct quadratic estimators of the angular power spectra as well as estimators for f_{NL} which we will use in future work. We also discuss how our estimators are modified to project out systematic effects.

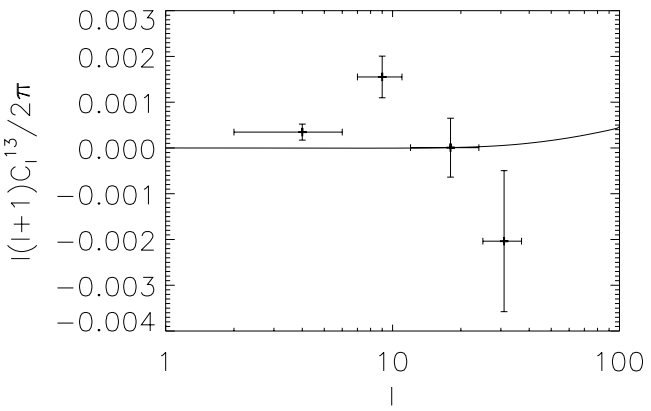

Figure 5.5: The measured cross-correlation angular power spectrum between QSO redshift slices z01 and z03. The crosses are the measured spectrum and the solid line is the predicted spectrum. Note that the predicted spectrum is not exactly zero because the redshift distributions have a small overlap.

We end by constructing an angular cross-power spectrum between the first and third redshift slices to test for any remaining systematic effects, which shows a positive detection of systematic error.

This work shows deep problems with the RQCat for estimating f_{NL} (or any other cosmological parameters) within multiple redshift slices. The previous analysis performed using this data [127] placed all the quasars in one redshift slice. A map of all the UVX objects in the RQCat, shown in Fig. 5.6, appears to have some of the same systematic issues we see in the maps of the redshift slices from Fig. 5.2, including striping. Striping was not mentioned in the analysis of Ref. [127], which may signal that the error bars in their analysis were underestimated. It is possible there are other systematic effects such as calibration errors for which we have not accounted. Further work to remove all systematics must be undertaken before the RQCat data sample can be used to constrain f_{NL} at multiple redshifts.

Acknowledgements

This work was supported by DOE DE-FG03-92-ER40701, NASA NNG05GF69G, the Gordon and Betty Moore Foundation, and a NASA Einstein Probe mission study grant, "The Experimental Probe of Inflationary Cosmology".

CH is supported by the US Department of Energy under contract DE-FG03-02-ER40701, the National Science Foundation under contract AST-0807337, and the Alfred P Sloan Foundation.

Funding for the Sloan Digital Sky Survey (SDSS) and SDSS-II has been provided by the Alfred P Sloan Foundation, the Participating Institutions, the National Science Foundation, the US Department of Energy, the National Aeronautics and Space Administration, the Japanese Monbukagakusho, the Max Planck Society, and the Higher Education Funding Council for England. The SDSS Web site is http://www.sdss.org/.

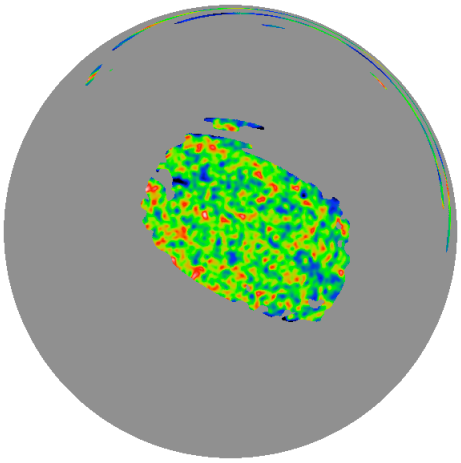

Figure 5.6: The QSO density of the entire RQCat UVX sample. The figure format is similar to Fig. 5.2, except that the color scale is twice as small.

The SDSS is managed by the Astrophysical Research Consortium (ARC) for the Participating Institutions. The Participating Institutions are the American Museum of Natural History, Astrophysical Institute Potsdam, University of Basel, University of Cambridge, Case Western Reserve University, The University of Chicago, Drexel University, Fermilab, the Institute for Advanced Study, the Japan Participation Group, The Johns Hopkins University, the Joint Institute for Nuclear Astrophysics, the Kavli Institute for Particle Astrophysics and Cosmology, the Korean Scientist Group, the Chinese Academy of Sciences (LAMOST), Los Alamos National Laboratory, the Max Planck Institute for Astronomy (MPIA), the Max Planck Institute for Astrophysics (MPA), New Mexico State University, Ohio State University, University of Pittsburgh, University of Portsmouth, Princeton University, the United States Naval Observatory, and the University of Washington.

Appendix A

Generalization to a Temperature-Polarization Map

For most experiments, the sensitivity to departures from statistical isotropy will come primarily from either the temperature or the polarization. Considering both in tandem will provide some improvement in the result, but given the temperature-polarization cross-correlation, this improvement will be weaker than what would be obtained by simply adding the two results in quadrature.

Still, to be complete, we include expressions for theory and estimators for a combined temperature-polarization map. Assuming only primordial density perturbations contribute to the temperature-polarization map, a map of the sky will now provide the E-mode polarization $E(\hat{\mathbf{n}})$, constructed in the usual fashion [72, 73] from the measured Stokes parameters $Q(\hat{\mathbf{n}})$ and $U(\hat{\mathbf{n}})$, in addition to the temperature $T(\hat{\mathbf{n}})$. The map can be written in terms of spherical-harmonic coefficients $a^{\rm X}_{lm}$, for $\mathrm{X} = \{\mathrm{T}, \mathrm{E}\}$, and Eq. (3.6) is generalized to

$$\left\langle a^{\rm X}_{lm} a^{\rm X',*}_{l'm'} \right\rangle = \delta_{ll'}\delta_{mm'} C_l^{\rm XX'} + \sum_{LM} \xi^{LM}_{lml'm'} D_{ll'}^{LM,\rm XX'}. \tag{A.1}$$

The $C_l^{\rm XX'}$s and $D_{ll'}^{LM,\rm XX'}$s are obtained as in Eqs. (3.7) and (3.8) by replacing the $\Theta_l(k)\Theta_{l'}(k)$ factors in the integrands of those equations by $\Theta^{\rm X}_l(k)\Theta^{\rm X'}_l(k)$, where these are obtained from Eq. (3.5) by replacing $T(\hat{\mathbf{n}})$ by $X(\hat{\mathbf{n}})$. Note that for TE and $l \neq l'$, $D_{ll'}^{LM,\rm XX'} \neq D_{l'l}^{LM,\rm XX'}$. This will affect the equations below for the minimum-variance estimator.

We now have a set of three power multipole moments $b_{LM}^{\rm XX'}$, obtained from Eq. (3.11) by replacing $\left\langle T^2 \right\rangle$ by $\langle XX' \rangle$, which is itself obtained from Eq. (3.12) by using $\left\langle a^{\rm X}_{lm} a^{\rm X',*}_{l'm'} \right\rangle$ for the expectation value therein. The expression for the $b_{LM}^{\rm XX'}$ is the same as Eq. (3.14) using $D_{ll'}^{LM,\rm XX'}$ there.

The power-multipole-moment estimators $\widehat{b}_{LM}^{\rm XX',map}$ are as in Eq. (3.15) with $[T^{\rm map}(\hat{\mathbf{n}})]^2$ replaced by $[X^{\rm map}(\hat{\mathbf{n}}) X'^{\rm map}(\hat{\mathbf{n}})]$. Things get a bit trickier, though, when we calculate the variances, as the estimators for different XX′ will now be correlated, although still uncorrelated for different LM. The variance in Eq. (3.16) is now promoted to a 3×3 matrix $\Xi^{LM}_{\rm AA'}$, for $\{\mathrm{A}, \mathrm{A}'\} = \{\mathrm{TT}, \mathrm{EE}, \mathrm{TE}\}$. For

$\{\mathrm{A\,A'}\} = \mathrm{XX'} = \{\mathrm{TT, EE}\}$, $\Xi^{LM}_{\mathrm{AA'}}$ is given by Eq. (4.13) with $C^{\mathrm{map}}_{l_1} C^{\mathrm{map}}_{l_2}$ replaced by $C^{\mathrm{A,map}}_{l_1} C^{\mathrm{A',map}}_{l_2}$. For the diagonal TE-TE term,

$$\Xi^{LM}_{\mathrm{TE,TE}} = \sum_{ll'} G^L_{ll'} [C^{\mathrm{TT,map}}_l C^{\mathrm{EE,map}}_{l'} + C^{\mathrm{TE,map}}_l C^{\mathrm{TE,map}}_{l'}], \tag{A.2}$$

and for the off-diagonal XX-XX$'$ terms,

$$\Xi^{LM}_{\mathrm{XX,XX'}} = 2 \sum_{ll'} G^L_{ll'} C^{\mathrm{XX,map}}_l C^{\mathrm{XX',map}}_{l'}. \tag{A.3}$$

Eq. (3.18) for the standard error with which a constant g_{LM} can be recovered with the power multipole moments is then replaced by [74, 72, 73]

$$\frac{1}{\sigma^2_{g_{LM}}} = \sum_{\mathrm{AA'}} \frac{\partial b^A_{LM}}{\partial g_{LM}} [(\Xi^{LM})^{-1}]_{\mathrm{AA'}} \frac{\partial b^{\mathrm{A'}*}_{LM}}{\partial g_{LM}}. \tag{A.4}$$

This is the equation used to obtain the "total" results listed in Table 3.1 for the power multipole moment.

The minimum-variance estimator for g_{LM} and its variance are similarly generalized. The estimators $\widehat{D}^{LM,\mathrm{A,map}}_{ll'}$ are still uncorrelated for different ll' pairs and different LM, but they are now correlated for different A. The main subtlety is that since $D^{LM,\mathrm{TE}}_{ll'} \neq D^{LM,\mathrm{TE}}_{l'l}$, we must be careful to keep track of all TE modes for $l \neq l'$. This will require that we split the sum in the generalization of Eq. (3.24) into two sums: the first over $l = l'$, and the second over $l' > l$. (Actually, the sum can in fact be written over all ll', but at the cost of much uglier algebraic expressions.)

For $l' = l$, there are now three (TT, EE, and TE) estimators to replace that in Eq. (3.19), and for $l' > l$, there are now four (TT, EE, TE, and ET) estimators to replace that in Eq. (3.19). For all ll', the estimators are as in Eq. (3.19), replacing each a^{map}_{lm} and C^{map}_l by the appropriate $a^{\mathrm{X,map}}_{lm}$ and $C^{\mathrm{XX',map}}_l$, respectively. The estimator for each ll', obtained after summing over all mm', is the same as in Eq. (3.21). For $l = l'$, the variances $\left\langle \left(\widehat{D}^{LM,\mathrm{A,map}}_{ll'} \right)^2 \right\rangle$ are now promoted to a 3×3 covariance matrix. and for $l' > l$, they are promoted to a 4×4 covariance matrix. In both cases, the covariance matrix can be written as

$$\mathcal{C}^{ll'}_{\mathrm{AA'}} \equiv \frac{G^L_{ll'}}{(1 + \delta_{ll'})} \left\langle \widehat{D}^{LM,\mathrm{A,map}}_{ll'} \widehat{D}^{LM,\mathrm{A',map}}_{ll'} \right\rangle. \tag{A.5}$$

For any ll' pair, the diagonal entries, for $\mathrm{A} = \{\mathrm{TT, EE}\}$, are $\mathcal{C}^{ll'}_{\mathrm{AA}} = C^{\mathrm{A,map}}_l C^{\mathrm{A,map}}_{l'}$, and the TT-EE off-diagonal entry is $\mathcal{C}^{ll'}_{\mathrm{TT,EE}} = C^{\mathrm{TE,map}}_l C^{\mathrm{TE,map}}_{l'}$. For $l = l'$, the diagonal TE-TE entry is

$$\mathcal{C}^{ll'}_{\mathrm{TE,TE}} = \left[C^{\mathrm{TT,map}}_l C^{\mathrm{EE,map}}_l + \left(C^{\mathrm{TE,map}}_l \right)^2 \right] / 2. \tag{A.6}$$

For $l' > l$, we have $\mathcal{C}^{ll'}_{\rm TE,TE} = C_l^{\rm TT} C_{l'}^{\rm EE}$, $\mathcal{C}^{ll'}_{\rm ET,ET} = C_{l'}^{\rm TT} C_l^{\rm EE}$, and $\mathcal{C}^{ll'}_{\rm TE,ET} = C_l^{\rm TE} C_{l'}^{\rm TE}$. For any ll', we have $\mathcal{C}^{ll'}_{\rm TT,TE} = C_l^{\rm TT} C_{l'}^{\rm TE}$ and $\mathcal{C}^{ll'}_{\rm EE,TE} = C_{l'}^{\rm EE} C_l^{\rm TE}$. For $l' > l$, we also have $\mathcal{C}^{ll'}_{\rm TT,ET} = C_{l'}^{\rm TT} C_l^{\rm TE}$ and $\mathcal{C}^{ll'}_{\rm EE,ET} = C_l^{\rm EE} C_{l'}^{\rm TE}$.

The generalization of Eq. (3.24) is then

$$\begin{aligned} \frac{1}{\sigma^2_{g_{LM}}} &= \frac{1}{2} \sum_l G^L_{ll} \sum_{AA'} C_l^{\rm A} C_l^{\rm A'} (W_l)^4 \left[\left(\mathcal{C}^{ll} \right)^{-1} \right]_{\rm AA'} \\ &+ \sum_{l'>l} G^L_{ll'} \sum_{\rm AA'} F^{\rm A}_{ll'} F^{\rm A'}_{ll'} (W_l W_{l'})^2 \left[\left(\mathcal{C}^{ll'} \right)^{-1} \right]_{\rm AA'} , \end{aligned} \tag{A.7}$$

where the matrix inversion is in the 3×3 AA$'$ space in the first sum and in the 4×4 AA$'$ space in the second sum. We use Eq. (A.7) to evaluate the standard errors for the "total" minimum-variance estimators listed in Table 3.1.

Appendix B

Real $l = 2$ Spherical Harmonics

In Eq. 4.3 we introduce our convention for the real spherical harmonics $R_{LM}(\theta, \phi)$. To clarify the functional form of R_{LM}, we list the harmonics for $L = 2$. These are given by

$$\begin{aligned} R_{22}(\theta,\phi) &= \sqrt{\frac{15}{16\pi}}\sin^2\theta\cos(2\phi) \\ R_{21}(\theta,\phi) &= -\sqrt{\frac{15}{4\pi}}\cos\theta\sin\theta\cos\phi \\ R_{20}(\theta,\phi) &= \sqrt{\frac{5}{16\pi}}\left(3\cos^2\theta - 1\right) \\ R_{2,-1}(\theta,\phi) &= \sqrt{\frac{15}{4\pi}}\cos\theta\sin\theta\sin\phi \\ R_{2,-2}(\theta,\phi) &= -\sqrt{\frac{15}{16\pi}}\sin^2\theta\sin(2\phi)\,. \end{aligned} \tag{B.1}$$

Appendix C

Expressions for the Anisotropy Coefficient

In Ref. [78], Pullen and Kamionkowski introduced an anisotropy coefficient $\xi^{LM}_{lml'm'}$ that appears in the correlation function, given by

$$\begin{aligned} \xi^{LM}_{lml'm'} &= \int d\hat{\mathbf{k}}\, Y^*_{lm}(\hat{\mathbf{k}}) Y_{l'm'}(\hat{\mathbf{k}}) Y_{LM}(\hat{\mathbf{k}}) \\ &= (-1)^m \left(G^L_{ll'}\right)^{1/2} C^{LM}_{lml',-m'}\,, \end{aligned} \tag{C.1}$$

where $C^{LM}_{lml'm'}$ are Clebsch-Gordan coefficients, and

$$G^L_{ll'} \equiv \frac{(2l+1)(2l'+1)}{4\pi(2L+1)} \left(C^{L0}_{l0l'0}\right)^2. \tag{C.2}$$

However, since we use real spherical harmonics (given by Eq. 4.3) in our analysis as opposed to complex spherical harmonics, we introduce the anisotropy coefficient $X^{LM}_{lml'm'}$ given by Eq. (4.13). We choose to write $X^{LM}_{lml'm'}$ in terms of Wigner 3j symbols. Due to the piecewise nature of the real spherical harmonics, $X^{LM}_{lml'm'}$ will have different expressions for different values of m, m', and M. After much algebra, we can find the expressions for $X^{LM}_{lml'm'}$ in terms of Wigner 3j symbols (written in matrix form) and $P_{ll'L}$, given by

$$P_{ll'L} = \sqrt{\frac{(2l+1)(2l'+1)(2L+1)}{4\pi}} \begin{pmatrix} l & l' & L \\ 0 & 0 & 0 \end{pmatrix}, \tag{C.3}$$

which is nonzero only for $l + l' + L$ even. The expression for $M = 0$ is given by

$$X^{L0}_{lml'm'} = (-1)^m P_{ll'L} \begin{pmatrix} l & l' & L \\ m & -m & 0 \end{pmatrix} \delta_{mm'}. \tag{C.4}$$

The expressions for $M \neq 0$ can be obtained similarly, e.g.,

$$\begin{aligned} X^{LM}_{lml'm'} &= P_{ll'L}\left[\frac{(-1)^{m'}}{\sqrt{2}}\begin{pmatrix} l & l' & L \\ m & -(m+M) & M \end{pmatrix}\delta_{m',m+M}\right. \\ &\left. +\frac{(-1)^{m}}{\sqrt{2}}\begin{pmatrix} l & l' & L \\ m & M-m & -M \end{pmatrix}\delta_{m',m-M}\right], \end{aligned} \tag{C.5}$$

for $m > M > 0$; the other equations are similar but will be omitted for brevity.

Appendix D

Effective Scale for Quadrupole Asymmetry Analyses

In Ref. [36], Groeneboom et al. calculated a quadrupole asymmetry in the matter power spectrum by analysis of the CMB up to multipoles of $l = 400$. In this appendix, we derive the effective wavenumber $k_{\rm eff}$ of this CMB measurement, as well as $k_{\rm eff}$ for our measurement using the LRG sample.

To find $k_{\rm eff}$ for the CMB analysis, we first find an estimator for g_{2M} in terms of measurable quantities in Fourier space.[1] This calculation has been done previously in Chapter 3. By using Eq. 3.23 in that chapter, we can construct the minimum-variance estimator for g_{2M} given by

$$\widehat{g}_{2M} = \frac{\sum_{ll'} \widehat{g}_{2M,ll'} Q_{ll'2} (F_{ll'}^{\rm map})^2 / (C_l^{\rm map} C_{l'}^{\rm map})}{\sum_{ll'} Q_{ll'2} (F_{ll'}^{\rm map})^2 / (C_l^{\rm map} C_{l'}^{\rm map})} \,, \tag{D.1}$$

where $C_l^{\rm map} = |W_l|^2 C_l + C_l^n$ is the map's power spectrum, $W_l = e^{-l^2\sigma_b^2/2}$ is the beam window function, $F_{ll'}^{\rm map} = W_l W_{l'} F_{ll'}$, $Q_{ll'2} = \sum_{mm'} (X^{2M}_{lml'm'})^2 = (P_{ll'2})^2/5$, and $\widehat{g}_{2M,ll'}$ is the estimator of g_{2M}. We can construct an estimator for each ll' pair with $\widehat{g}_{2M,ll'} = \widehat{D}^{2M}_{ll'}/F_{ll'}$, where $\widehat{D}^{2M}_{ll'}$ is an estimator constructed from the measured a_{lm}s. By approximating for large l

$$\begin{pmatrix} l & l & 2 \\ 0 & 0 & 0 \end{pmatrix}^2 \simeq \frac{1}{8l} \text{ and } \begin{pmatrix} l & l \pm 2 & 2 \\ 0 & 0 & 0 \end{pmatrix}^2 \simeq \frac{3}{16l} \,, \tag{D.2}$$

using Eq. (8.32) of Ref. [104], along with $F_{ll} = C_l$ and $F_{l(l\pm2)} \simeq -0.5 C_l$ (for temperature perturbations), we have

$$\widehat{g}_{2M} \simeq \frac{\sum_l l T_l [\frac{1}{8\pi} \widehat{g}_{2M,ll} + \frac{3}{64\pi} (\widehat{g}_{2M,l(l+2)} + \widehat{g}_{2M,l(l-2)})]}{\frac{7}{32\pi} \sum_l l T_l} \,, \tag{D.3}$$

where $T_l = [1 + C_l^n/(W_l^2 C_l)]^{-2}$.

[1] Although Ref. [36] parametrized the quadrupole asymmetry in terms of g_*, not g_{2M}, this should not affect the effective wavenumber of the measurement.

If the expectation value of this estimator is taken, then $\widehat{g}_{2M,ll'}$ is replaced with $\langle\widehat{g}_{2M,ll'}\rangle = D^{2M}_{ll'}/F_{ll'}$. This estimator was constructed with the assumption that g_{2M} is scale-invariant, in which case $\langle\widehat{g}_{2M,ll'}\rangle = g_{2M}$ and $\langle\widehat{g}_{2M}\rangle$ does give the true g_{2M}. However, if g_{2M} does vary with scale, then it has to be included inside the integral for $D^{2M}_{ll'}$, and the estimator's expectation value must be taken as g_{2M} at $k = k_{\rm eff}$. We find this scale by giving $g_{2M}(k)$ a functional form, which we use to find $\langle\widehat{g}_{2M}\rangle = g_{2M}(k_{\rm eff})$.

We begin with the expectation value of $\widehat{g}_{2M,ll'}$, given by

$$\langle\widehat{g}_{2M,ll'}\rangle = \frac{\int g_{2M}(k)\bar{P}_\zeta(k)\Theta_l(k)\Theta_{l'}(k)k^2dk}{\int \bar{P}_\zeta(k)\Theta_l(k)\Theta_{l'}(k)k^2dk}\,, \tag{D.4}$$

where $\bar{P}_\zeta$ is the curvature power spectrum and $\Theta_l(k)$ is the transfer function of the CMB temperature fluctuations. Typically, in inflationary models that break scale invariance, g_{2M} will vary smoothly with $\ln k$, and we can write

$$g_{2M}(k) = B_1 + B_2\ln(k/k_*)\,, \tag{D.5}$$

where k_* is the (arbitrary) pivot wavenumber such that $\bar{P}_\zeta(k_*)$ is constant even when the scalar spectral index n_s is varied. We then insert this expression into Eq. D.4 and find

$$\langle\widehat{g}_{2M,ll'}\rangle = B_1 + B_2\frac{\int \ln(k/k_*)\bar{P}_\zeta(k)\Theta_l(k)\Theta_{l'}(k)k^2dk}{\int \bar{P}_\zeta(k)\Theta_l(k)\Theta_{l'}(k)k^2dk}\,. \tag{D.6}$$

The denominator in the second term is just $F_{ll'}$. The numerator can be rewritten by using $\bar{P}_\zeta(k) \propto (k/k_*)^{n_s}$ such that

$$\langle\widehat{g}_{2M,ll'}\rangle = B_1 + B_2\frac{\partial \ln F_{ll'}}{\partial n_s}\,. \tag{D.7}$$

We then insert this expression into the expectation value of Eq. D.3 and, by using $\langle g_{2M}\rangle = B_1 + B_2\ln(k_{\rm eff}/k_*)$, we find

$$\ln(k_{\rm eff}/k_*) = \frac{\sum_l lT_l(\partial\ln C_l/\partial n_s)}{\sum_l lT_l}\,. \tag{D.8}$$

We can find the derivative in this expression numerically by using the finite difference method with a two-sided derivative centered at the fiducial value $n_s = 1$ with endpoints $n_s^\pm = 1 \pm 0.025$.

We use the fiducial cosmological parameters (except for n_s) to calculate C_l using CAMB [105], along with WMAP's instrumental parameters $\sigma_T = 1.09\times10^{-5}$ and $\theta_{\rm fwhm} = 21'$, specifically in the V band. These parameters give us T_ls in the range of $T_2 = 0.99994$ to $T_{400} = 0.17$. We select the pivot wavenumber $k_* = 0.002$ Mpc^{-1}. This gives us $k_{\rm eff}^{\rm CMB} = 0.0204$ Mpc^{-1}.

Finding $k_{\rm eff}$ for the LRG analysis is similar except we include measurements of perturbations at 8 redshift slices instead of only one last-scattering surface. By making the necessary changes for a galaxy survey analysis, including $F^i_{g,l(l\pm2)} \simeq -C^i_{g,l}$ (i denotes the redshift slice), we find

$$\widehat{g}_{2M} \simeq \frac{\sum_{l,i} lT^i_{g,l}[\frac{1}{8\pi}\widehat{g}^i_{2M,ll} + \frac{3}{16\pi}(\widehat{g}^i_{2M,l(l+2)} + \widehat{g}^i_{2M,l(l-2)})]}{\frac{1}{2\pi}\sum_{l,i} lT^i_{g,l}}\,, \tag{D.9}$$

where $T^i_{g,l} = [1 + C^{i,n}_{g,l}/C^i_{g,l}]^{-2}$, $C^{n,i}_{g,l} = \Delta\Omega/\overline{n}_i$, $\Delta\Omega$ is the pixel size, and $\overline{n}_i$ is the average number of galaxies per pixel. The expectation value of the estimator $\widehat{g}^i_{2M,ll'}$ is given by

$$\left\langle \widehat{g}^i_{2M,ll'} \right\rangle = \frac{\int g_{2M}(k)\bar{P}_g(k)W^i_l(k)W^i_{l'}(k)k^2dk}{\int \bar{P}(k)W^i_l(k)W^i_{l'}(k)k^2dk}\,, \tag{D.10}$$

where $W^i_l(k)$ is the (survey) window function. $g_{2M}(k)$ again varies smoothly with $\ln k$, which allows us to write

$$g_{2M}(k) = D_1 + D_2 \ln k\,. \tag{D.11}$$

This parameterization gives us

$$\left\langle \widehat{g}^i_{2M,ll'} \right\rangle = D_1 + D_2 \frac{\int \ln k\bar{P}_g(k)W^i_l(k)W^i_{l'}(k)k^2dk}{\int \bar{P}_g(k)W^i_l(k)W^i_{l'}(k)k^2dk}\,. \tag{D.12}$$

The denominator in the second term is just $F^i_{g,ll'}$, and the numerator can be calculated directly. Inserting this into the expectation value of Eq. D.9, which equals $D_1 + D_2\ln(k_{\rm eff})$, we find $k^{\rm LRG}_{\rm eff} = 0.151$ Mpc^{-1}.

Appendix E

QSO Redshift Distributions

In Ref. [94], Ho et al. construct photometric redshift distributions $f_i(z)$ for QSOs using spectroscopic data from 2SLAQ [134]. These redshift distributions determine how the matter overdensity $\delta(\mathbf{x})$ relates to the QSO overdensity $\delta_q(\hat{\mathbf{n}})$

$$\delta_q(\hat{\mathbf{n}}) = \int_0^\infty f(z)\delta[\hat{\mathbf{n}}, \chi(z)]dz\,. \tag{E.1}$$

We refer the reader to Ref. [94] for the theory behind this method, and we describe our method which is similar to and follows from Ref. [94].

The expression for $f(z)$ is given as

$$f_i(z) = b(z)\Pi(z) + \int_z^\infty W(z, z')[\alpha(z') - 1]\Pi_i(z')dz'\,, \tag{E.2}$$

where $b(z)$ is the linear bias as a function of redshift, $\chi(z) = \int_0^z c/H(z')dz'$ is the comoving radial distance, and $\Pi_i(z)$ is the probability distribution for the QSO redshifts. The second term in Eq. E.2 is due to magnification bias, which becomes important for large redshifts, with the lensing window function $W(z, z')$ given for a flat universe by

$$W(z, z') = \frac{3}{2}\Omega_m H_0^2 \frac{1+z}{cH(z)}\chi^2(z)\left[\frac{1}{\chi(z)} - \frac{1}{\chi(z')}\right], \tag{E.3}$$

and $\alpha(z)$ being the logarithmic slope of the number counts of QSOs as a function of flux: $N(> F) \propto F^{-\alpha}$.

Since the photometric redshifts of QSOs are difficult to determine, we must rely on spectroscopic data to compose redshift distributions. Specifically, we use spectroscopic QSOs (spectro-QSOs) from an area with high spectroscopic coverage to construct a preliminary probability distribution $\Pi_{i,\mathrm{prelim}}$ and $\alpha(z)$. We use spectroscopic data from the 2SLAQ survey, which contains 8389 spectro-QSOs over its total region of view. We restrict ourselves to using spectroscopic data from five rectangles on the sky with declination range $-01°00'36''$–$00°35'24''$ and right ascension ranges 137°–143°, 150°–

Table E.1: Properties of $\Pi_{i,\mathrm{prelim}}$ for the 3 QSO redshift slices; N_q is the number of spectro-QSOs (matched with a photo-QSO in RQCat) in the photometric redshift slice, σ is the slice's kernel width, and α is the logarithmic slope of number counts as a function of flux.

Label	N_q	σ	α
z01	599	0.08	0.48
z02	779	0.10	0.63
z03	236	0.06	0.64

168°, 185°–193°, 197°–214°, and 218°–230°, the same as those used in Ref. [94]. These rectangles in particular have high spectroscopic coverage and contain 5383 QSOs. Since we also need photo-zs for the QSOs to construct probability densities, we only use QSOs that have matches in the RQCat, decreasing the number of objects to 3443.

We calculate $\Pi_{i,\mathrm{prelim}}(z)$ for each photometric redshift slice using a kernel density estimator of the form

$$\Pi_{i,\mathrm{prelim}}(z) = \frac{1}{N_q}\sum_{k=1}^{N_q}\frac{1}{\sqrt{2\pi}\sigma}e^{-(z-z_k)^2/2\sigma^2}\,, \tag{E.4}$$

where N_q is the number of spectro-QSOs (matched with a photo-QSO in RQCat) in the photometric redshift slice, z_k is the spectro-z of the kth matched QSO, and σ is the slice's kernel width. σ is chosen to be smaller than any real features in $\Pi_{i,\mathrm{prelim}}$ yet large enough to smooth out shot noise. Table E.1 lists N_q and σ for each redshift slice, and Fig. E.1 shows a plot of $\Pi_{i,\mathrm{prelim}}$ for each slice. We also calculate α, the logarithmic slope of the number count of QSOs in terms of flux, by creating a histogram of number counts in terms of the PSF magnitude in the g-band around $g = 21$ and calculating the *actual* slope around this value. This value for each redshift slice is also listed in Table E.1.

The expression for $f_i(z)$ in Eq. E.2 requires the true probability distribution $\Pi_i(z)$. However, since $\alpha - 1$ is small, the second term is subdominant to the first and we can substitute $\Pi_i(z)$ with $\Pi_{i,\mathrm{prelim}}(z)$ in the second term, giving us

$$f_i(z) \simeq b(z)\Pi_i(z) + \int_z^\infty W(z,z')[\alpha(z')-1]\Pi_{i,\mathrm{prelim}}(z')dz'\,. \tag{E.5}$$

$\Pi_i(z)$ cannot be similarly substituted for in the first term, so we must estimate $b(z)\Pi_i(z)$ using LSS data. We estimate $b(z)D(z)$ as nearly constant, writing

$$b(z)\Pi_i(z)D(z) = A_i\Pi_{i,\mathrm{prelim}}\,, \tag{E.6}$$

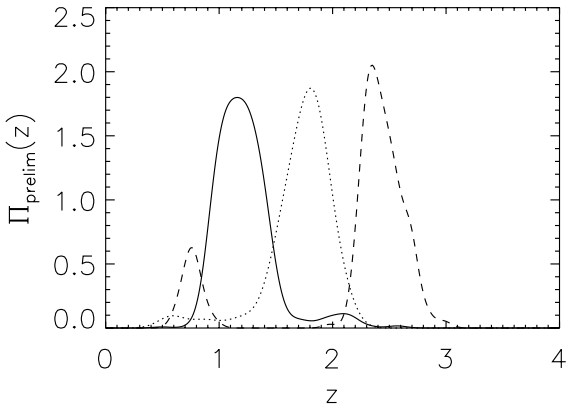

Figure E.1: The preliminary redshift distributions for the QSO photometric redshift slices z01 (solid), z02 (dotted), and z03 (dashed).

where A_i is a constant. Generally, A_i would be a piecewise function of z that varies in however many places it needs to for A_i to be estimated precisely; however, we were able to estimate A_i as a constant function with very small uncertainties.

We estimate A_i in each redshift slice by constraining its effect on the QSO clustering. We begin by estimating the QSO correlation function $w_i(\theta)$ in each redshift slice using the method presented in Landy and Szalay [135]. Specifically, we use the estimator $\hat{w}_4(\theta)$ along with its variance given in Ref. [135], given by

$$\hat{w}_4(\theta) = \frac{DD(\theta) - 2DR(\theta) + RR(\theta)}{RR(\theta)}\,, \tag{E.7}$$

where $DD(\theta)$, $DR(\theta)$, and $RR(\theta)$ are properly normalized histograms of the number of data-data pairs, data-random pairs, and random-random pairs, respectively, binned in terms of angular separation. We use the following expression for the Poisson uncertainty in our estimator

$$\mathrm{var}[\hat{w}_4] = \frac{2}{n(n-1)RR}\,, \tag{E.8}$$

where n is the number of random data points used to calculate $RR(\theta)$. To this we add a similar expression for Poisson noise due to the data to get the total variance for $w_i(\theta)$. Note that for these stochastic calculations we use 25 simulations with the number of random points equal to twice the number of data points. We calculate $w_i(\theta)$ in 10 logarithmic bins of equal (logarithmic) size in the range $0.3^\circ < \theta < 6^\circ$. We use this angular range to avoid nonlinearities at smaller angles and potential effects of non-Gaussianity at large angles. We compare this estimate of $w_i(\theta)$ to the expression

$$w(\theta) \quad = \quad \int_0^\infty dk\, kP(k)F(k,\theta)$$

Table E.2: Estimates for QSO redshift distribution amplitude A_i for each redshift slice.

Label	A_i
z01	1.77±0.165
z02	1.88±0.145
z03	2.13±0.869

$$F(k,\theta) \quad = \quad k\sum_{l=1}^{\infty}\left(\frac{2l+1}{2\pi^2}\right)P_l(\cos\theta)[W_l(k)]^2\,, \tag{E.9}$$

where we substitute Eq. E.6 for the first term in Eq. E.5 to calculate $W_l(k)$ in terms of A. Note that we include the effect of redshift-space distortions in $W_l(k)$. For calculating $F(k,\theta)$ we use the Limber approximation for $k > 0.0155$ Mpc^{-1} by converting the sum to an integral[1], replacing $P_l(\cos\theta) \rightarrow J_0(l\theta)$, and replacing $W_l(k) \rightarrow \sqrt{\pi/2l}f(l/k)/k$. We can write $w_i(\theta)$ as a sum of terms linear and quadratic in A_i, which allows us to fit for this parameter for each redshift slice. We also add to this model a constant term B_i due to systematics effects for which we also fit[2]. In Table E.2, we list estimates for the A_is, from which we derive the redshift distributions $f_i(z)$ shown in Fig. 5.1.

[1]We verified that for $k > 0.017$ Mpc^{-1} the summand vanishes for $l < 40$, which removes all terms over which the Limber approximation is not valid.

[2]Note that we did not include B_i for redshift slice z03 because it caused A_i to not be constrainable.

Bibliography

[1] G. Jungman, M. Kamionkowski, and K. Griest, Phys. Rept. **267**, 195 (1996), hep-ph/9506380.

[2] L. Bergstrom, Rept. Prog. Phys. **63**, 793 (2000), hep-ph/0002126.

[3] G. Bertone, D. Hooper, and J. Silk, Phys. Rept. **405**, 279 (2005), hep-ph/0404175.

[4] M. Milgrom, Astrophys. J. **270** 365 (1983).

[5] J. Bekenstein, Phys. Rev. D **70** 083509 (2004) [arXiv:astro-ph/0403694].

[6] J. Brownstein and J. Moffat, Mon. Not. Roy. Astron. Soc. **367** 527 (2006) [arXiv:astro-ph/0507222].

[7] D. Clowe *et al.*, Astrophys. J. **648** L109 (2006) [arXiv:astro-ph/0608407].

[8] H. E. Haber and G. L. Kane, Phys. Rept. **117**, 75 (1985).

[9] A. Bottino, F. Donato, N. Fornengo, and S. Scopel, Phys. Rev. **D70**, 015005 (2004), hep-ph/0401186.

[10] J. F. Gunion, D. Hooper, and B. McElrath, Phys. Rev. **D73**, 015011 (2006), hep-ph/0509024.

[11] F. Ferrer, L. M. Krauss, and S. Profumo, Phys. Rev. **D74**, 115007 (2006), hep-ph/0609257.

[12] L. Bergstrom and H. Snellman, Phys. Rev. **D37**, 3737 (1988).

[13] fermi.gsfc.nasa.gov.

[14] D. J. Thompson, D. L. Bertsch, C. E. Fichtel, R. C. Hartman, R. Hofstadter, E. B. Hughes, S. D. Hunter, B. W. Hughlock, G. Kanbach, D. A. Kniffen, et al., Astrophys. J. Suppl. **86**, 629 (1993).

[15] A. de Oliveira-Costa, M. Tegmark, M. Zaldarriaga and A. Hamilton, Phys. Rev. D **69**, 063516 (2004) [arXiv:astro-ph/0307282]; C. J. Copi, D. Huterer and G. D. Starkman, Phys. Rev. D **70**, 043515 (2004) [arXiv:astro-ph/0310511]; D. J. Schwarz, G. D. Starkman, D. Huterer and C. J. Copi, Phys. Rev. Lett. **93**, 221301 (2004) [arXiv:astro-ph/0403353]; S. Prunet,

J. P. Uzan, F. Bernardeau and T. Brunier, Phys. Rev. D **71**, 083508 (2005) [arXiv:astro-ph/0406364]; H. K. Eriksen, A. J. Banday, K. M. Gorski and P. B. Lilje, Astrophys. J. **622**, 58 (2005) [arXiv:astro-ph/0407271]; K. Land and J. Magueijo, Phys. Rev. Lett. **95**, 071301 (2005) [arXiv:astro-ph/0502237]; T. R. Jaffe, A. J. Banday, H. K. Eriksen, K. M. Gorski and F. K. Hansen, Astrophys. J. **629**, L1 (2005) [arXiv:astro-ph/0503213]; C. J. Copi, D. Huterer, D. J. Schwarz and G. D. Starkman, Mon. Not. Roy. Astron. Soc. **367**, 79 (2006) [arXiv:astro-ph/0508047]; K. Land and J. Magueijo, Mon. Not. Roy. Astron. Soc. **367**, 1714 (2006) [arXiv:astro-ph/0509752]; A. Bernui, T. Villela, C. A. Wuensche, R. Leonardi and I. Ferreira, Astron. Astrophys. **454**, 409 (2006) [arXiv:astro-ph/0601593]; L. R. Abramo, A. Bernui, I. S. Ferreira, T. Villela and C. A. Wuensche, Phys. Rev. D **74**, 063506 (2006) [arXiv:astro-ph/0604346]; J. Magueijo and R. D. Sorkin, Mon. Not. Roy. Astron. Soc. Lett. **377**, L39 (2007) [arXiv:astro-ph/0604410]; C. G. Park, C. Park and J. R. I. Gott, Astrophys. J. **660**, 959 (2007) [arXiv:astro-ph/0608129]; D. Huterer, New Astron. Rev. **50**, 868 (2006) [arXiv:astro-ph/0608318]; P. Vielva, Y. Wiaux, E. Martinez-Gonzalez and P. Vandergheynst, New Astron. Rev. **50**, 880 (2006) [arXiv:astro-ph/0609147]; K. Land and J. Magueijo, Mon. Not. Roy. Astron. Soc. **378**, 153 (2007) [arXiv:astro-ph/0611518]; C. Gordon, W. Hu, D. Huterer and T. Crawford, Phys. Rev. D **72**, 103002 (2005) [arXiv:astro-ph/0509301]; J. G. Cresswell, A. R. Liddle, P. Mukherjee and A. Riazuelo, Phys. Rev. D **73**, 041302 (2006) [arXiv:astro-ph/0512017]. S. H. S. Alexander, arXiv:hep-th/0601034.

[16] H. K. Eriksen, F. K. Hansen, A. J. Banday, K. M. Gorski and P. B. Lilje, Astrophys. J. **605**, 14 (2004) [Erratum-ibid. **609**, 1198 (2004)] [arXiv:astro-ph/0307507].

[17] F. K. Hansen, A. J. Banday and K. M. Gorski, Mon. Not. Roy. Astron. Soc. **354** 641 (2004) arXiv:astro-ph/0404206.

[18] H. K. Eriksen, A. J. Banday, K. M. Gorski, F. K. Hansen and P. B. Lilje, Astrophys. J. **660**, L81 (2007) [arXiv:astro-ph/0701089].

[19] G. V. Chibisov and Y. V. Shtanov, Sov. Phys. JETP **69**, 17 (1989).

[20] G. V. Chibisov and Y. V. Shtanov, Int. J. Mod. Phys. **A5**, 2625 (1990).

[21] A. Berera, R. V. Buniy and T. W. Kephart, JCAP **0410**, 016 (2004) [arXiv:hep-ph/0311233].

[22] E. P. Donoghue and J. F. Donoghue, Phys. Rev. D **71**, 043002 (2005) [arXiv:astro-ph/0411237].

[23] R. V. Buniy, A. Berera and T. W. Kephart, Phys. Rev. D **73**, 063529 (2006) [arXiv:hep-th/0511115].

[24] L. Ackerman, S. M. Carroll and M. B. Wise, Phys. Rev. D **75**, 083502 (2007) [arXiv:astro-ph/0701357].

[25] A. E. Gumrukcuoglu, C. R. Contaldi and M. Peloso, JCAP **711** 5 (2007) arXiv:0707.4179 [astro-ph].

[26] C. Armendariz-Picon, JCAP **709** 14 (2007) arXiv:0705.1167 [astro-ph].

[27] J. F. Donoghue, K. Dutta and A. Ross, Phys. Rev. D **80** 023526 (2009) arXiv:astro-ph/0703455.

[28] T. S. Pereira, C. Pitrou and J.-P. Uzan, J. Cosmol. Astropart. Phys. **09**, 006 (2007).

[29] R. A. Battye and A. Moss, Phys. Rev. D **74**, 041301 (2006) [arXiv:astro-ph/0602377].

[30] T. Koivisto and D. F. Mota, Astrophys. J **679** 1 (2008) arXiv:0707.0279 [astro-ph].

[31] C. L. Bennett *et al.*, Astrophys. J. Suppl. **192** 17 (2011) arXiv:1001.4758 [astro-ph.CO].

[32] `map.gsfc.nasa.gov`

[33] [Planck Collaboration], arXiv:astro-ph/0604069.

[34] B. Himmetoglu, C. Contaldi, and M. Peloso, Phys. Rev. D **79** 063517 (2009) [arXiv:0812.1231].

[35] N. E. Groeneboom and H. K. Eriksen, Astrophys. J. **690**, 1807 (2009) [arXiv:0807.2242 [astro-ph]].

[36] N. E. Groeneboom, L. Ackerman, I. K. Wehus and H. K. Eriksen, Astrophys. J **722** 452 (2010) arXiv:0911.0150.

[37] D. Hanson and A. Lewis, Phys. Rev. D **80**, 063004 (2009) [arXiv:0908.0963].

[38] D. Hanson, A. Lewis and A. Challinor, Phys. Rev. D **81** 103003 (2010) [arXiv:1003.0198].

[39] `www.sdss.org`.

[40] J. Maldacena, JHEP **305** 13 (2003) [arXiv:astro-ph/0210603].

[41] E. Komatsu and D. Spergel, Phys. Rev. D **63** 063002 (2001) [arXiv:astro-ph/0005036].

[42] A. Gangui *et al.*, Astrophys. J. **430** 447 (1994) [arXiv:astro-ph/9312033].

[43] E. Komatsu *et al.*, Astrophys. J. Suppl. **192** 18 (2011) [arXiv:1001.4538].

[44] N. Dalal, O. Doré, D. Huterer, and A. Shirokov, Phys. Rev. D **77** 123514 (2008) [arXiv:0710.4560].

[45] A. Slosar, C. Hirata, U. Seljak, S. Ho, and N. Padmanabhan, JCAP **0808** 031 (2008) [arXiv:0805.3580].

[46] C. Boehm, D. Hooper, J. Silk, M. Casse, and J. Paul, Phys. Rev. Lett. **92**, 101301 (2004), astro-ph/0309686.

[47] J. Knodlseder et al., Astron. Astrophys. **411**, L457 (2003), astro-ph/0309442.

[48] P. Jean et al., Astron. Astrophys. **407**, L55 (2003), astro-ph/0309484.

[49] J. F. Navarro, C. S. Frenk, and S. D. M. White, Astrophys. J. **462**, 563 (1996), astro-ph/9508025.

[50] R. C. Hartman et al. (EGRET), Astrophys. J. Suppl. **123**, 79 (1999).

[51] S. D. Hunter, D. L. Bertsch, J. R. Catelli, T. M. Dame, S. W. Digel, B. L. Dingus, J. A. Esposito, C. E. Fichtel, R. C. Hartman, G. Kanbach, et al., Astrophys. J. **481**, 205 (1997).

[52] T. D. Willis (1996), astro-ph/0201515.

[53] D. L. Bertsch, T. M. Dame, C. E. Fichtel, S. D. Hunter, P. Sreekumar, J. G. Stacy, and P. Thaddeus, Astrophys. J. **416**, 587 (1993).

[54] J. M. Fierro, P. F. Michelson, P. L. Nolan, and D. J. Thompson, Astrophys. J. **494**, 734 (1998), astro-ph/9709123.

[55] P. Sreekumar, F. W. Stecker, and S. C. Kappadath, AIP Conf. Proc. **510**, 459 (2004), astro-ph/9709258.

[56] A. V. Kravtsov, A. A. Klypin, J. S. Bullock, and J. R. Primack, Astrophys. J. **502**, 48 (1998), astro-ph/9708176.

[57] L. Bergstrom, P. Ullio, and J. H. Buckley, Astropart. Phys. **9**, 137 (1998), astro-ph/9712318.

[58] C. Boehm and P. Fayet, Nucl. Phys. **B683**, 219 (2004), hep-ph/0305261.

[59] P. Fayet, Phys. Rev. **D70**, 023514 (2004), hep-ph/0403226.

[60] J. F. Beacom, N. F. Bell, and G. Bertone, Phys. Rev. Lett. **94**, 171301 (2005), astro-ph/0409403.

[61] H. Goldberg, Phys. Rev. Lett. **50**, 1419 (1983).

[62] R. L. Kinzer et al., Astrophys. J. **559**, 282 (2001).

[63] S. Rudaz, Phys. Rev. **D39**, 3549 (1989).

[64] J. F. Beacom and H. Yuksel, Phys. Rev. Lett. **97**, 071102 (2006), astro-ph/0512411.

[65] P. Sizun, M. Casse, and S. Schanne, Phys. Rev. **D74**, 063514 (2006), astro-ph/0607374.

[66] C. Boehm, J. Orloff, and P. Salati, Phys. Lett. **B641**, 247 (2006), astro-ph/0607437.

[67] A. Hajian and T. Souradeep, Astrophys. J. **597**, L5 (2003) [arXiv:astro-ph/0308001]. S. Basak, A. Hajian and T. Souradeep, Phys. Rev. D **74**, 021301 (2006) [arXiv:astro-ph/0603406]. A. Hajian and T. Souradeep, arXiv:astro-ph/0501001.

[68] C. Armendariz-Picon, JCAP **0603**, 002 (2006) [arXiv:astro-ph/0509893].

[69] U. Seljak and M. Zaldarriaga, Astrophys. J. **469**, 437 (1996) [arXiv:astro-ph/9603033]; cfa-www.harvard.edu/ mzaldarr/CMBFAST/cmbfast.html

[70] cmbpol.uchicago.edu.

[71] A. Loeb and M. Zaldarriaga, Phys. Rev. Lett. **92**, 211301 (2004) [arXiv:astro-ph/0312134].

[72] M. Kamionkowski, A. Kosowsky and A. Stebbins, Phys. Rev. D **55**, 7368 (1997) [arXiv:astro-ph/9611125]; M. Kamionkowski, A. Kosowsky and A. Stebbins, Phys. Rev. Lett. **78**, 2058 (1997) [arXiv:astro-ph/9609132].

[73] M. Zaldarriaga and U. Seljak, Phys. Rev. D **55**, 1830 (1997) [arXiv:astro-ph/9609170]; U. Seljak and M. Zaldarriaga, Phys. Rev. Lett. **78**, 2054 (1997) [arXiv:astro-ph/9609169].

[74] G. Jungman, M. Kamionkowski, A. Kosowsky and D. N. Spergel, Phys. Rev. D **54**, 1332 (1996) [arXiv:astro-ph/9512139]; G. Jungman, M. Kamionkowski, A. Kosowsky and D. N. Spergel, Phys. Rev. Lett. **76**, 1007 (1996) [arXiv:astro-ph/9507080].

[75] C. G. Boehmer and D. F. Mota, Phys. Lett. **B663**, 168 (2008) [arXiv:0710.2003 [astro-ph]].

[76] L. Campanelli, P. Cea and L. Tedesco, Phys. Rev. Lett. **97** 131302 (2006) [arXiv:astro-ph/0606266].

[77] L. Campanelli, P. Cea and L. Tedesco, Phys. Rev. D **76** 063007 (2007) [arXiv:0706.3802 [astro-ph]].

[78] A. R. Pullen and M. Kamionkowski, Phys. Rev. D **76**, 103529 (2007) [arXiv:0709.1144 [astro-ph]].

[79] N. Padmanabhan *et al.* [SDSS Collaboration], Mon. Not. Roy. Astron. Soc. **378**, 852 (2007) [arXiv:astro-ph/0605302].

[80] D. G. York *et al.* [SDSS Collaboration], Astron. J. **120**, 1579 (2000) [arXiv:astro-ph/0006396].

[81] J. E. Gunn *et al.* [SDSS Collaboration], Astron. J. **131**, 2332 (2006) [arXiv:astro-ph/0602326].

[82] J. E. Gunn *et al.* [SDSS Collaboration], Astron. J. **116**, 3040 (1998) [arXiv:astro-ph/9809085].

[83] J. R. Pier, J. A. Munn, R. B. Hindsley, G. S. Hennessy, S. M. Kent, R. H. Lupton and Z. Ivezic, Astron. J. **125**, 1559 (2003) [arXiv:astro-ph/0211375].

[84] M. Fukugita, T. Ichikawa, J. E. Gunn, M. Doi, K. Shimasaku and D. P. Schneider, Astron. J. **111**, 1748 (1996).

[85] D. W. Hogg, D. P. Finkbeiner, D. J. Schlegel and J. E. Gunn, Astron. J. **122**, 2129 (2001) [arXiv:astro-ph/0106511].

[86] D. L. Tucker *et al.* [SDSS Collaboration], Astron. Nachr. **327**, 821 (2006) [arXiv:astro-ph/0608575].

[87] N. Padmanabhan *et al.*, Astrophys. J. **674**, 1217 (2008) [arXiv:astro-ph/0703454].

[88] M. A. Strauss *et al.* [SDSS Collaboration], Astron. J. **124**, 1810 (2002) [arXiv:astro-ph/0206225].

[89] D. J. Eisenstein *et al.* [SDSS Collaboration], Astron. J. **122**, 2267 (2001) [arXiv:astro-ph/0108153].

[90] G. T. Richards *et al.* [SDSS Collaboration], Astron. J. **123**, 2945 (2002) [arXiv:astro-ph/0202251].

[91] M. R. Blanton, R. H. Lupton, F. Miller Malley, N. Young, I. Zehavi and J. Loveday, Astron. J. **125**, 2276 (2003) [arXiv:astro-ph/0105535].

[92] J. K. Adelman-McCarthy [SDSS Collaboration], Astrophys. J. Suppl. **172**, 634 (2007) [arXiv:0707.3380 [astro-ph]].

[93] N. Padmanabhan *et al.* [SDSS Collaboration], Mon. Not. Roy. Astron. Soc. **359**, 237 (2005) [arXiv:astro-ph/0407594].

[94] S. Ho, C. Hirata, N. Padmanabhan, U. Seljak and N. Bahcall, Phys. Rev. D **78**, 043519 (2008) [arXiv:0801.0642 [astro-ph]].

[95] K. M. Gorski, E. Hivon, A. J. Banday, B. D. Wandelt, F. K. Hansen, M. Reinecke and M. Bartelman, Astrophys. J. **622**, 759 (2005) [arXiv:astro-ph/0409513].

[96] R. E. Smith *et al.* [The Virgo Consortium Collaboration], Mon. Not. Roy. Astron. Soc. **341**, 1311 (2003) [arXiv:astro-ph/0207664].

[97] S. Ando and M. Kamionkowski, Phys. Rev. Lett. **100**, 071301 (2008) [arXiv:0711.0779].

[98] M. Tegmark, Phys. Rev. D **55**, 5895 (1997) [arXiv:astro-ph/9611174].

[99] N. Padmanabhan, U. Seljak and U. L. Pen, New Astron. **8**, 581 (2003) [arXiv:astro-ph/0210478].

[100] C. M. Hirata, N. Padmanabhan, U. Seljak, D. Schlegel and J. Brinkmann, Phys. Rev. D **70**, 103501 (2004) [arXiv:astro-ph/0406004].

[101] J. Carlson, M. White and N. Padmanabhan, Phys. Rev. D **80**, 043531 (2009) [arXiv:0905.0479].

[102] I. K. Wehus, L. Ackerman, H. K. Eriksen and N. E. Groeneboom, Astrophys. J. **707**, 343 (2009) [arXiv:0904.3998].

[103] C. M. Hirata, J. Cosmol. Astropart. Phys. **0909** 011 (2009) [arXiv:0907.0703].

[104] D. A. Varshalovich, A. N. Moskalev and V. K. Khersonsky, Quantum Theory of Angular Momentum Singapore, Singapore: World Scientific (1988) 514p

[105] A. Lewis, A. Challinor and A. Lasenby, Astrophys. J. **538**, 473 (2000) [arXiv:astro-ph/9911177]; `camb.info`

[106] A. A. Starobinskii, JETP **30** 682 (1979).

[107] A. Guth, Phys. Rev. D **23** 347 (1981).

[108] A. Linde, Phys. Lett. B **108** 389 (1982).

[109] A. Albrecht and P. Steinhardt, Phys. Rev. Lett. **48** 1220 (1982).

[110] V. Mukhanov and G. Chibisov, JETP. Lett. **33** 532 (1981).

[111] S. Hawking, Phys. Lett. B **115** 295 (1982).

[112] A. Guth and S. Pi Phys. Rev. Lett. **49** 1110 (1982).

[113] A. Starobinskii, Phys. Lett. B **117** 175 (1982).

[114] J. Bardeen, P. Steinhardt, and M. Turner, Phys. Rev. D **28** 679 (1983).

[115] A. Cooray, D. Sarkar, and P. Serra, Phys. Rev. D **77** 123006 (2008) [arXiv:0803.4194].

[116] D. Tseliakhovich, C. Hirata, and A. Slosar, Phys. Rev. D **82** 043531 (2010) [arXiv:1004.3302].

[117] A. Linde and V. Mukhanov, Phys. Rev. D **56** 535 (1997) [arXiv:astro-ph/9610219].

[118] S. Mollerach, Phys. Rev. D **42** 313 (1990).

[119] D. Lyth and D. Wands, Phys. Lett. B **524** 5 (2002) [arXiv:hep-ph/0110002].

[120] D.Lyth, C. Ungarelli, and D. Wands, Phys. Rev. D **67** 023503 (2003) [arXiv:astro-ph/0208055].

[121] L. Boubekeur and D. Lyth, Phys. Rev. D **73** 021301 (2006) [arXiv:astro-ph/0504046].

[122] Q. Huang, J. Cosmol. Astropart. Phys. **0811** 005 (2008) [arXiv:0808.1793].

[123] J. Xia *et al.*, Astrophys. J Lett. **717** L17 (2010) [arXiv:1003.3451].

[124] F. Bernardis *et al.*, Phys. Rev. D **82** 083511 (2010) [arXiv:1004.5467].

[125] J. K. Adelman-McCarthy [SDSS Collaboration], Astrophys. J. Suppl. **175**, 297 (2008) [arXiv:0707.3413 [astro-ph]].

[126] G. Richards *et al.*, Astrophys. J. Suppl. **180** 67 (2009) [arXiv:0809.3952].

[127] J. Xia *et al.*, JCAP **1008** 13 (2010) [arXiv:1007.1969].

[128] A. Hamilton and M. Tegmark, Mon. Not. Roy. Astron. Soc. **349** 115 (2004) [arXiv:astro-ph/0306324].

[129] M. Swanson, M. Tegmark, and A. Hamilton, arXiv:0711.4352.

[130] D. Schlegel, D. Finkbeiner, and M. Davis, Astrophys. J. **500** 525 (1998) [arXiv:astro-ph/9710327].

[131] A. Cooray and R. K. Sheth, Phys. Rep. **372**, 1 (2002).

[132] W. Press and P. Schechter, Astrophys. J. **187** 425 (1974).

[133] R. K. Sheth and G. Tormen, Mon. Not. Roy. Astron. Soc. **308** 119 (1999), [arXiv:astro-ph/9901122].

[134] G. T. Richards *et al.* [SDSS Collaboration], Mon. Not. Roy. Astron. Soc. **360**, 839 (2005) [arXiv:astro-ph/0504300].

[135] S. Landy and A. Szalay Astrophys. J **412**, 64 (1993).